

---

# **Realistic Rendering and Reconstruction of Astronomical Objects and an Augmented Reality Application for Astronomy**

---

**Andrei Lințu**

**Max-Planck-Institut für Informatik  
Saarbrücken, Germany**

Dissertation zur Erlangung des Grades  
*Doktor der Ingenieurwissenschaften (Dr.-Ing)*  
der Naturwissenschaftlich-Technischen Fakultät I  
der Universität des Saarlandes



MAX-PLANCK-GESELLSCHAFT



max planck institut  
informatik

Eingereicht am 31. Oktober 2007 in Saarbrücken durch

Andrei Lințu  
MPI Informatik  
Stuhlsatzenhausweg 85  
66 123 Saarbrücken

lintu@mpi-sb.mpg.de

**Betreuender Hochschullehrer – Supervisor**

Prof. Dr. Marcus Magnor, Technische Universität Braunschweig, Germany  
Dr.-Ing. Hendrik P. A. Lensch, Max-Planck-Institut für Informatik, Germany

**Gutachter – Reviewers**

Dr.-Ing. Hendrik P. A. Lensch, Max-Planck-Institut für Informatik, Germany  
Prof. Dr. Marcus Magnor, Technische Universität Braunschweig, Germany  
Prof. Dr. Hans-Peter Seidel, Max-Planck-Institut für Informatik, Germany

**Dekan – Dean**

Prof. Dr. Thorsten Herfet, Universität des Saarlandes, Saarbrücken, Germany

**Datum des Kolloquiums – Date of Defense**

7. Dezember 2007 – December 7th, 2007

*to Cami*

## Abstract

These days, there is an ever increasing need for realistic models, renderings and visualization of astronomical objects to be used in planetarium and as a tool in modern astrophysical research. One of the major goals of this dissertation is to develop novel algorithms for recovering and rendering 3D models of a specific set of astronomical objects. We first present a method to render the color and shape of the *solar disc* in different climate conditions as well as for different height to temperature atmospheric profiles. We then present a method to render and reconstruct the 3D distribution of *reflection nebulae*. The rendering model takes into account scattering and absorption to generate physically realistic visualization of reflection nebulae. Further, we propose a reconstruction method for another type of astronomical objects, *planetary nebulae*. We also present a novel augmented reality application called the *augmented astronomical telescope*, tailored for educational astronomy. The real-time application augments the view through a telescope by projecting additional information such as images, text and video related to the currently observed object during observation. All methods previously proposed for rendering and reconstructing astronomical objects can be used to create novel content for the presented augmented reality application.

## Kurzfassung

Realistische Modelle, Visualisierungen und Renderings von astronomischen Objekten gewinnen heutzutage in Planetarium shows oder als Werkzeug für die Astrophysikalische Forschung immer mehr an Bedeutung. Eines der Hauptziele dieser Dissertation ist es, neue Algorithmen zum Rendering und zur Rekonstruktion von Astronomischen Objekten zu entwickeln. Wir beschreiben zuerst ein Verfahren zum Rendering von Farbe und Form der *Sonnenscheibe* für verschiedene Klimate und gegebenen Höhe zu Temperatur Profilen. Im weiteren wird eine Methode zum Rendering und zur Rekonstruktion von 3D Modellen von *Reflexionsnebeln* präsentiert. Das Renderingmodell berücksichtigt Streuung und Absorption, um physikalisch realistische Visualisierungen von Reflexionsnebeln zu erzeugen. Weiter, wird ein Rekonstruktionsalgorithmus für eine andere Art astronomischer Objekte, *Planetarische Nebel*, vorgeschlagen. Wir stellen eine neuartige Erweiterte Realität Anwendung vor, welche für die astronomische Bildung zugeschnitten ist. Die Anwendung erweitert die Sicht durch das Okular des Teleskopes und projiziert zusätzliche Informationen wie Bilder, Text und Video online, während des Betrachtens. Alle vorher erwähnten Verfahren zum Rendering und zur Rekonstruktion von Astronomischen Objekten können verwendet werden, um Inhalte für die vorgestellte Erweiterte Realität Anwendung zu entwerfen.



## Summary

The purpose of this thesis is to present the use of computer graphics for simulating the appearance of several astronomical objects and in particular cases, for recovering their 3D distribution. Further, computer graphics techniques are used to create an augmented reality application geared towards educational astronomy.

We present a method to render the color and shape of the solar disc in different climate conditions and at height to temperature atmospheric profiles that can generate mirages. By using a parabolic approximation for ray-tracing through our atmosphere model we are able to reproduce several mirages appearing during sunset or sunrise such as the green flash, the red flash and other refractive effects of the solar disc. Additionally, by modeling different climate types we can render precise colors of the solar disc at corresponding climate and humidity values.

A method to render and recover the 3D distribution of *reflection nebulae* is also presented in this thesis. These objects are clouds of dust surrounding one or more stars which scatter and absorb the light emitted by the star(s). We develop a rendering model that takes these scattering and absorption effects into account to generate physically realistic images of reflection nebulae. Furthermore, we propose an algorithm to recover the 3D distribution of reflection nebulae based on a single input image, by means of a non linear optimization scheme.

We then focus on another astronomical object, *planetary nebulae*. These objects are formed in the last evolutionary stage of middle size stars and mainly consist of ionized gas and dust. For the reconstruction of these objects we use the axial symmetry inherent to a high number of planetary nebulae to simplify the reconstruction problem starting from a single input image. We jointly recover both ionized gas and dust distributions by consequently optimizing our model and comparing renderings with images at two different wavelengths.

We finish by presenting a novel augmented reality application for educational astronomy. During observation, it augments the view through a telescope's eyepiece by projecting additional information such as images, text and video related to the currently observed astronomical object. All methods previously proposed for rendering and reconstructing astronomical objects can be used to create novel content for this application.

## Acknowledgements

I would first like to thank Prof.Dr.-Ing. Marcus Magnor for giving me the opportunity to pursue my Ph.D. studies at the Graphics–Optics–Vision Independent Research group at the MPI Informatik. In the years at MPI, I broadened my knowledge of computer graphics, but in the meantime also learned a lot more about optics and astronomy in general. I am also very grateful to Prof. Hans-Peter Seidel, who took me warmly in his group after Marcus’s move to Braunschweig. My thanks go also to Dr.-Ing. Hendrik P. A. Lensch for his kind supervision during the last part of my thesis work.

Thanks to Boris Ajdin, Lukas Ahrenberg, Adrian Alexa, Sascha El-Abed, Christian Fuchs, Bastian Goldluecke, Kristian Hildebrand, Ivo Ihrke, Christian Linz, Volker Scholz, Oliver Schall, Timo Stich and Christian Weber for making the work environment here at the MPI such a great working place and being always there for scientific as well as non-scientific discussions.

Special thanks to Robert Bargmann and Gregorz Krawczyk, who both became very close friends to me during my time at MPI. With Gregorz we spent together many happy hours doing things related to our common passion, photography. Robert was always there for a chat or a coffee break; thanks for directing me to those good old classic movies.

During my thesis work, I had occasionally to solve several hardware problems; the assistance of Thomas Hirtz, Axel Köeppel and Michael Leise were always very prompt and mostly welcome. My thanks also go to my friend, Andrei Novak, who helped me with several equipment modifications in the field of electronics.

Financial support for parts of this dissertation has been provided by an International Max Planck Research School for Computer Science scholarship, the Max Planck Center for Visual Computing and Communication, Project BMBF-FKZ01IMC01 and the Max-Planck-Gesellschaft zur Förderung der Wissenschaften e.V.

Thanks also to my parents, Olga and Ilie Lințu, who always encouraged me during my studies and did everything they could to support me. Last, but not least I would like to thank Cami, my wife, for all the support provided during my Ph.D. studies. She was always beside me, for better and for worse.

# Contents

<b>I</b>	<b>Introduction</b>	<b>1</b>
<b>1</b>	<b>Introduction</b>	<b>3</b>
1.1	Main Contributions . . . . .	5
1.2	Chapter Overview . . . . .	6
<b>2</b>	<b>Background</b>	<b>9</b>
2.1	The Electromagnetic Spectrum . . . . .	9
2.2	Light Transport in Participating Media . . . . .	11
2.2.1	Scattering . . . . .	11
2.2.2	Absorption . . . . .	14
2.3	Inverse Problems . . . . .	15
2.4	Powell's Direction Set Optimization Method . . . . .	16
2.5	Planetariums . . . . .	17
2.6	Augmented Reality . . . . .	18
<b>3</b>	<b>Related Work</b>	<b>21</b>
3.1	Rendering of Atmospheric Phenomena . . . . .	21
3.2	Visualization of Astronomical Objects . . . . .	22
3.3	Reconstruction of Astronomical Objects . . . . .	24
3.4	Augmented Reality Applications . . . . .	26
<b>II</b>	<b>Rendering of Astronomical Objects</b>	<b>31</b>
<b>4</b>	<b>Realistic Solar Disc Rendering</b>	<b>35</b>
4.1	Introduction . . . . .	35
4.2	Sunset Science . . . . .	36
4.2.1	Mirages . . . . .	37
4.2.2	The Green Flash . . . . .	37
4.2.3	The Red Flash . . . . .	39
4.2.4	Limb Darkening . . . . .	39

4.3	System Overview . . . . .	40
4.4	Solar Disc Rendering . . . . .	41
4.4.1	Extinction Coefficients . . . . .	41
4.4.2	Atmosphere Model . . . . .	42
4.4.3	Temperature Profiles . . . . .	43
4.4.4	Atmospheric Refraction . . . . .	43
4.4.5	Atmospheric Extinction . . . . .	45
4.4.6	Gamma Correction . . . . .	46
4.5	Results . . . . .	46
4.6	Conclusion . . . . .	48
<b>5</b>	<b>Reflection Nebula Visualization</b>	<b>51</b>
5.1	Introduction . . . . .	51
5.2	Reflection Nebula Physics . . . . .	52
5.2.1	Interstellar Dust . . . . .	53
5.3	Color . . . . .	54
5.4	Lighting Model . . . . .	54
5.5	Voxel Characteristics . . . . .	56
5.6	Nebula Generation . . . . .	57
5.7	Interactive Rendering . . . . .	58
5.8	Results . . . . .	60
5.9	Conclusions . . . . .	60
<b>III</b>	<b>Reconstruction of Astronomical Objects</b>	<b>63</b>
<b>6</b>	<b>Reflection Nebula Reconstruction</b>	<b>67</b>
6.1	Introduction . . . . .	67
6.2	3D Reconstruction . . . . .	68
6.2.1	Rendering and Runtime Optimization . . . . .	70
6.3	Results . . . . .	71
6.4	Conclusion . . . . .	74
<b>7</b>	<b>3D Reconstruction of Gas and Dust in Planetary Nebulae</b>	<b>77</b>
7.1	Introduction . . . . .	78
7.2	Planetary Nebulae . . . . .	80
7.2.1	Absorption and Scattering . . . . .	80
7.3	3D Reconstruction . . . . .	82
7.3.1	Optimization . . . . .	83
7.3.2	Planetary Nebula Reconstruction . . . . .	84
7.4	Rendering and Visualization . . . . .	87

7.5	Results . . . . .	88
7.5.1	Planetary Nebula M3-35 . . . . .	90
7.5.2	Planetary Nebula Hen 2-320 . . . . .	91
7.6	Discussion and Future Work . . . . .	92

## **IV An Augmented Reality Application for Educational Astronomy 95**

<b>8</b>	<b>Augmented Astronomical Telescope</b>	<b>97</b>
8.1	Introduction . . . . .	97
8.2	System Description . . . . .	99
8.3	Telescope Optical Characteristics . . . . .	100
8.4	Telescope Pointing and Sidereal Tracking Accuracy . . . . .	102
8.5	Projection System . . . . .	104
8.6	Adaptation of the Human Visual System . . . . .	108
8.7	Customized Planetarium Software . . . . .	110
8.7.1	Field of view calibration . . . . .	112
8.7.2	Additional Information . . . . .	112
8.8	Input Device . . . . .	114
8.9	Fields of Application . . . . .	116
8.10	Conclusion and Future Work . . . . .	116
<b>9</b>	<b>Discussion and Conclusion</b>	<b>119</b>
9.1	Summary . . . . .	119
9.2	Future Work . . . . .	120
<b>A</b>	<b>Monte-Carlo Simulation of Anisotropic Photon Scattering</b>	<b>123</b>
<b>B</b>	<b>Celestial Coordinate Systems</b>	<b>125</b>
	<b>Curriculum Vitae</b>	<b>149</b>



# **Part I**

## **Introduction**





---

# Chapter 1

## Introduction

Astronomical research can be very well seen correlated to the instruments available to astronomers over the centuries. The early instruments were all naked-eye instruments, like the gnomon, astrolabe or astronomical quadrant, mainly used to measure the elevation of certain astronomical objects on the sky or to determine the current time or date [[Zinner 1957](#)]. It was only after Galileo's discovery and use of the telescope to observe the night sky that the heliocentric theory of Copernicus (Figure 1.1) was confirmed and validated by observations. Another major breakthrough in our understanding of the structure of the universe came with Hubble's discovery that the Andromeda Galaxy is not part of our Milky Way but another galaxy far away. This discovery was made possible by the use of the 100-inch Hooker telescope and of photographic plates, by the means of which it could be demonstrated that the newly discovered galaxy is made out of distinct stars.

It is not until the 70-80s that CCD sensors got to be used by daily basis in astronomy. They however, enabled far deeper observations of the sky due to their highly increased quantum efficiency over photographic plates. Consequently, this allowed more precise measurements and between others lead also to the discovery of extra-solar planets. With the arrival of CCD sensors, image processing became one of the main tools for the analysis of the gathered astronomical data, and special techniques such as the Richardson-Lucy deconvolution [[Richardson 1972](#), [Lucy 1974](#)] have been developed for special use in astronomical data reduction.

Parallel to the importance of image processing in astrophysical research, computer graphics is also gaining importance. As a concrete example, Monte Carlo simula-

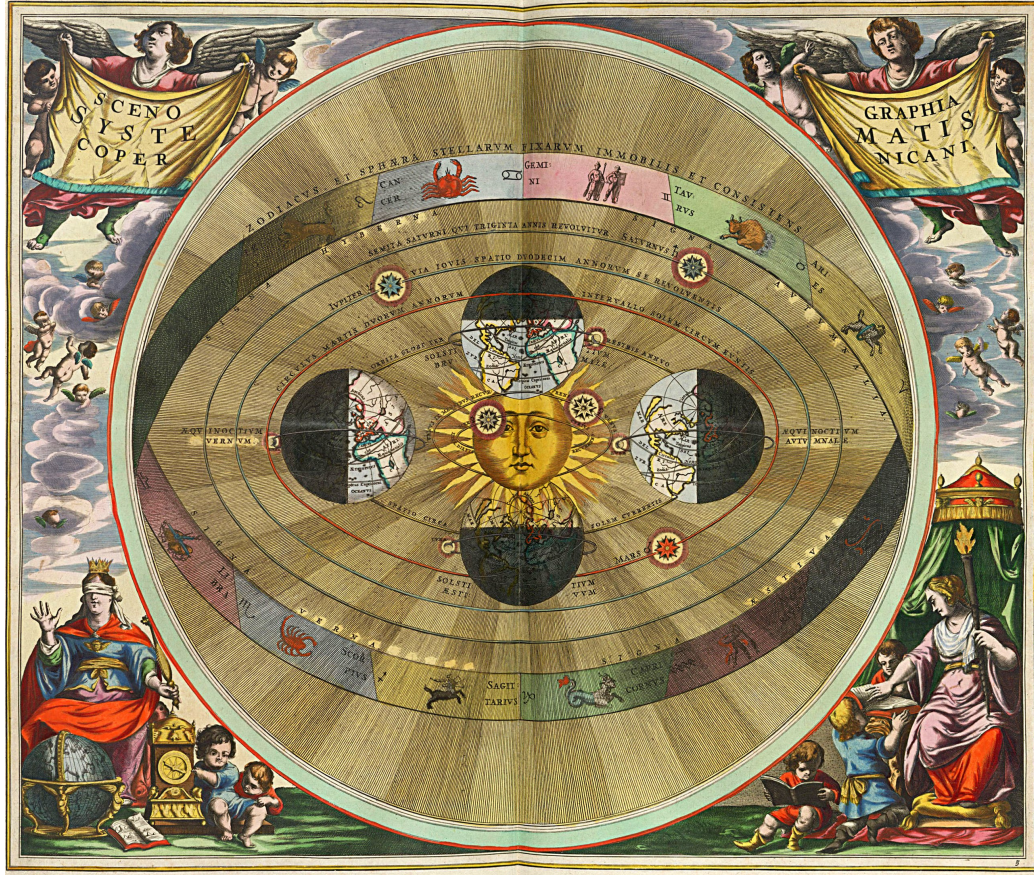


Figure 1.1: Scenography of the Copernican world system, from the *Harmonia Macrocosmica* of Andreas Cellarius [Cellarius 1661]. Image courtesy of Robert van Gent [van Gent, Robert 2007]

tion methods are used in astrophysical research to compute full photo-ionization simulations and predict the 3D distribution of planetary nebulae [Ercolano et al. 2003]. These models can be afterwards used to simulate and study the morphology and to compute distances to planetary nebulae [Monteiro et al. 2005] (which are known with a rather poor precision).

Computer graphics and visualization have an increasing role also in educational astronomy, as planetariums with digital projectors become more frequent these days. There is almost no planetarium show nowadays without a spectacular flyby of 3D astronomical objects. This means that there is also a need for 3D models of different kind of astronomical objects. Some of the methods described in this thesis can be used to generate and render models which can be later used in planetarium shows.

Until the appearance of motorized and computerized telescopes (so called GOTO telescopes) every amateur astronomer had to know the starry sky very well and her/his only choice to find astronomical objects was a precise alignment of the instrument and the use of detailed sky maps. Once GOTO telescopes got popular and affordable, more and more amateur astronomers selected these type of telescopes as their instrument of choice. Once the telescope is aligned and calibrated, the user just has to input the identifier of the desired object in a hand controller and the telescope slews to it, in a matter of seconds.

While GOTO telescopes solved the time consuming problem of finding a particular astronomical object on the sky, the problem of observing and perceiving faint astronomical objects is still an open issue. The system presented in this thesis in Chapter 8, we call the *augmented astronomical telescope* tries to solve this problem by overlaying directly into the eyepiece view, online, high resolution images of the observed object, to improve the perception and give visual hints to the stargazer. For a German language popular science article about the *augmented astronomical telescope* the reader can refer to the article in the German version of the Sky and Telescope magazine, *Astronomie Heute* [Hügler 2006]. There is also a report on the New Scientist Space column about our system [Groshong 2006].

## 1.1 Main Contributions

The fundamental ideas discussed in this dissertation have already been partially published in the following conference, symposium and workshop proceedings [Lințu et al. 2005, Magnor et al. 2005, Lințu and Magnor 2005, Lințu and Magnor 2006, Lințu et al. 2007b, Lințu et al. 2007a, Lințu et al. 2007c]. With respect to these publications, we revise presented methods and demonstrate improved results. The key contributions can be summarized as follows:

- A non-linear ray-tracing algorithm developed to simulate different colors and shapes of the *solar disc* depending on atmospheric dust and ice particle composition as well as temperature to height profiles.
- An algorithm designed for realistic rendering of *reflection nebulae*. The renderings can be used by astrophysicists as a research tool, as well as by planetarium show artists to generate realistic 3D flybys of these astronomical objects.
- A method to reconstruct the 3D distribution of reflection nebulae based on a single input image. Although an ill posed problem, we obtain plausible reconstructions by carefully driving the optimization process.

- An algorithm to reconstruct the ionized gas as well as the dust particle distribution in *planetary nebulae* using two images at different wavelengths. By assuming axial symmetry in the objects to reconstruct, we simplify the reconstruction problem and solve it by a non-linear optimization approach.
- A combined software and hardware system designed to augment the view through computer controlled astronomical telescopes. The system overlays directly in the eyepiece view high resolution images, additional information and movie clips related to the currently observed object thus improving the perception of faint astronomical objects.

Figure 1.2 presents some of the results and highlights of the methods and systems proposed in this thesis.



Figure 1.2: Top, left. A sunset scenario in a maritime climate, generated with the method described in Chapter 4. Top, right. The Augmented Astronomical Telescope, described in Chapter 8. Bottom. Renderings of a synthetic reflection nebula datasets using the algorithm presented in Chapter 5

## 1.2 Chapter Overview

This dissertation is structured as follows. In the remainder of Part I we provide background information on general concepts or possible places of application for



the algorithms and techniques proposed in this thesis, Chapter 2. Chapter 3 summarizes related work in the fields of astronomical visualization, reconstruction as well as augmented reality applications related to the one presented in this thesis. In Part II we describe proposed methods for rendering the solar disc and reflection nebulae. Chapter 4 presents our method for realistic solar disc rendering, taking into consideration different climate types as well as reproducing atmospheric mirages. Chapter 5 presents our rendering and visualization approach for reflection nebulae, considering scattering and absorption, at interactive frame-rates. Part III focuses on the 3D reconstruction of two types of astronomical objects: reflection and planetary nebulae. Chapter 6 describes a reconstruction algorithm which recovers plausible 3D models of reflection nebulae from a single input image. We present our method for the joint recovery of gas and dust distribution in planetary nebulae in Chapter 7. Part IV consist only of Chapter 8, where the augmented reality system for educational astronomy proposed by us is presented. The thesis is summarized and we give outlines for future work in the relevant area in Chapter 9. Additionally, in Appendix A we describe the Monte-Carlo method used to precompute the scattering probability for the rendering described in Chapter 5. Appendix B describes the conversion from altitude–azimuth to equatorial coordinates used in the planetarium software for the augmented reality system described in Chapter 8.



---

---

## Chapter 2

# Background

This chapter presents some background information on concepts which are found throughout this thesis, or areas where the techniques proposed have direct applications. It describes in some detail mostly physical phenomena which are referred to in the chapters dealing with physically correct renderings or 3D reconstructions of astronomical objects. Because all the methods proposed in Parts II and III of this thesis involve working with a multi-spectral representation of the electromagnetic spectrum, we summarize related elements in Section 2.1. Scattering and absorption are also considered in Parts II and III of this dissertation, in Section 2.2 we describe the physical background behind these phenomena. Section 2.3 shortly presents inverse problems and their use in computer graphics; both reconstruction methods presented in Part III are ill-posed inverse problems. The reconstruction algorithms presented in Part III use Powell's direction set optimization method, which is presented in Section 2.4 of this chapter. All rendering and reconstruction methods presented in Parts II and III can be employed to create novel content for educational purposes to be used in planetariums, which are presented in Chapter 2.5. We list in Chapter 2.6 general concepts and types of display devices in augmented reality, related to the application presented in Part IV designed as an educational tool for observational astronomy.

### 2.1 The Electromagnetic Spectrum

All methods presented in this thesis related to rendering or reconstruction of astronomical objects have a close link to the electromagnetic spectrum, this is why

we chose to describe it very shortly here. Figure 2.1 presents a schematic representation of the electromagnetic spectrum. Electromagnetic radiation is characterized by a given wavelength  $\lambda$ , measured in nanometers ( $nm$ ) which is directly correlated with a frequency  $\nu$  in Hertz ( $Hz$ ) and also corresponds to an emissive object of a given temperature, as described in Planck's law of blackbody radiation [Planck 1901]. The relationship between  $\lambda$  and  $\nu$  is given by

$$\nu = \frac{c}{\lambda} \quad (2.1)$$

Where  $c$  denotes the speed of light in vacuum. Note that this formula holds only for the propagation of light through vacuum. Inside a medium like air, the speed of the propagation is slower than  $c$  and the actual wavelength is correspondingly shorter [Petty 2004]. Light perceived by the human visual system represents only a small fraction of this spectrum. Relative to wavelength, the upper limit of what the human visual system can perceive is the infrared emission ( $700\text{ nm}$ ) and the lower limit is the ultraviolet emission ( $400\text{ nm}$ ).

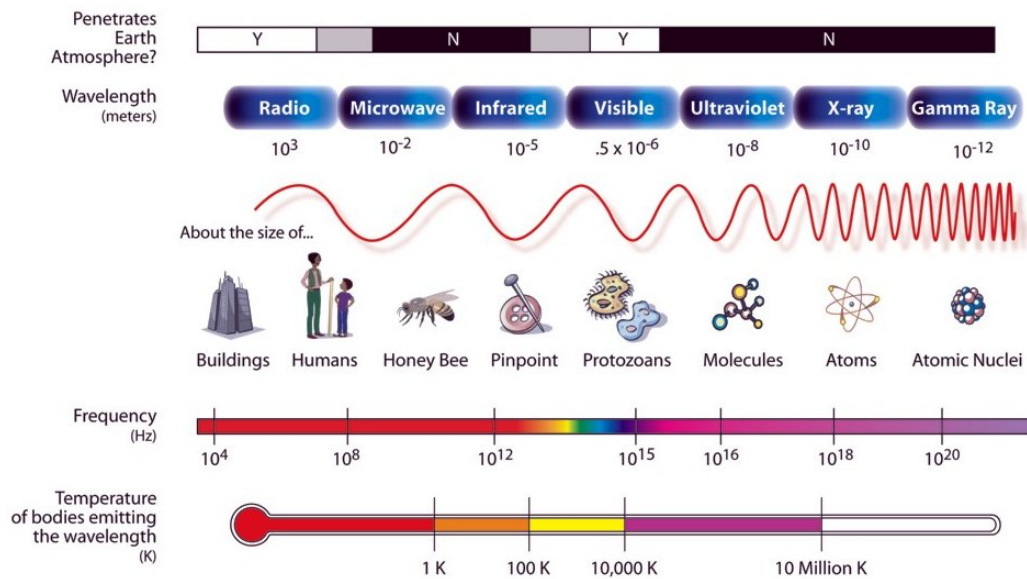


Figure 2.1: A schematic overview of the whole electromagnetic spectrum. The size of the wavelength for each type of radiation is compared to well known objects. Wavelength is generally measured in nanometers ( $nm$ ) which corresponds to an unique frequency, in Hertz ( $Hz$ ). The visible spectrum stretches from  $400\text{ nm}$  to  $700\text{ nm}$ . Note the bar on the bottom part which shows the temperature of each emitting body based on Planck's law of blackbody radiation. Image courtesy of NASA [NASA c]



In computer graphics, most conventional color rendering is done using only the three basic color channels, Red, Green and Blue. When more complicated physical phenomena such as scattering (see Section 2.2.1) are simulated, the three base colors are a too sparse sampling of the visible electromagnetic spectrum, and light at more wavelengths, i.e., a multi-spectral approach has to be considered. This is the case in Chapters 4 and 5 of this thesis. In Chapter 7 we recover jointly dust and gas distributions of planetary nebulae by using data from the infrared or radio wavelengths of the electromagnetic spectrum combined with visible wavelength images.

## 2.2 Light Transport in Participating Media

Most chapters in this thesis deal with light transport through participating media, so we now give a short physical background on the interaction of light with particles present in the medium it traverses. The path of light rays through vacuum can be considered to be a straight line. However, in almost every case light rays traveling in the atmosphere are influenced by the particles contained in the atmosphere or even by the air molecules. If the size of these particles is similar to the wavelength of visible light, these interactions are mostly noticeable.

The two major types of interaction of light with small particles are *scattering* and *absorption*. By scattering, we refer to the phenomenon of a photon being "reflected" in another direction when reaching a small particle. Absorption refers to the transformation of part of the photons energy into heating up the particle it interacts with. Let  $\sigma_{\text{sct}}$  be the scattering coefficient and  $\sigma_{\text{abs}}$  be the absorption coefficient; then by  $\sigma_{\text{ext}} = \sigma_{\text{abs}} + \sigma_{\text{sct}}$  we denote the *extinction* coefficient which accounts for the total loss of energy when light passes through the participating medium due to both scattering and absorption. To be able to quantify the relative strength of scattering and absorption, the albedo  $\alpha$  of a particle is defined as  $\alpha = \sigma_{\text{sct}} / \sigma_{\text{ext}}$ . If all incident radiation is absorbed, i.e. there is no scattering present this corresponds to a completely black particle with  $\alpha = 0$ . If, on the other hand, all radiation is scattered without any absorption the albedo of the particle is  $\alpha = 1$ .

### 2.2.1 Scattering

When incoming light encounters a particle, it is scattered in given directions and with given intensity depending mainly on the size of the particle and the wavelength of the incoming light. For exact computations of the amount of light scat-

tered in every direction, complicated and time consuming radiation transfer computations have to be effectuated [Petty 2004]. The amount of light scattered in every direction can be modeled by a phase function, which can be regarded as a probability density function of a photon being scattered in a given direction.

### Scattering Phase Function

Because scattering phase functions of many particles are often complicated and as already mentioned before require time consuming computations, for many applications analytical phase functions which resemble closely the real phase function are used. One of the most widely used phase functions is the Henyey-Greenstein phase function [Henyey and Greenstein 1941]. It is given by

$$p(\theta) = \frac{1 - g^2}{2 \cdot (1 + g^2 - 2 \cdot g \cdot \cos\theta)^{3/2}}, \quad (2.2)$$

where  $g$  is an anisotropy factor for forward and backward scattering. For  $g = 0$ , we have an isotropic scattering, i.e., light is scattered in every direction with the same intensity. As the value of  $g$  increases, the particle modeled by the phase function will show a stronger forward scattering. Using this phase function and Monte Carlo simulation, the amount of light scattered in every direction for different dust densities can be precomputed and tabulated as described in Appendix A.

Although the Henyey-Greenstein phase function approximates relatively well real scattering phase functions, there have been other phase functions proposed. The double Henyey-Greenstein phase function [Petty 2004] is designed to better replicate cases with  $g < 0$ , i.e., backward scattering. Because exact models of scattering are important in modern medicine, a recent work by Binzoni et al. [Binzoni et al. 2006] proposes a new approach for more precise computations of Henyey-Greenstein based phase functions.

### Rayleigh Scattering

One of the particular cases of scattering occurs when the size of the particle is much smaller than the wavelength of light, and can be described using the laws proposed by Lord Rayleigh [Minnaert 1954]. Scattering can be considered to be twice as strong backwards and forwards compared to the direction perpendicular to the incoming light, Figure 2.3. In this case, light is scattered much more at the violet (400 nm) end of the visible electromagnetic spectrum, proportional with  $1/\lambda^4$ , where  $\lambda$  is the wavelength, Figure 2.2. Rayleigh scattering is the main

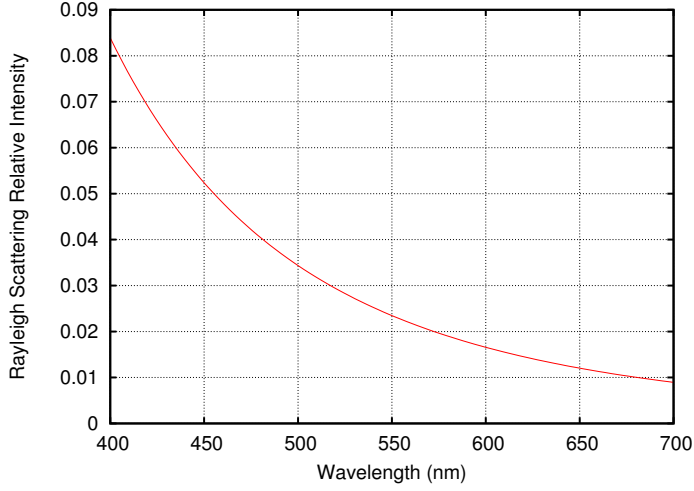


Figure 2.2: A plot highlighting the proportion of light scattered at different wavelengths given Rayleigh scattering. Note that considerably more light is scattered at the blue end of the spectrum (400 nm), than at the infrared end (700 nm)

cause for the blue color of the sky; direct sunlight reaching the atmosphere is scattered by the small molecules of air stronger at the blue wavelengths and much less for the green, yellow and red part of the visible electromagnetic spectrum. The exact amount of light of wavelength  $\lambda$  scattered into a given direction is:

$$I(\lambda) = I_0(\lambda) \cdot \frac{8\pi^4 N \alpha^2}{\lambda^4 R^2} (1 + \cos^2 \theta) \quad (2.3)$$

where  $N$  is the number of scatterer particles,  $\alpha$  is the polarizability,  $R$  is the distance from the scatterer and  $\theta$  being the angle between the ray from the observer to the scatterer and the ray from the scatterer to the light source.

## Mie Scattering

If the size of the particles is comparable with the wavelength of the interacting light, and the particles can be fairly approximated as having spherical shape, scattering is described by the laws of Mie theory [van de Hulst 1982]. In this case, scattering cannot be considered as isotropic; depending on particle size it can highlight various degrees of forward scattering, Figure 2.4. On the other side, opposite to Rayleigh scattering, Mie scattering is much less wavelength dependent.

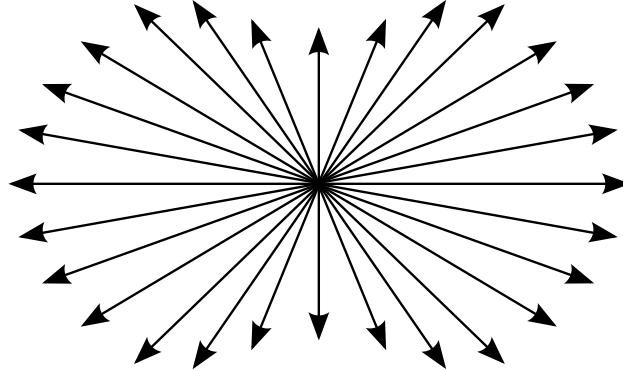


Figure 2.3: Typical Rayleigh scattering pattern, for particles with the size up to  $1/10$  of the wavelength of light. Light is scattered slightly stronger forward and backwards. Because of the strong wavelength dependence of Rayleigh scattering, light at the blue end of the electromagnetic spectrum is scattered much stronger than light at the red end of the spectrum

This is also why clouds, mist and fog appear white; because of the larger size of water droplets light is scattered equally for every wavelength. A good explanation of why the sky is blue, Rayleigh and Mie scattering can be found on the following website [[HyperPhysics 2007](#)].

### 2.2.2 Absorption

When light interacts with participating media, it is not always completely scattered. Depending on the material the particle is consisting of, different proportions of the incident light are transformed into heat and the incident light is attenuated.

If the initial light has the intensity  $I_0(\lambda)$  before absorption, the value after absorption can be computed by:

$$I(\lambda) = I_0(\lambda) \cdot e^{-\int_{\gamma} \sigma_a ds} \quad (2.4)$$

where  $\gamma$  is the path on which the light travels and  $\sigma_a$  is the absorption coefficient of the particles. Absorption is easily noticeable at sunrise or sunset, as the solar disc has a much lower intensity compared to when it is at higher altitudes in the sky. This is due to the light travelling a much longer way through the atmosphere and the strong absorption.

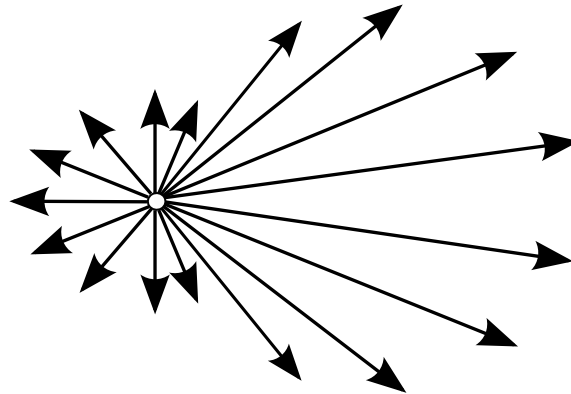


Figure 2.4: Typical Mie scattering pattern, for particles with the size larger than  $1/10$  of the wavelength of light. Light is scattered slightly much stronger forwards than in any other direction, increasing with particle size. This scattering is weakly wavelength dependent, typically Mie scattered light maintaining its color

## 2.3 Inverse Problems

Inverse problems are generally *ill-posed*, as opposed to *well posed* problems which satisfy the three conditions first proposed by Hadamard [[Hadamard 1902](#)]: a solution exists, the solution is unique, and it depends continuously on the data. An ill-posed problem is usually not satisfying one, if not more of the conditions for a well posed problem. To avoid the non-continuity of the dependence of the model on small changes in the measurements, usually additional constraints are imposed upon the model, generally known as *regularization*. For a statistically based description of ill-posed problems the reader should refer to [[Tarantola 2005](#)].

Inverse problems can be divided into two categories: linear and non-linear. Linear inverse problems are generally easier to solve than non-linear ones because they generally allow the building of a linear correspondence between the measured data and the current model. If there is no linear correspondence between the model and the measured data, the inverse problem is said to be non-linear. The reconstruction algorithms developed to recover 3D distributions presented in Part III of this thesis, all use non-linear optimization algorithms such as Powell's Optimization algorithm [[Press et al. 1992](#)].

In computer graphics, inverse problems appear generally in cases when the geometry of an object, its reflecting properties or its entire 3D structure are to be reconstructed. Recovering geometry and scene properties by means of computer graphics from photographs of a scene has been introduced as *inverse rendering* by

Marschner [Marschner 1998]. Image-based acquisition techniques which recover additionally also the material reflecting properties are presented by Lensch [Lensch 2003]. To recover an entire 3D volume, most common techniques are based on *computerized tomography* (CT) [Kak and Slaney 1988]. For an exact reconstruction using CT techniques a large number of projections of the object of interest are usually necessary. We present in Chapters 6 and 7 two methods for recovering the 3D distribution in reflection and planetary nebulae based on a single projection.

## 2.4 Powell's Direction Set Optimization Method

Powell's direction set optimization method [Powell 1964] is an iterative numerical method to find the minimum of a function. It follows the general scheme of successive line minimizations without computing analytically the function's gradient, which can prove to be difficult or impossible in many cases. The method generates a set of  $N$  *conjugate directions* until the minimum is reached, Figure 2.5.

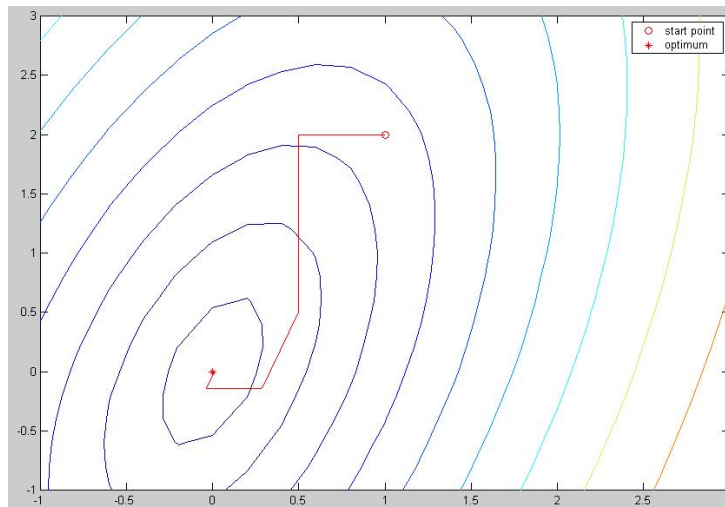


Figure 2.5: An illustration of the optimization steps until the minimum is reached using Powell's direction set method. It evaluates the function's local slope along all dimensions and determines the conjugate gradient direction. Image courtesy of Giovanni Tonel [Tonel 2007]

For a given function  $f(x)$ , if we start at a point  $x_0$  in an  $M$ -dimensional space, the method proceeds from this starting point along a vector  $u$  to find the minimum.

However, after the minimization in the direction of  $u$ , we want to minimize in another direction  $v$ , but without 'spoiling' the already achieved minimization in the direction  $u$ . A set of two vectors  $u$  and  $v$  with the property that the change in the gradient of the function  $f$  stays perpendicular to  $u$  is called *conjugate*. A set of vectors for which this is valid for all pairs is called a *conjugate set*. The algorithm then performs  $n$  line minimizations on the vectors from the conjugate set until the global minimum of the function is reached. We use the implementation given in [Press et al. 1992] for all the reconstruction methods presented in Part III of this thesis.

## 2.5 Planetariums

Nowadays digitally equipped planetariums are becoming more and more frequent, so there is also an increasing demand in astronomical digital content that can be used for planetarium shows. Leading planetarium manufacturers provide fully integrated digital projection solutions which can replace or augment a traditional optomechanical planetarium projector. Some examples are the *powerdome*® [Carl Zeiss Jena GmbH 2007] from Carl Zeiss (Figure 2.6) or the *Digistar 3* [Evans & Sutherland 2007] from Evans & Sutherland.

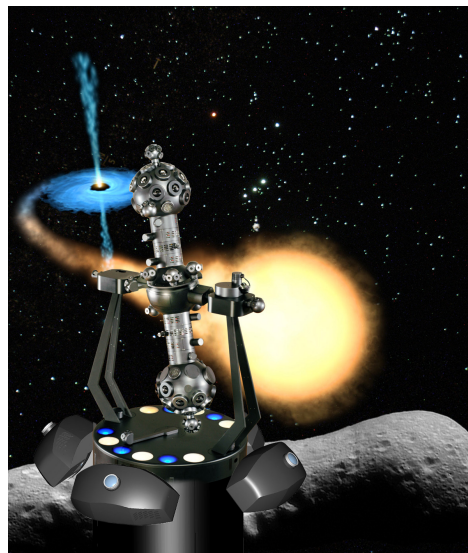


Figure 2.6: A classical optomechanical projector from Carl Zeiss and their digital projectors permit the combination of both projection technologies. Image courtesy of Carl Zeiss [Carl Zeiss Jena GmbH 2007]

In order to use their digital projection capabilities, all modern planetariums display highly realistic space shows, consisting mainly of astronomical object flybys. The great majority of media for these shows are created by talented space artists and are just partially based on physical certainties. Several techniques presented in this thesis (Chapters 4, 5, 6 and 7) can be used to create and render physically plausible and realistic 3D models of reflection and planetary nebulae as well as renderings of the solar disc given different climatic and temperature gradients in the atmosphere.

## 2.6 Augmented Reality

Augmented reality is a relatively new domain and is emerging as an alternative solution to virtual reality. In a given *virtual reality* application, the user is emerged in a completely synthetic environment. In contrast to this, *augmented reality* does not completely suppress the real environment, the real world is augmented by relevant additional information to the user by means of a computer [Bimber and Raskar 2005]. Indeed, augmented reality is situated between virtual reality and the real world and uses the advantages of both. The perception of the real world is augmented with information which the human senses could not perceive. For a comprehensive review of the field, the reader should refer to the field overview paper by Azuma [Azuma 1997], or to the recent book by Bimber and Raskar [Bimber and Raskar 2005].

There are several ways of building an augmented reality system. The widest spread systems use head mounted displays, though recently hand held and spatial displays are also emerging [Bimber and Raskar 2005]. Generally, almost all types of displays used in augmented reality can be classified into *video see through displays* and *optical see through displays*. A video see through system is one where the user only sees the environment displayed onto a screen as recorded by an attached video camera. It has the disadvantage that the user is less likely to perceive the scene as realistic (a similar experience is using digital cameras with electronic viewfinder), but the advantage is that overlaying additional information and system calibration is much easier. In contrast to video see through systems, optical see through systems overlay all additional information directly onto the image of the real world perceived by the user. This is achieved by means of semi-transparent displays or beam splitters. Optical see through systems have the advantage of a higher realism, but are more complicated to align and calibrate. The augmented reality system proposed by us as an educational aid in astronomy uses an optical see through system and is presented in Chapter 8. Augmented





Figure 2.7: A typical augmented reality application for architectural planning. Image courtesy of the VR Center for the Built Environment [[VR Centre for the Built Environment 2004](#)]

reality systems have a very large domain of applicability nowadays. We mention just some of the fields where this technology is applied: industrial, medicine, architecture and construction, entertainment, military and education applications.



---

## Chapter 3

# Related Work

In this chapter we review related work to the solutions presented in this thesis. There is a great amount of work in the field of rendering and reconstruction of astronomical objects in the computer graphics as well as in the astrophysical literature. We also present here augmented reality applications and educational astronomy devices related to the augmented astronomical telescope proposed by us.

### 3.1 Rendering of Atmospheric Phenomena

Realistic renderings of atmospheric phenomena has been a well researched topic in the computer graphics community. We review papers focusing on solar disc rendering, as well as work on rendering the sky.

Some publications focus on physically correct and realistic atmosphere simulations, for daytime [[Preetham et al. 1999](#)], [[Nishita et al. 1996](#)] as well as for nighttime [[Wann Jensen et al. 2001](#)]. Also, a system for rendering the atmosphere from a viewpoint situated in space is presented by Nishita et al. [[Nishita et al. 1993](#)]. These approaches concentrate on fast rendering of the atmosphere, approximating the physics of atmospheric light transport. An evaluation and validation with real world measurements of the Preetham sky model [[Preetham et al. 1999](#)] was recently presented by Zotti et al. [[Zotti et al. 2007](#)].

A work focusing on a physically correct simulation of the atmosphere during twilight phenomena is presented in [[Haber et al. 2005](#)]. The authors create a model of the Earth's atmosphere including air molecules, aerosols and water particles

and account for Rayleigh as well as for Mie scattering by simulating full radiation transfer over a discretized hemisphere. By considering different climatic conditions, corresponding hemispherical twilight skies can be computed.

A different method focusing on the rendering of the solar disc is presented by Bruton [Bruton 1996]. In his thesis, ray-tracing through the atmosphere is performed using Lehn's model [Lehn 1985], and solar disc appearance is simulated from diverse input temperature profiles. However, this work considers only Rayleigh scattering due to air molecules. Thus, different types of sunsets depending on current aerosol distribution in the atmosphere cannot be simulated. Another work based on Bruton's model concentrates more only on reproducing the correct shape of the solar disc is presented by Sloup [Sloup 2003].

One possible approach is to simulate the green flash or other atmospheric phenomena using an approach based on photon mapping [Gutierrez et al. 2004, Seron et al. 2004, Guitierrez et al. 2005]. These papers focus on implementing a "Curved Photon Mapping" algorithm. Although the obtained results are highly realistic, these approaches are slow (due to the photon mapping algorithm), and they lack any dependence on climate conditions.

A paper describing the theoretic concepts of non-linear ray-tracing was presented by Gröller [Gröller 1995]. He describes data structures and ray object intersection algorithms specially suited to the case of non-linear rays. An in depth review of work related to rendering of atmospheric phenomena is presented by Sloup [Sloup 2002]. As already mentioned in the previous Chapter, for a book describing phenomena relating to atmospheric optics the reader should refer to [Minnaert 1954].

In contrast to the already reviewed works, our approach presented in Section 4 concentrates on combining the simplified parabolic model for ray-tracing in the atmosphere presented by Lehn [Lehn 1985] and the climate dependent stratified atmosphere model presented in [Haber et al. 2005] in order to create a ray-tracing system which realistically reproduces several possible sequences of the solar disc at sunset or sunrise.

## 3.2 Visualization of Astronomical Objects

Recently, there have been large efforts to produce 3D simulations of astronomical nebulae, particularly the Orion nebula [Nadeau et al. 2001], where a highly detailed model of the nebula was created, based on data from astrophysical research papers. Time consuming renderings on supercomputers were generated for the final fly-through animation.

Hanson and coauthors published recently papers concentrating on ways to solve the problems which arise while trying to render or visualize very large scale environments such as our Universe [Fu and Hanson 2007, Hanson et al. 2000]. They use power scale coordinates, to be able to adapt the conventional graphics pipeline such as interactive visualizations of the Universe with huge scale differences are possible.

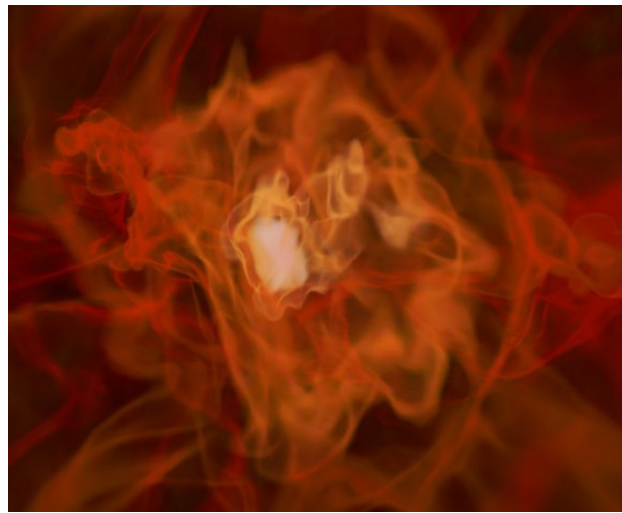


Figure 3.1: A frame of the animation generated by Kähler et al. [Kähler et al. 2002] using adaptive mesh refinement enabling the authors to reproduce very fine detail. Image courtesy of Ralf Kähler [Kähler et al. 2002]

A work presenting visualizations of the first star in the universe is presented in [Kähler et al. 2002] (Figure 3.1). The authors use Adaptive Mesh Refinement to be able to create volume renderings of the available data which is on large spatial as well as temporal scales. Kähler et al. describe in [Kähler et al. 2006] a framework for rendering volumetric cosmological datasets. The method uses graphics hardware to implement an adaptive ray-casting approach to obtain high quality, artefact free interactive renderings. Isotropic scattering is also taken account of for the three wavelengths corresponding to the used astronomical filters. A more recent work [Kähler et al. 2007] of the same authors focuses on optimizations needed for a joint rendering of point set data as well as volumetric grid data.

Recent work of Zotti et al. [Zotti and Gröller 2005, Zotti et al. 2006] is concentrated on astro-archaeological applications of astronomical visualizations. They computed the positions of several brighter astronomical objects and stars in order to help archaeologists easier determine the reason behind the orientation of several ancient temples.

In astrophysical research, the importance of 3D models of astronomical objects has increased lately. Ercolano et al. introduced the mocassin 3D Monte-Carlo photo-ionization code [Ercolano et al. 2003, Ercolano et al. 2005] which is widely used in the literature for comparing models of planetary nebulae with observations. The results are very exact simulations using a given set of parameters, but have the major disadvantage that computations times are long and the parameters have to be adjusted by hand after every simulation run, until the results best match the observations [Monteiro et al. 2005]. A method to speed up 3D photo-ionization by interpolation was proposed by Morisset [Morisset 2006]. Due to the faster computation time this method would be more appropriate for automatic parameter optimization. Another approach towards 3D modelling of planetary nebulae is presented by Steffen et al. [Steffen and López 2006]. The authors combine models generated by commercially available 3D modelling software with a custom renderer to reproduce observed data for given planetary nebulae.

### 3.3 Reconstruction of Astronomical Objects

The problem of reconstructing the 3D distribution of an object from its projections is solved in computed tomography usually by having available a high number of projections of the object of interest from different viewpoints [Kak and Slaney 1988]. Because of our limited viewpoint on Earth, for most astronomical objects outside our Solar System we can observe only a single viewpoint, thus making reconstruction of astronomical objects a difficult task.

There are several papers in the computer graphics literature which tackle the problem of reconstructing astronomical objects. Hildebrand et al. [Hildebrand et al. 2006] propose a framework for 3D reconstruction of spiral galaxies. By the means of an analysis-by-synthesis approach the authors recover the distribution of dust and gas based on visible and infrared input images.

A method for reconstructing the 3D structure of another type of astronomical objects, planetary nebulae, from a single image has been proposed in [Magnor et al. 2004] (Figure 3.2). The appearance of planetary nebulae is mostly influenced by the self-emission of ionized gas, slightly simplifying the reconstruction problem. Furthermore, the authors apply axial symmetry as a constraint to reduce the complexity of the reconstruction process from 3D to reconstructing a 2D density map, which is rotated around the axis of symmetry to obtain a volumetric dataset. The authors then optimize for this so called map via an inverse rendering approach using non linear optimization.

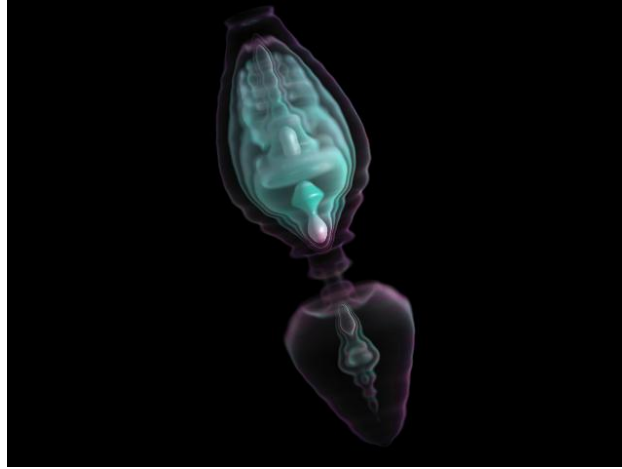


Figure 3.2: A rendering of the iso-surfaces of a reconstructed planetary nebula by Magnor et al. [Magnor et al. 2004]. Image courtesy of Marcus Magnor [Magnor et al. 2004]

There are several papers in the astrophysical literature which approach the reconstruction of astronomical objects. Planetary nebulae are well suited candidates because of the high percentage showing cylindrical symmetry. Volk and Leahy [Volk and Leahy 1993] present an approach to deproject ellipsoidal shape nebulae by deprojecting discretized cuts from the input images, while integrating Lucy [Lucy 1974] deconvolution. Bremer [Bremer 1995] proposes an iterative algorithm which is able to recover distributions in synthetic nebulae with inclinations up to  $60^\circ$ . The method can handle deconvolution and a Poisson noise model.

Knuth and Hajian [Knuth and Hajian 2002] use a Bayesian approach and propose a hierarchical model which infers the size, orientation, shape, expansion rate and mass distribution of selected planetary nebulae. The authors use an adapted version of the ionization-bounded prolate ellipsoidal shell model [Aquist and Kwok 1996] to fit their model parameters such that the final nebula resembles best the input image.

Generally computed tomography only accounts for the attenuation due to absorption through the imaged volume. There are tomographic reconstruction algorithms that consider scattering in the reconstructed volumes [Bronnikov 1999] or even diffuse propagation [Arridge 1999]. However, they always build on observations from different projection directions. We present in Chapter 7 a method for joint reconstruction of dust and gas in planetary nebulae considering absorption and scattering, based on images from a single viewpoint.

### 3.4 Augmented Reality Applications

Most augmented reality applications that perform tracking are concerned with tracking the user's head and / or body movements in order to determine its position and orientation [Azuma 1997, Bimber and Raskar 2005]. In contrast, in our approach presented in Chapter 8, the telescope together with the projection unit are moving on a fixed tripod pointing to the sky hemisphere, with two degrees of freedom. Our system constantly queries the position of the telescope and synchronizes it with the projected sky section.



Figure 3.3: Celestron Sky Scout Personal Planetarium. The user selects a desired object, points the device to the sky and she / he is guided into the direction of the object by arrows inside the viewfinder. Additional information and audio guides for many astronomical objects are provided as well. Image courtesy of Celestron [Celestron, LLC. 2006]

There are two related, recently developed commercial products from Celestron and Meade respectively, two of the major telescope manufacturing companies. They are the Celestron Sky Scout [Celestron, LLC. 2006] (Figure 3.3) and the Meade mySKY [Meade Instruments Corp. 2007] (Figure 3.4). Both devices are small, stand alone and portable; they assist an observer of the night sky to easier identify astronomical objects. None of the devices highlights optical magnification, they are thought as naked eye visual observing guides, though they can be integrated with Meade and Celestron computer controlled telescopes up to some extent. While the Celestron Sky Scout does not have a color LCD display, the Meade mySKY is able to display images and video on a 480 x 234 pixel color display. We want to mention that both devices came on the market some time after



the publication of our papers related to the subject [[Lințu and Magnor 2005](#), [Lințu and Magnor 2006](#)].

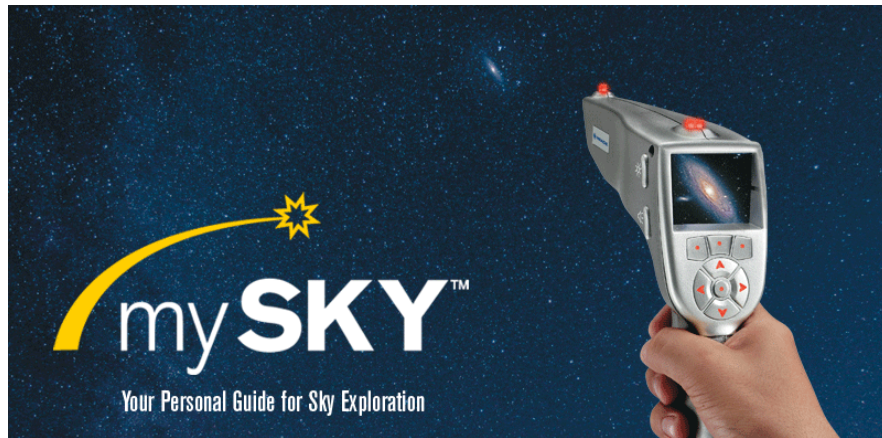


Figure 3.4: Meade mySKY. Similar to the Celestron Sky Scout, this tool has a pointing device like form and contains a small LCD display. Image courtesy of Meade [[Meade Instruments Corp. 2007](#)]

A similar application developed after the publication of our approach (but unknowing of it) is the so called *Dinocular* (Figure 3.5), by the amateur astronomer Martin Neumann from Köln. The idea is very similar to the one presented in this chapter, that is to project additional images directly in the eyepiece view of an astronomical telescope. The projection unit was hand built by Dr. Neumann and uses an 3–4” commercially available LCD display, a black cloth covering the construction in a prism-like form. The LCD image is projected by a custom built lens through a pinhole in the 45° mirror directly into the eyepiece view of the telescope on which the projection unit is mounted. The resolution of this projection unit is well below resolution and sharpness achieved with our custom projection module (Section 8.5), but it is much cheaper and easier to manufacture. If the means of the system is just to project an overlay image of a deep-sky object, resolution and sharpness do not play such an important role.

In the optical industry there are several patents on related applications. Beamon [[Beamon 1990](#)] proposes a system where a stereo image is projected on two small displays situated in front of the user’s eye. Ellenby et al. [[Ellenby et al. 1997](#)] describe a system for augmenting real images of a scene based on the tracked orientation of the user. A technique to enhance the contrast between the projected virtual image and the visible background by first projecting a darkened mask is introduced by Melville [[Melville 1999](#)]. All previously mentioned patents

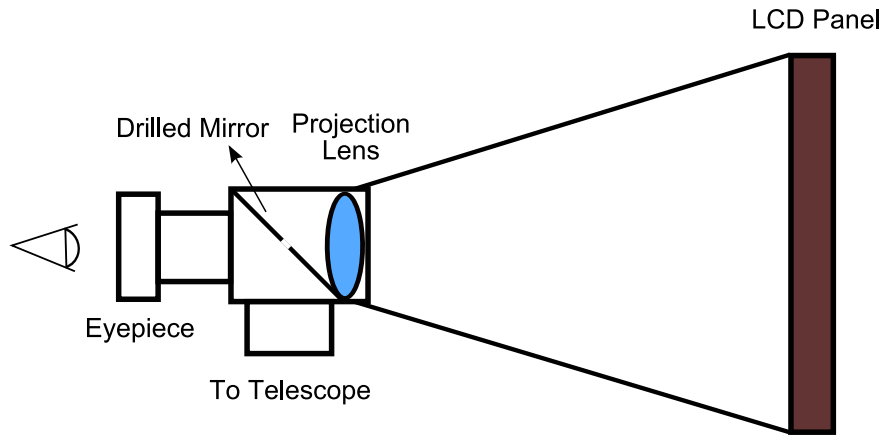


Figure 3.5: Schematic side-view of the projection unit developed by Martin Neumann. The image on the LCD panel is projected through the small pinhole on the mirror directly in the eyepiece view

are neither designed for night vision nor provide a comprehensive database of the visible objects.

The system developed by researchers at the Fraunhofer IGD [Stricker 2005, Zoellner et al. 2005] uses a *video see-through* approach. This work focuses on boosting the performance of a coin-operated telescope by equipping it with a display, a standard PC, a hardware tracking device and a camera. Thus the system can be used to augment views of the attraction sites where the telescope is installed. Reeves et al. [Reeves et al. 2005] depict another example of a video see-through application that allows the visitors to an exhibition to gather additional information about some of the presented objects. For both previously described applications, the telescope's optical assembly is not utilized. It is replaced by a video camera with a telephoto lens. Conversely, in our application the optical assembly of the telescope is of major importance, its main function of *light gathering* is kept. The hereby proposed system is an *optical see-through* application, so that the genuine visual impression given by the observed objects is maintained. A conceptual presentation of the system can be found in [Lințu and Magnor 2005].

Birkfellner et al. [Birkfellner et al. 2000] present a related optical see-through application. The authors propose a head-mounted display customized for medical applications such as an on-line aid during surgery. The optical setup of the system uses image rectification prisms to project the visual and the display image onto a common focal plane. Because of the relatively small magnifications available (3.6 x – 7.2 x) the whole optical assembly is relatively small and can be used as a head-mounted display.

Optical see-through head mounted displays have only recently reached contrast ratios of 1:200 – 1:300 [[Nvis Inc. 2005](#), [Cybermind Interactive Nederland](#)]. The designed projection unit for our system provides even higher contrast ratio (1:500), and has the advantage of being able to be incorporated in applications that require optical magnification.



## **Part II**

# **Rendering of Astronomical Objects**



# Overview

This part of the thesis deals with the rendering of selected astronomical objects, considering scattering and absorption.

We first present an approach to rendering realistic solar disc images at sunset or sunrise, for given climates and height to temperature profiles in the atmosphere, in Chapter 4. The hue of the solar disc can be reproduced for different humidity values and different aerosol distributions in the atmosphere. We can also reproduce specific mirage phenomena such as the green flash, the red flash or the omega sun.

Chapter 5 describes an interactive and physically correct visualization tool for reflection nebula volumetric datasets. We simulate the light transport in these type of astronomical objects which consist of one or more emissive stars which illuminate the clouds of dust surrounding them. Because of scattering and absorption, the appearance of these type of objects varies strongly with the viewpoint. Using our visualization tool, planetarium artists as well as astrophysicists can interactively investigate reflection nebula datasets. We use synthetic datasets for our visualizations in Chapter 5. Part III will present methods to reconstruct the 3D distribution of reflection and planetary nebulae.





---

## Chapter 4

# Realistic Solar Disc Rendering

In this chapter we concentrate on rendering the solar disc considering Rayleigh scattering, Mie scattering, absorption, and refraction. The atmosphere is modeled in layers, each layer having a set of individual optical properties. Based on different atmospheric temperature profiles and climates, the solar disc is rendered in realistic shape and color. In particular, we replicate optical phenomena such as the red and the green flash, limb darkening, and refractive distortions of the solar disc.

### 4.1 Introduction

Computing a physically and visually correct reproduction of the colors of the sky dome around the observer is an essential task for outdoor scene renderings. Although some work has been done on the simulation of the sky colors during daytime [[Preetham et al. 1999](#), [Nishita et al. 1996](#)], nighttime [[Wann Jensen et al. 2001](#)], and twilight periods [[Haber et al. 2005](#)], realistic rendering of the solar disc has received little attention in the literature so far. In order to achieve realistic renderings, the optical phenomena occurring in the atmosphere need to be considered. Based on the physical structure of the Earth's atmosphere, this paper reproduces solar disc appearances at sunrise/sunset in correct form and color. We take into account Rayleigh scattering due to air molecules as well as Mie scattering due to aerosols present in the atmosphere, thus obtaining a realistic color of the solar disc.



Figure 4.1: A sunset scenario in a polluted maritime climate, few minutes before the Sun is setting

To obtain the correct shape of the solar disc, we also model refraction, allowing us to trace rays correctly through the atmosphere.

Based on the actual structure of a given input atmosphere model, i.e. height-dependent temperature profile and distribution of aerosols, we observe different colors and shapes of the solar disc. The color of the disc varies with the climate, its shape differs due to mirage phenomena. By rendering the Sun taking different wavelengths into account, chromatic aberration phenomena such as the green flash or the red flash can be reproduced.

After an introductory review of the physics in Section 4.2, we give a system overview in Section 4.3. We describe our approach on solar disc rendering in Section 4.4. Results are presented in Section 4.5, before we conclude and point to future work in Section 4.6.

## 4.2 Sunset Science

Our approach for rendering the solar disc is able to faithfully reproduce a variety of optical phenomena such as mirages and chromatic aberrations. In the following,

we give physical descriptions of these phenomena.

### 4.2.1 Mirages

Mirages are caused by strong ray-bending due to steep temperature gradients in the atmosphere [Minnaert 1954]. According to the position of the mirrored images relative to the original object, mirages can be classified into two main categories:

- inferior mirages: mirrored image below object
- superior mirages: mirrored image above object

The *inferior mirage* occurs if a layer of hot air is close to the ground, bending the grazing rays upwards. It can be observed in deserts or above asphalt paving on sunny days. An example of this mirage is presented in Figure 4.3, the so called *Omega sunset*.

For the *superior mirage* to take place, the observer has to be situated *inside* a layer of air with a thermal inversion, i.e. there is a sudden increase in temperature above the observer. The rays in this duct intersect after traversing kilometers through the atmosphere, creating the inverted image of a distant object. In the case of the superior mirage, the intersecting rays remain inside the inversion layer. Thus superior mirages do not occur of astronomical objects that are situated outside the Earth's atmosphere.

If the observer is above a thermal inversion layer the just recently understood *mock mirage* can occur [Young 1999 - 2004]. In this case the intersecting rays can escape the Earth's atmosphere, the intersection points being far away from the observer.

A large variety of mirages can occur. They are highly dependent on the altitude of the observer. In order to be able to see a solar disc mirage, at least one temperature inversion layer has to be present in the atmosphere at the time of observation. This inversion layer produces a sudden change in the refraction index of the air, thus creating a mirage.

### 4.2.2 The Green Flash

This peculiar optical phenomenon consists of a short green flash (lasting only a few seconds) that can appear on top of the solar disc when at sunset or sunrise. It is due to the large variation of refraction and induced dispersion close to the horizon.

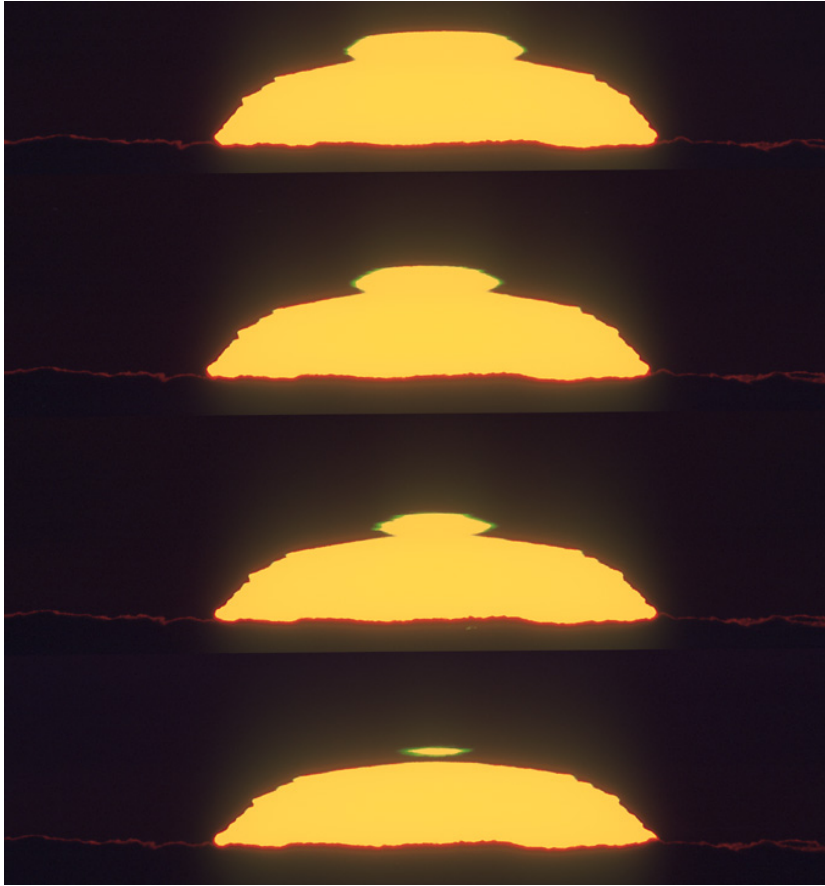


Figure 4.2: Photograph of a Green Flash Sequence

Photograph by Mario Cogo [[Cogo 1996 - 2004](#)], used with permission

There are several types of green flashes, each one being associated with a mirage phenomenon. The green color is mainly due to *atmospheric dispersion* which makes the red component of the light spectra disappear first, followed by green, blue, and violet during sunset. Another effect contributing to the green flash is *atmospheric extinction*, which mainly consists of *atmospheric scattering* due to air molecules. In this case, the shortest wavelengths are almost completely removed. Therefore, it is sometimes possible to observe only the *green* component of the light spectra for a few seconds during sunset.

The green flash phenomenon depends also on the adaptation of the human visual system during observation [[Young 2000](#)]. The high intensity of the solar disc bleaches the red-sensitive photo-pigments on the retina, thus allowing also yellow flashes to be perceived as green.

In Figure 4.2 a sequence of photographs of this phenomenon are presented. Figure 4.14 illustrates a simulation generated using our system. An exhaustive explanation and bibliography of this phenomenon can be found in [Young 1999 - 2004].

### 4.2.3 The Red Flash

Another type of mirage, which is harder to observe than the green flash, is the red flash. The red flash can occur due to a *mock mirage*, where it consists of a round red “droplet” below the “cropped” solar disc (see Figure 4.3, left), or as a consequence of an *inferior mirage*, where it is visible as a red middle region of the *Omega sunset* (see Figure 4.3, right). Also to note is that this mirage is harder to observe visually because of the small hue differences between the yellowish – red solar disc and the red flash itself.

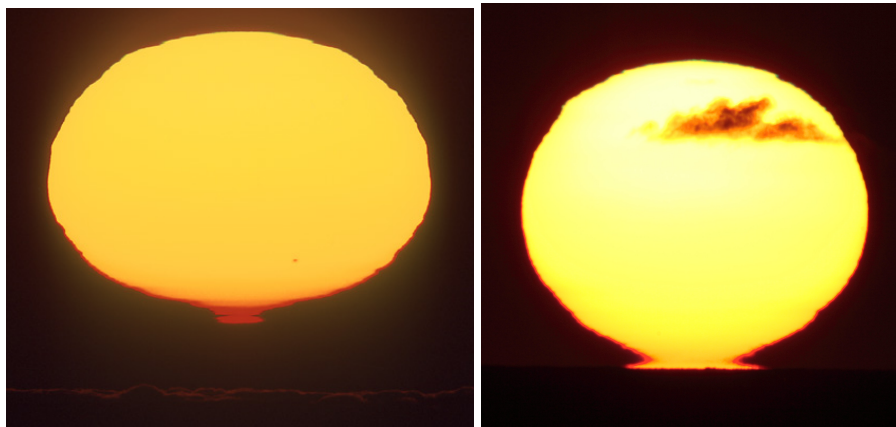


Figure 4.3: Left: Photograph of a Red Flash by Mario Cogo [Cogo 1996 - 2004], used with permission. Right: Photograph of an Omega Sunrise, with a slight red flash visible at the bottom part

### 4.2.4 Limb Darkening

This phenomenon consists of the darkened outer rim of the solar disc, as visible in Figure 4.4. It is due to the fact that light from the center of the Sun traverses less gas of the Sun’s photosphere where it is partially absorbed.

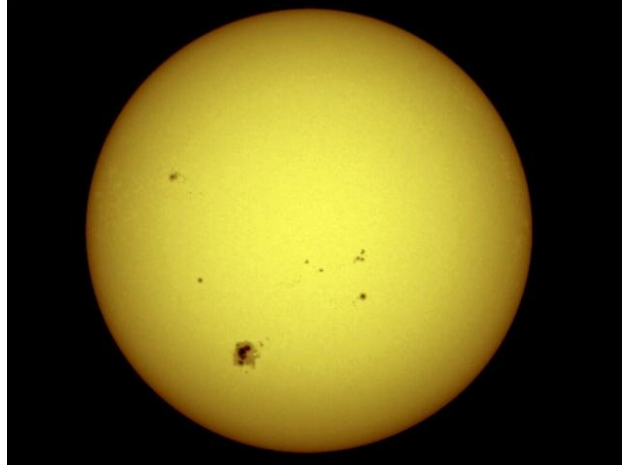


Figure 4.4: A Photograph of the Solar photosphere highlighting visible limb darkening, from [NASA b]

Limb darkening can be phenomenologically described by

$$I'(\lambda) = I(\lambda) \cdot \left( 1 - u \cdot \left( 1 - \sqrt{1 - \frac{d^2}{r^2}} \right) \right),$$

where  $I$  is the solar irradiance,  $d$  is the distance from the center of the Sun,  $r$  is the radius of the solar disc, and  $u$  is the limb darkening coefficient for the Sun, which is approximately 0.6 for visible sunlight [Bruton 1996].

We incorporate limb darkening in our system in order to obtain realistic renderings of the solar disc.

### 4.3 System Overview

Our solar disc rendering system combines tracing of parabolic rays through the atmosphere [Lehn 1985, Bruton 1996] with an atmosphere model incorporating different climate-dependent characteristics [Haber et al. 2005] to reproduce both the correct *shape* of the solar disc and its corresponding correct *color*. The used atmosphere model incorporates the scattering and absorption coefficients for Rayleigh scattering and Mie scattering. The effects of different climate types, air humidities, and atmosphere temperature profiles on the appearance of the solar disc at sunset or sunrise are simulated.

Ray-tracing through the atmosphere is computed using Lehn's parabolic model for a light ray traveling through an atmosphere layer [Lehn 1985]. This model

reduces the amount of computation time otherwise required to solve the Eikonal PDE for light rays traveling through the atmosphere. To determine the distribution of the aerosols in the atmosphere we use the OPAC software package [Hess et al. 1998, Hess 1998].

As input to our simulations, in addition to the required climate type and temperature profile, we also specify *observer height*.

We now give a short, step by step description of the used method:

- specify input: *temperature profile, climate, number of layers* and *observer height*;
- precompute the *radius of curvature* for the parabolic ray approximations;
- compute *solar disc shape* – ray-trace through the atmosphere model and compute the length the rays travel through each layer;
- compute *solar disc color* – multiply the initial intensity with the extinction factor;

## 4.4 Solar Disc Rendering

In this section we describe the atmosphere model and the ray-tracing mechanism used in our simulations.

### 4.4.1 Extinction Coefficients

To determine the optical properties of the *aerosols* present in the atmosphere, we use the publicly available OPAC software package [Hess et al. 1998, Hess 1998]. Using this package we compute wavelength-dependent aerosol absorption coefficients  $\sigma_a^{\text{aerosol}}(\lambda)$ , scattering coefficients  $\sigma_s^{\text{aerosol}}(\lambda)$ , and anisotropy factors  $g(\lambda)$  for the given input climate type of an arbitrary aerosol composition and humidity.

Values for the wavelength-dependent scattering coefficient  $\sigma_s^{\text{air}}(\lambda)$  of *air* molecules are taken from Nagel et al. [Nagel et al. 1978]. Pure air does not significantly absorb visible light. Thus, the extinction coefficient of air  $\sigma_e^{\text{air}}$  is assumed to be equal to the scattering coefficient,  $\sigma_e^{\text{air}}(\lambda) = \sigma_s^{\text{air}}(\lambda)$ .

### 4.4.2 Atmosphere Model

The atmosphere model used in our system is stratified, consisting of atmosphere layers located geocentrically around the surface of the Earth.

The height of individual layers is chosen such that approximately the same amount of molecules is contained in each one of them. Our atmosphere model reaches up to a height of  $H_{\max} = 35$  km. The number of molecules above this height can be considered negligible. A schematic description of the used model is depicted in Figure 4.5.

We discretize the atmosphere into a set of geocentric atmosphere layers  $L_i$ , ( $i = 1, \dots, N$ ). Each layer  $L_i$  has an individual upper and lower boundary at height  $H_{i,\max}$  and  $H_{i,\min}$ , respectively. To each layer  $L_i$  we assign the relative humidity  $w_i$  and the following optical parameters:

- aerosol scattering coefficient  $\sigma_{s,i}^{\text{aerosol}}(\lambda)$  and extinction coefficient  $\sigma_{e,i}^{\text{aerosol}}(\lambda) = \sigma_{s,i}^{\text{aerosol}}(\lambda) + \sigma_{a,i}^{\text{aerosol}}(\lambda)$ ;
- Henyey-Greenstein scattering anisotropy coefficient  $g_i(\lambda)$ ;
- isotropic scattering coefficient of air  $\sigma_{s,i}^{\text{air}}(\lambda)$ ;
- mean index of refraction  $\eta_i(\lambda)$  and indices of refraction  $\eta_{i,\min}(\lambda)$  and  $\eta_{i,\max}(\lambda)$  corresponding to  $H_{i,\min}$  and  $H_{i,\max}$ , respectively.

All these parameters are functions of the wavelength  $\lambda$  and are evaluated for a discrete number of wavelengths. A more detailed description of the used layered atmosphere model can be found in [Haber et al. 2005].

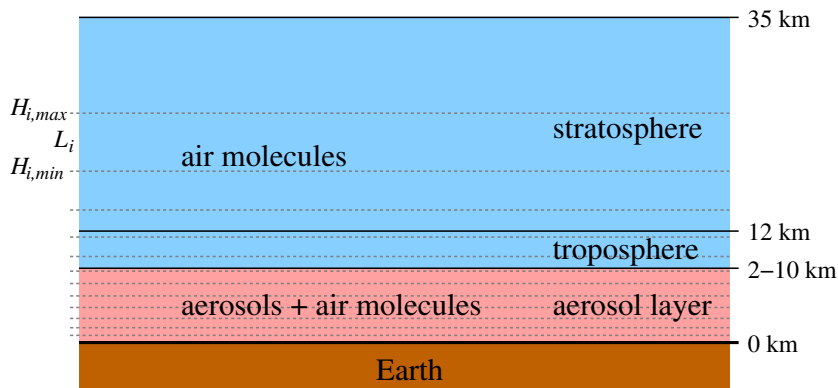


Figure 4.5: Cross section of the atmosphere model. It is composed of an aerosol-containing region, clear troposphere and stratosphere [Hess et al. 1998]. For the aerosol region the height is climate dependent.



The simulations presented in this paper are typically computed using 300–30000 layers, depending on the input temperature profile. The number of input layers is dependent on the height of the inversion layers. For a thermal inversion layer close to the surface of the Earth, we need a fine sampling of our atmosphere model in order to be able to correctly simulate the corresponding mirage, due to the exponential distribution of the atmosphere layers.

The solar irradiance  $I_0(\lambda)$  outside the atmosphere, i.e. before the sun light reaches the ozone layer, is computed from the solar spectrum data measured by Kurucz [Kurucz et al. 1984] for wavelengths from 200 nm to 1000 nm. We filter the solar irradiance using the approach presented in [Haber et al. 2005], accounting for wavelength-dependent absorption in the ozone layer.

### 4.4.3 Temperature Profiles

Our simulations are based on temperature profiles of the atmosphere, the starting point being the U.S. Standard Atmosphere [Bruton 1996, Young 1999 - 2004]. In order to simulate different mirage phenomena, several input height-temperature profiles differing from the U.S. Standard Atmosphere are used. The profile of the atmosphere is specified as the temperature gradient at discretized heights.

### 4.4.4 Atmospheric Refraction

A model based on exact computation of refraction taking place in the atmosphere requires numerically solving a PDE and is computationally too expensive to be practically useful. The simplest solution is to assume all rays traveling linearly through each layer. We chose to implement a quadratic-error model developed by Lehn [Lehn 1985]. This model assumes that the circular arcs representing the Earth's surface, the light rays, and the layer boundaries of the atmosphere model can be locally approximated by parabolas.

Taking into consideration the specified atmosphere temperature profile, climate and humidity for the current rendering, parameters regarding to the used model can be computed before the actual ray-tracing process. For each layer  $L_i$  we pre-compute the wavelength-dependent radius of curvature  $\kappa_i(\lambda)$  using

$$\kappa_i(\lambda) = -K \cdot \eta_i(\lambda) \cdot \frac{(H_{i,\max} - H_{i,\min})}{(\eta_{i,\max}(\lambda) - \eta_{i,\min}(\lambda))},$$

where  $\eta_i(\lambda)$  is the mean index of refraction of air in layer  $L_i$ , and  $\eta_{i,\max}(\lambda)$ ,  $\eta_{i,\min}(\lambda)$  are the refractive indices of air corresponding to the upper and lower

heights  $H_{i,\max}$  and  $H_{i,\min}$ . The value for  $K$  depends on the initial parameters in the ray-tracing process and can be found in Bruton's thesis [Bruton 1996]. The rays are traced through the atmosphere starting from the layer containing the observer.

In Figure 4.6, the two possible cases of the intersection between the currently traced ray and the boundaries of an atmosphere layer are depicted. The expected trajectory of the ray is denoted as Path 1. However, if a thermal inversion is present, the ray can bend downwards following Path 2.

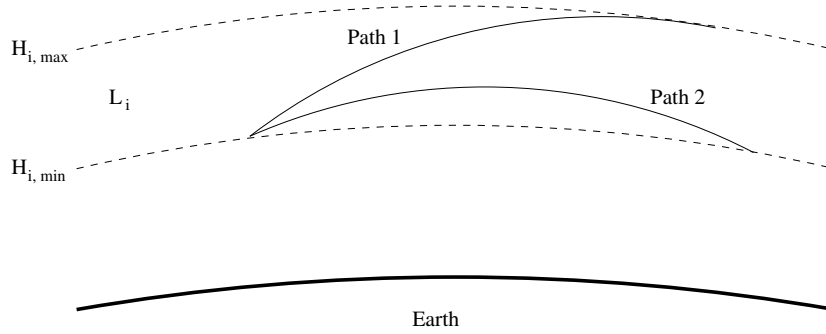


Figure 4.6: Two possible ray paths through the atmosphere. Path 1 depicts the normal trajectory of a ray traveling through layer  $L_i$ . For a thermal inversion present in  $L_i$ , the ray trajectory may follow the path indicated as Path 2.

The distance  $\Delta\gamma_i(\lambda)$  that a light ray of wavelength  $\lambda$  travels through layer  $L_i$  is numerically determined by

$$\Delta\gamma_i(\lambda) = 2 \cdot \kappa_i(\lambda) \cdot \arcsin\left(\frac{d}{2 \cdot \kappa_i(\lambda)}\right) \quad (4.1)$$

with

$$d = \sqrt{\Delta x^2 + \left(\Delta z - \frac{\Delta x^2}{2R}\right)^2}.$$

The values for  $\Delta x$  and  $\Delta z$  are computed during the ray-tracing process through the atmosphere layers as described by Lehn [Lehn 1985] and Bruton [Bruton 1996]. Based on the current optical parameters during ray-tracing, for each layer  $L_i$  a decision is taken [Lehn 1985, Bruton 1996] whether Path 1 or Path 2 is chosen for the current ray (see Figure 4.6).

In order to accurately compute the indices of refraction for each atmosphere layer based on the input temperature profiles, we employ the formulas proposed by Ciddor [Ciddor 1996]:

$$\eta_{h,w}(\lambda) = 1 + \frac{\rho_a}{\rho_d} \cdot (\tilde{\eta}_d - 1) + \frac{\rho_v}{\rho_w} \cdot (\tilde{\eta}_w - 1),$$

where  $\rho_d$  is the density of dry air at 15°C and 101325 Pa,  $\rho_w$  is the density of pure water vapor at 20°C and 1333 Pa, and  $\rho_a$  and  $\rho_v$  are the densities of the dry air component and water vapor component for the current conditions. The equations needed to calculate the air densities in the above formula are given by Ciddor [Ciddor 1996]. To compute the values for  $\tilde{\eta}_d$  and  $\tilde{\eta}_w$ , the following equations are used [Ciddor 1996]:

$$\tilde{\eta}_d(\lambda) = 1 + \left( \frac{5792105.0}{238.0185 - \lambda^{-2}} + \frac{167917.0}{57.362 - \lambda^{-2}} \right) \cdot 10^{-8}$$

$$\tilde{\eta}_w(\lambda) = 1 + (295.235 + 2.6422 \lambda^{-2} - 0.03238 \lambda^{-4} + 0.004028 \lambda^{-6}) \cdot 1.022 \cdot 10^{-8}.$$

#### 4.4.5 Atmospheric Extinction

To accurately determine the color of each pixel in the rendered images, we first compute the intensity  $I(\lambda)$  of sun rays that reach the observer *after extinction* in the atmosphere according to:

$$I(\lambda) = I_0(\lambda) \cdot \xi_\gamma(\lambda), \quad (4.2)$$

where  $I_0(\lambda)$  is the solar irradiance filtered by absorption in the ozone layer and the extinction factor  $\xi_\gamma(\lambda)$  is given as:

$$\xi_\gamma(\lambda) = \exp \left( - \int_\gamma \left( \sigma_e^{\text{aerosol}}(\lambda) + \sigma_e^{\text{air}}(\lambda) \right) ds \right).$$

The value for the extinction factor  $\xi_\gamma(\lambda)$  is numerically determined by

$$\xi_\gamma(\lambda) = \exp \left( - \sum_{i=1}^N \left( \sigma_{e,i}^{\text{aerosol}}(\lambda) + \sigma_{e,i}^{\text{air}}(\lambda) \right) \cdot \Delta\gamma_i(\lambda) \right), \quad (4.3)$$

where  $\Delta\gamma_i(\lambda)$  denotes the path length through layer  $L_i$ , see Equation (4.1).

We take into account both multiple Rayleigh scattering (by air molecules) and Mie scattering (by aerosols). Mie scattering is modeled using the well-known Henyey-Greenstein approximation [Henyey and Greenstein 1941]. For rendering the solar disc, the phase angle (i.e. the angle between incident light and scattering direction)

in this approximation can be considered equal to zero, since the diameter of the solar disc is merely  $0.5^\circ$ . As a consequence, the extinction factor  $\xi_\gamma(\lambda)$  from Equation (4.3) is modified as follows:

$$\begin{aligned}\xi'_\gamma(\lambda) &= \exp\left(-\sum_{i=1}^N \sigma_{e,i}^{\text{mult}}(\lambda) \cdot \Delta\gamma_i(\lambda)\right), \\ \sigma_{e,i}^{\text{mult}}(\lambda) &= (1 - g(\lambda)) \cdot \sigma_{e,i}^{\text{aerosol}}(\lambda) + \sigma_{e,i}^{\text{air}}(\lambda).\end{aligned}\tag{4.3'}$$

Substituting  $\xi'_\gamma(\lambda)$  for  $\xi_\gamma(\lambda)$  in Equation (4.2) yields the final formula to compute the intensity  $I(\lambda)$ .

#### 4.4.6 Gamma Correction

For the final rendering, we convert the sampled spectral distribution into its corresponding color in XYZ color space by convolution with the CIE (1964)  $10^\circ$  color matching functions. Due to the high dynamic range of intensities, we have to apply gamma correction to faithfully display our results. We thus transform from XYZ color space to xyY color space and perform gamma-correction on the Y-value:

$$Y' = Y^{1/\bar{\gamma}},$$

where we use  $\bar{\gamma} = 2.5$  for the correction coefficient. Finally, we convert back to XYZ and from XYZ to RGB color space using the sRGB primaries from CIE Rec. 709 and a D<sub>65</sub> whitepoint. For details of these spectral conversions see the textbooks by Wyszecki et al. [Wyszecki and Stiles 1982] or Hall [Hall 1989].

### 4.5 Results

We have rendered a variety of sunset sequences for different meteorological conditions using the approach presented in this paper. To obtain a large diversity of solar disc renderings, various aerosol distributions, air humidity values, and temperature profiles of the atmosphere have been used.

Figure 4.1 shows a sunset scenario for a polluted maritime climate with 80% humidity. A polluted urban climate with 80% humidity has been used to simulate the sunset depicted in Figure 4.7. The sunset reproduced in Figure 4.8 has been

simulated for a continental climate with 70% humidity. For all of the above mentioned images, the colors of the sky have been computed and rendered using the approach presented in [Haber et al. 2005].



Figure 4.7: Rendering of a sunset in a polluted urban climate with 80% humidity

All images presented in this paper have been generated using a discretization of  $N_\lambda = 8$  wavelengths in the range from 380 nm to 720 nm. Depending on the number  $N$  of atmosphere layers used for the simulations and the resolution of the generated images, computation times on a 2.4 GHz Pentium4 PC are in the range of a few minutes for our unoptimized implementation.

Figures 4.9 and 4.10 show the effect of varying humidity on the appearance of the solar disc at sunset or sunrise. With increasing air humidity the solar disc becomes noticeably darker.

The consequences of the presence of a temperature inversion layer close to the ground are depicted in Figure 4.11. This is the so called *Omega Sun*, the form of the solar disc being reminiscent of the Greek letter  $\Omega$ . Figure 4.12 highlights in comparison a photograph of a similar sunrise sequence. Note the red flash visible in the rightmost stage of the sunrise.

The red flash is simulated in Figure 4.13. An atmosphere containing a weak inversion layer is used here to simulate a mock mirage for an observer situated at an altitude of 45 m above sea level.

In Figure 4.14, a green flash is replicated. The atmosphere is identical to the one used in Figure 4.13. Here, however, the Sun is at a lower altitude. The difference in altitude between successive renderings is below one arc-minute.



Figure 4.8: Rendering of a sunset for a continental climate with 70% humidity

## 4.6 Conclusion

A system for realistic rendering of the solar disc has been presented. Atmospheric optical phenomena such as mirages, red and green flash, and limb darkening are simulated based on physical laws and meteorological conditions. In order to validate the obtained results, one future research direction is to calibrate the rendered images with real life photographs of sunsets. Furthermore, due to the large variation in extinction of various climates, which are reflected in the high dynamic range of our obtained results, an efficient tone mapping operator should be developed.

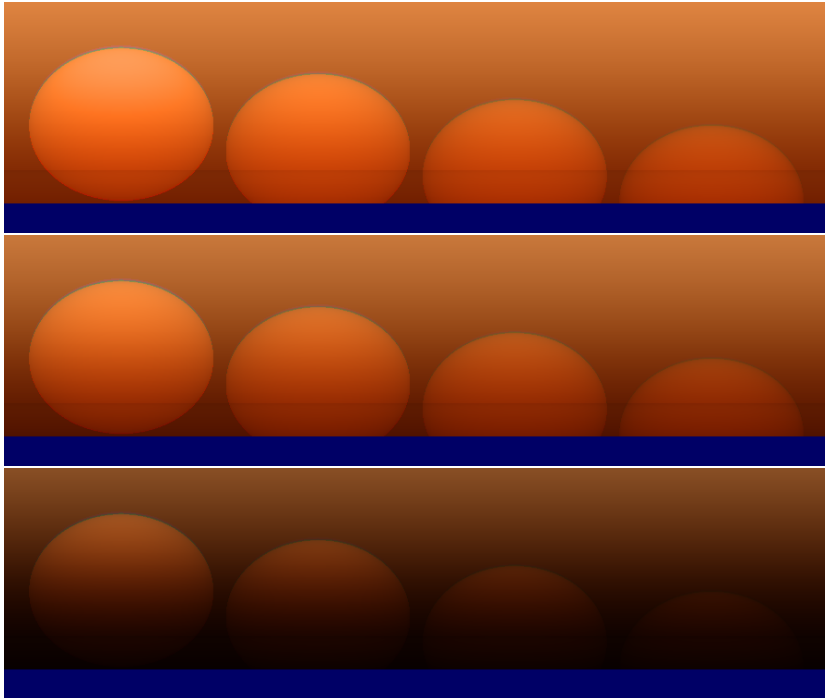


Figure 4.9: Rendering of a sunset in continental climate for different humidities. Top to bottom: 50%, 80%, and 95% humidity

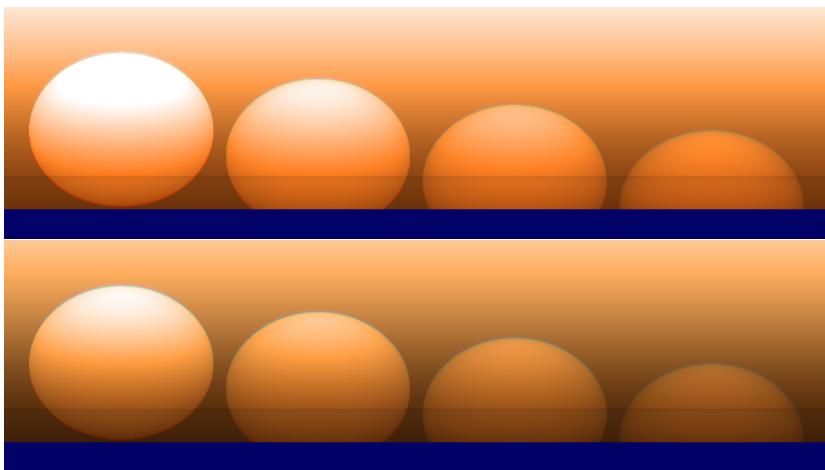


Figure 4.10: Rendering of a sunset in tropical maritime climate for 80% (top) and 90% (bottom) humidity.

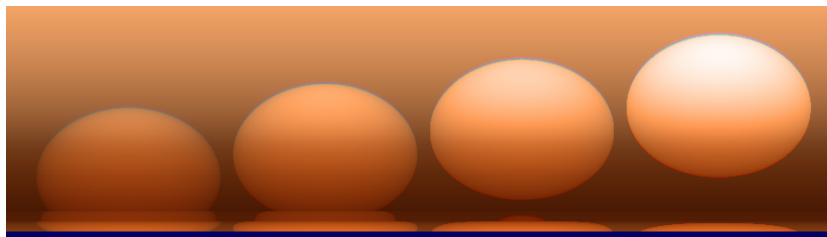


Figure 4.11: Rendering of an omega sunset sequence. It frequently occurs in desert climates. A strong inversion layer right above the ground causes this inferior mirage



Figure 4.12: Photographs of an omega sunrise sequence recorded on La Palma, Spain. The camera was situated approximately 100 meters above sea level

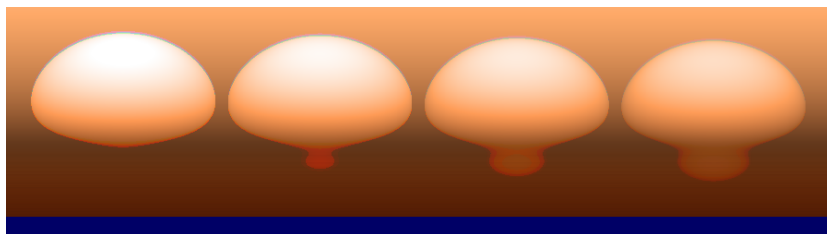


Figure 4.13: Rendering of the red flash—a frequent mirage, hardly observed because of the small hue difference between the color of the solar disc and that of the flash

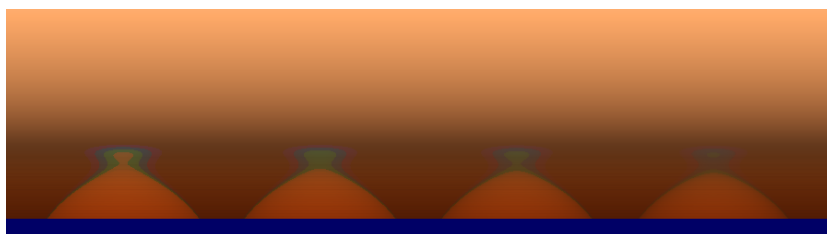


Figure 4.14: Rendering of the green flash resulting from a mock mirage



---

---

## Chapter 5

# Reflection Nebula Visualization

Reflection nebulae are clouds of dust in space illuminated by one or more stars. In a reflection nebula, light is typically emitted from a central star and then scattered and partially absorbed by the nebula's dust particles. We model the light transport in this kind of nebulae by considering absorption and scattering and design an interactive visualization tool which enables astrophysicist as well as planetarium artists too analyze and simulate the effects on the appearance of these nebulae with changing viewpoint.

### 5.1 Introduction

3D models and visualizations of astronomical objects are becoming more and more important nowadays. They are widely used as a tool to prove existing astrophysical theories and to determine various properties of a given astronomical object [[Gordon et al. 2001](#), [Wood et al. 2004](#)]. They are further used in today's modern planetariums, in which the number of digital video projectors available increased significantly. Realistic 3D flybys of astronomical objects in planetarium shows are becoming rather the rule than the exception [[Evans and Sutherland 2000](#)]. However, most of these animations are created by talented graphical artists; in many cases the structure and morphology of the original objects is widely unknown, and therefore the created volume has little in common with astrophysical certainties.

Reflection nebulae (Figure 5.1) are clouds of dust which are illuminated by one or more stars. Scattering and absorption plays an important role in the appearance

of these type of astronomical objects which can change their appearance greatly with the viewpoint. As observers on Earth have a fixed point of view towards astronomical objects, it is of interest for astrophysicists as well as astronomy educators to be able to inspect the appearance of reflection nebulae from several other viewpoints. This can be practically achieved only by modelling the physical phenomena which take place in these nebulae and by producing synthetic or recovering the 3D dust distribution in reflection nebulae.

In this chapter we address the problem of physically accurate visualization of reflection nebulae by developing a physically accurate visualization tool which takes into account the wavelength dependant effects of scattering and absorption which occur in these objects. As we can simulate on the fly changes in viewpoint but also in physical constants relevant for the appearance of these type of astronomical objects, the developed tool is of interest for planetarium artists as well as for astrophysicists.



Figure 5.1: The NGC 2023 reflection nebula in Orion (image courtesy of Robert Gendler [[Gendler 2007](#)]). The cloud of dust is illuminated by the central star

## 5.2 Reflection Nebula Physics

Reflection nebulae are clouds of dust surrounding one or more young, recently formed stars [[Binney and Merrifield 1998](#)]. The stars in these nebulae are not

hot enough to ionize the gas around them but their light is strong enough, so that the reflected light can be observed (see Figure 5.1). Their wonderful colors are due to the light of the central star which is scattered and attenuated by the dust surrounding it.

The blue colors seen in these nebulae are mostly due to scattering. This is due to the fact that light at blue wavelengths scatters much more than light at the red end of the visible electromagnetic spectrum. The best example which demonstrates this is the color of the sky; it is blue because it consists of sunlight scattered by the particles in the atmosphere. All reddish colors visible in reflection nebulae account for absorption, the light from the central star gets attenuated and reddened on its way to an observer on earth.

### 5.2.1 Interstellar Dust

The physics behind reflection nebulae is actually the physics of the interaction of light with interstellar dust particles. We create a physically-based model of light scattering in interstellar dust using a set of scalar parameters. At single particle level, this interaction can be characterized by Mie scattering theory [van de Hulst 1982]. However, for a very large number of particles, astrophysicists use simplified models such as the one proposed by Henyey and Greenstein [Henyey and Greenstein 1941] which is described by two scalar parameters. One is the *albedo*  $\alpha$ , which indicates how much light the particles reflect: 0 for total absorption i.e. black dust and 1 for the case where all incident light is scattered. With  $\sigma_{\text{sct}}$  as the scattering coefficient and  $\sigma_{\text{abs}}$  the absorption coefficient, albedo is always defined as the ratio between the scattered light and the light that is extincted

$$\alpha = \frac{\sigma_{\text{sct}}}{\sigma_{\text{abs}} + \sigma_{\text{sct}}} = \frac{\sigma_{\text{sct}}}{\sigma_{\text{ext}}}.$$

In our calculations, we set  $\alpha = 0.6$  [Gordon 2004b]. In addition, the presence of dust also attenuates any light shining through the dust region, which can be described by an *extinction* parameter  $\sigma_{\text{ext}}$ .

The scattering is further dependent on the angle  $\theta$  between the incident and the reflected light direction. It is described by the *single particle scattering probability* modeled using the Henyey-Greenstein phase function [Henyey and Greenstein 1941]:

$$p(\theta) = \frac{1 - g^2}{2 \cdot (1 + g^2 - 2 \cdot g \cdot \cos\theta)^{3/2}}, \quad (5.1)$$

where  $g$  is an anisotropy factor for forward and backward scattering. Observations and measurements show [Gordon 2004b], that equation 5.1 describes the scattering properties of interstellar dust with a value for  $g \approx 0.6$ .

## 5.3 Color

Data in astronomy is normally acquired through different types of filters depending on the objects being observed, the most common in use is the Johnson *BVR* color system [Binney and Merrifield 1998], which largely corresponds to the RGB color-space used in computer graphics.

The scattering coefficient  $\sigma_{\text{sct}}$ , thus as well the extinction is wavelength-dependent. The *extinction*  $A$ , or *optical depth*  $\tau_{\text{opt}} = A = \sigma_{\text{ext}} \cdot l$  is the product of total path length  $l$  and the average extinction coefficient  $\sigma_{\text{ext}}$  along the way. To express the relative amount of extinction  $\tau_{\text{opt}}$  at different wavelengths  $\lambda$ , astrophysicist express relative extinction in the *B* and *R* bands relative to the *V* band. Typical values for reflection nebulae are  $A_B/A_V = 1.324$  and  $A_R/A_V = 0.748$  [Binney and Merrifield 1998].

Dust concentrations in reflection nebulae can reach high densities, the illuminating star light may be scattered not only once, but multiple times. The *scattering depth*  $\tau = \sigma_{\text{sct}} l$  denotes the average number of scattering events that a photon undergoes along a travel path length  $l$  and is directly proportional to dust particle density. Scattering anisotropy decreases with  $g^n$ , after several scattering events, the scattered light is in essence distributed isotropically over all directions. To account for multiple scattering exactly, full-fledged, computationally expensive radiative transfer simulations are required.

## 5.4 Lighting Model

Our volume renderer is based on the following lighting model: the observed radiance  $L(x, y)$  at a camera at position  $c$  is a function of the extinction  $\tau(v) = \sigma_{\text{sct}} l$ , and the albedo  $\alpha$  of every voxel  $v$  along the ray through the camera pixel:

$$L(x, y) = \int_c^\infty e^{-\int_c^v \tau(w) dw} \cdot \alpha \cdot S(v) dv, \quad (5.2)$$

where  $S(v)$  is the total in-scattering to the voxel  $v$  towards the camera due to the emission  $L_e^{\text{star}}$  of the nebula's central star(s) at position  $p^{\text{star}}$ . Considering single

scattering only,  $S(v)$  is computed as

$$S(v) = P(\tau(v), \theta) \cdot L_e^{star} \cdot e^{-\int_{p^{star}}^v \tau(w) dw} \quad (5.3)$$

incorporating the extinction on the way from the star to the voxel as well as the scattering phase function  $P$  from the star to the voxel into the direction of the camera  $c$ . Let the view direction independent part of Equation 5.3 be

$$L_{incoming} = L_e^{star} \cdot e^{-\int_{p^{star}}^v \tau(w) dw} \quad (5.4)$$

Because it is an intrinsic property for every given volume,  $L_{incoming}$  can be pre-computed for every nebula model in order to speed up rendering. The method to compute  $P$  is described in detail in Section 5.5.  $L_e^{star}$ , and  $p^{star}$  are assumed to be known. We consider the star to be positioned in the center of the volume and  $L_e^{star}$  can be looked up in astrophysical data bases for a specific nebula.

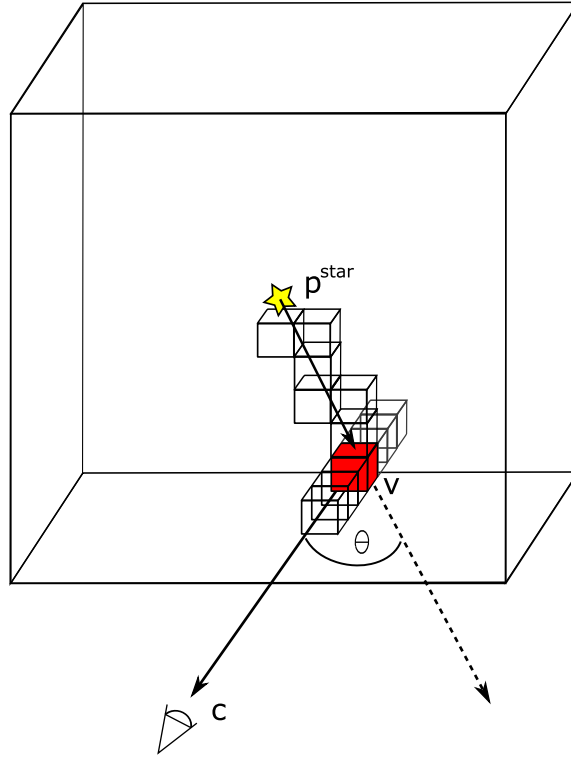


Figure 5.2: The intensity of the light reflected due to single scattering caused by the red voxel depends on the absorption along the path from the central star to the voxel, the voxels albedo, the phase function, as well as on the accumulated absorption along the remaining path towards the viewer.

## 5.5 Voxel Characteristics

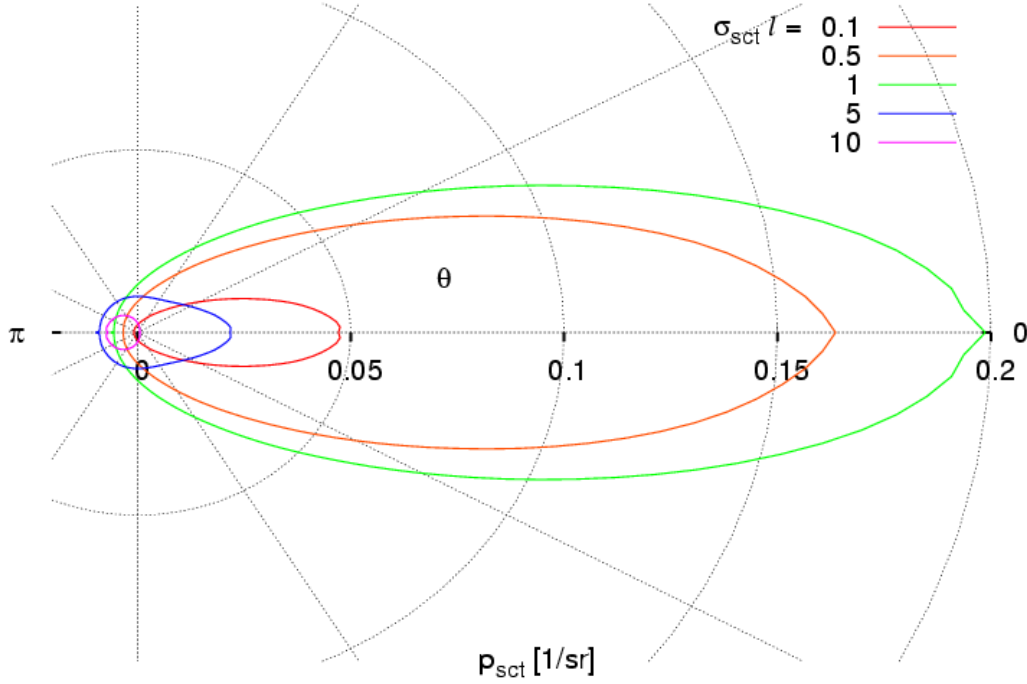


Figure 5.3: Scattering probability of a voxel  $P(\tau(v), \theta)$  with albedo  $\alpha = 0.6$  and anisotropy factor  $g = 0.6$ . The forward scattering direction is to the right ( $\theta = 0$ ). With increasing scattering depth  $\tau(v)$ , overall scattering first increases, then decreases again. Relative forward scattering also decreases until for the highest scattering depth  $\tau(v) = 10$ , more light is actually being scattered backward than forward due to extinction within the voxel volume

The fraction  $P(\tau(v), \theta)$  of illumination radiance that is scattered from the voxel into the viewing direction depends on the scattering depth  $\tau(v)$  (dust density) of the voxel as well as on the angle  $\theta$  between the incident ray from the star and the viewing direction, Figure 5.2. The dust density can be so high that an illuminating photon is likely to be scattered several times within the voxel before exiting, multiple scattering must be taken into account when computing  $P(\tau(v), \theta)$ . We use Monte-Carlo simulation to pre-compute and tabulate scattering probabilities  $P(\tau(v), \theta)$  for 1000 scattering depth values between  $\tau(v) = 0$  and 10, each for 72 directions between  $\cos \theta = -1$  and  $+1$ . Appendix A gives details of the Monte-Carlo simulation. The table is computed for the albedo and anisotropy values  $\alpha = 0.6$ ,  $g = 0.6$  of interstellar dust, as suggested by the astrophysics literature [[Gordon 2004a](#)].

Figure 5.3 depicts the direction-dependent scattering probability distribution of a voxel for different scattering depths  $\tau(v)$ . Due to multiple scattering, directional dependence changes much with voxel scattering depth. With increasing dust concentration, the total amount of scattered light first increases, then starts to decrease for very dense dust. Regions of thin to moderate dust are dominated by forward scattering, while very dense dust regions exhibit mostly backward scattering.

## 5.6 Nebula Generation

The visualization tool proposed by us can render any given 3D dust distributions. For planetarium shows or educational purposes, a given reflection nebula can be generated based on artistic and esthetic criteria. For an astrophysical application, the dust distribution has to exactly match measured brightness distribution of real nebula.

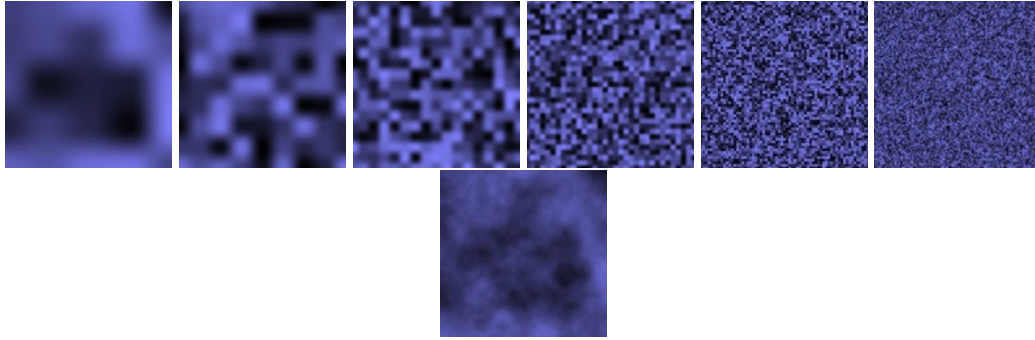


Figure 5.4: The top row shows smooth 2D noise functions at different frequencies and amplitudes. The image in the bottom row is the resulting 2D Perlin noise image which is a combination of the top row images. Images courtesy of Hugo Elias [[Elias 2007](#)]

Based on astrophysics literature, we can assume that stellar winds from the illuminating star have swept clean the immediate surroundings, so that the star is situated in a sphere of low dust concentration. Beyond this sphere dust concentration increases, forming inhomogeneous dust clouds. To reproduce corresponding variations in local dust density, we use a constrained 3D Perlin noise function [[Perlin 1985](#)] to modulate voxel scattering depth  $\tau(v)$ . As shown in Figure 5.4, a 2D Perlin noise image is generated by combining noise functions with different frequencies and amplitudes. We can generate a wide variety of different-looking, yet realistically appearing nebulae by varying Perlin noise amplitude and frequency, Figure 5.5.



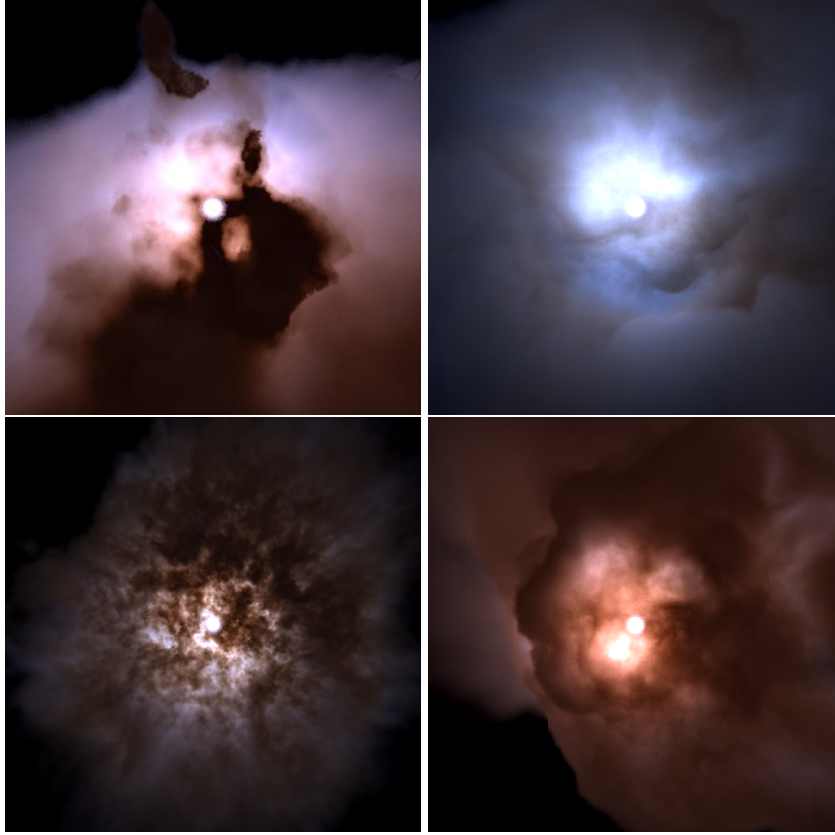


Figure 5.5: Renditions of different 3D dust distributions generated with various setting for the constrained 3D Perlin noise generator

## 5.7 Interactive Rendering

Before visualization, the pre-computed scattering table is uploaded as a 2D floating-point texture to graphics memory. A floating-point 3D texture stores the scattering depth  $\tau(v)$  for each voxel. Depending on the number of illuminating stars, one or more 3D arrays store the pre-computed illumination  $L_{incoming}$  for each voxel. We also store the emissive radiance  $L_{em}$  per voxel. The 3D emission texture allows us to visualize the illuminating star. Both emitted and scattered light undergo the same extinction on the way from the voxel to the camera  $L(x, y)$ , (5.2).

Our reflection nebula visualization algorithm is based on GPU-based ray-casting. After determining viewing ray parameters as described in [Krueger and Westermann 2003], we use a fragment program to step along each viewing vector from front to back in voxel-length intervals. At each step, we look up local scattering depth  $\tau(v)$ , voxel illumination  $L_{incoming}$ , and emissive RGB radiance values  $L_{em}$



from the 3D volume textures, taking advantage of hardware-accelerated trilinear interpolation. The fragment program computes the angle between viewing ray direction and the incident star-light direction  $\theta$ , and queries the scattering probability table to determine  $P(\tau(v), \theta)$ . Equation 5.3 is evaluated, and the emissive radiance  $L_{\text{em}}$  is added.

To quickly evaluate equation 5.2, we accumulate extinction depth  $\tau$  while stepping along the ray. For each ray, extinction depth  $\tau(v)$  is initialized to zero. At each step  $i$  along the viewing ray, local extinction is added up,  $\tau^{i+1} = \tau^i + \tau(v)^{i+1}/\alpha$ . Equations 5.3 and 5.2 are actually computed for the red, green, and blue channel separately by weighting  $\tau(v)$  according to Section 5.3. For display, the rendered image is optionally normalized and gamma-corrected.

The change in appearance due to different viewing directions can be evaluated by simply rotating the nebula. However, to appreciate the full range of color variations, e.g., for planetarium shows, we want to be able to move the viewpoint inside the nebula. We appropriately modify the original GPU-based ray-casting algorithm [Krueger and Westermann 2003, Scharsach 2005] to solve the problem that arises when the near clipping planes fall within the volume.



Figure 5.6: Left: Photo (color composite) of the “Cocoon” reflection nebula IC 5146 (from, Greg Crinklaw [Crinklaw 2005]). Right: rendering result for a simulated dust distribution with 4 illuminating stars, composited into a star field photo for enhanced visual realism

## 5.8 Results

Our visualization tool is designed to render realistic images of reflection nebulae. A comparison of a photo composite of an actual nebula (IC 5146) and the visualization of a simulated dust distribution is presented in Figure 5.6. Note how our rendering algorithm produces color hues very similar to reality, and how the synthetically generated dust distribution reproduces closely the overall appearance of the real nebula. Figure 5.7 presents screenshots from a fly-around and a fly-through sequence for two synthetic nebulae to illustrate the change in shape and color with viewpoint. From the outside, the nebula appears reddish with dark regions of dense dust. Once inside the nebula, backscattered light is responsible for the blue-enhanced appearance. Depending on dust concentration and geometric dust configuration, the scattered star light reaches the viewpoint almost unhindered (bluish appearance), attenuated to varying degrees (reddish appearance), or not at all (dark regions).

In the presence of one illuminating star and with our rendering algorithm performs at 7.5 frames per second on an nVidia GeForce 6800 Ultra graphics board, rendering at  $512 \times 512$ -pixel resolution from a  $128^3$ -voxel model. Alternatively, for 2,3,4 or 5 illuminating stars, rendering frame rates are 4.7, 3.6, 2.5, and 1.9 Hz, respectively.

## 5.9 Conclusions

We have presented an interactive visualization tool to realistically render reflection nebula appearance based on astrophysical models. The algorithm runs on graphics hardware and allows the user to interactively vary viewing position and direction. Multiple scattering is taken into account locally, at voxel level. Our visualization tool can be used to create virtual fly-throughs of reflection nebulae for interactive desktop visualizations, or to produce scientifically accurate animations for educational purposes such as planetarium shows.

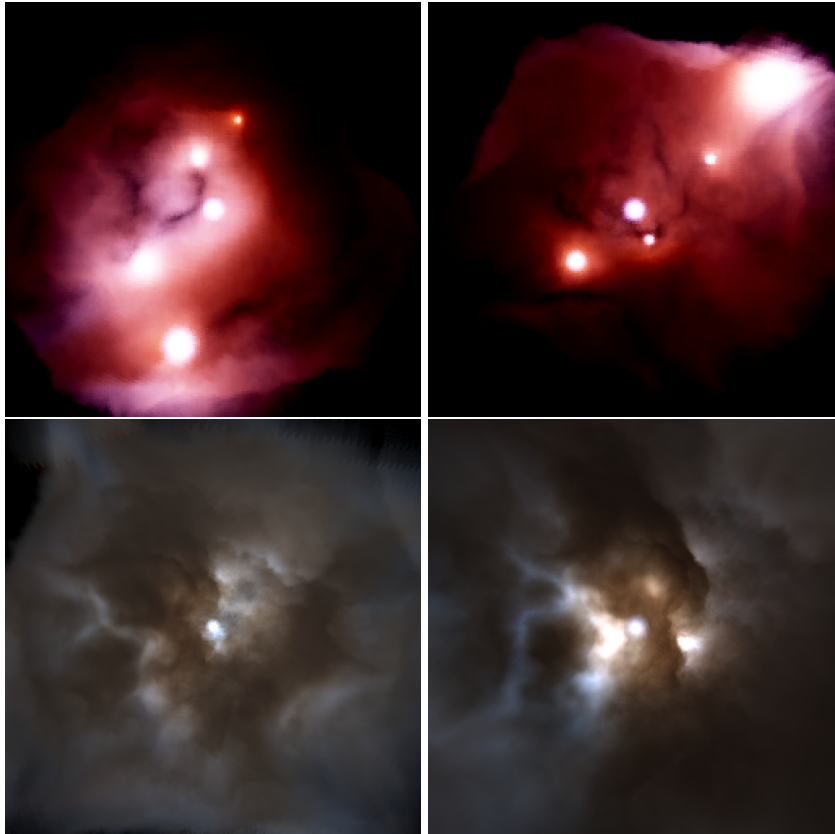


Figure 5.7: Screenshots from a fly-around sequence of a nebula illuminated by five stars (top), and images of a fly-through sequence with a single central star (bottom). Top: From the outside, nebulae appear reddish due to wavelength-dependent extinction. Bottom: Once inside the nebula, thin dust backscatters predominantly blue light, while light backscattered from dense dust assumes the color of the illuminating star



## **Part III**

# **Reconstruction of Astronomical Objects**



# Overview

This part of the thesis deals with the reconstruction of two types of astronomical objects: reflection and planetary nebulae. We consider for single scattering and absorption in the proposed light transport models. The methods presented in both chapters use Powell's non linear direction set optimization method to recover the 3D distribution of the objects. Chapter 6 describes the method we propose to recover 3D dust densities in reflection nebulae from a single input image. While being an ill posed problem, we succeed to recover plausible reflection nebula distributions by modelling the light transport in this type of astronomical objects and carefully guiding the optimization process.

Chapter 7 presents our method to reconstruct both gas and dust distributions in planetary nebulae starting from images at two wavelength. Because the physical characteristics of the dust and gas constituting the nebula vary when imaged at different wavelengths, we are able to reconstruct the 3D distribution of gas, as well as dust. In the case of planetary nebulae we use the axial symmetry property which is inherent for a large number of objects of this type. This allows us to reduce the complexity of the reconstruction problem and obtain more plausible reconstruction results.





---

# Chapter 6

## Reflection Nebula Reconstruction

In this chapter we present a method for reconstructing the 3D distribution of dust densities in reflection nebulae based on a single input image using an analysis-by-synthesis approach. While the core problem of reconstructing an arbitrary 3D volume of dust particles from a 2D image would be ill-posed we demonstrate how the special configuration of light transport paths in reflection nebulae allows us to produce non-exact but plausible 3D volumes. Our reconstruction is driven by an iterative non-linear optimization method, which renders an image in each step with the current estimate of dust densities and then updates the density values to minimize the error to the input image. The recovered volumetric datasets can be used in astrophysical research as well as planetarium visualizations.

### 6.1 Introduction

In this chapter, we address the problem of reconstructing a plausible 3D volume of a reflection nebula using only a single image as input, which can be captured by any telescope. We assume that all light reflected by the nebula originates from a single central star, and that the reflected intensity is due to single scattering and due to the absorption along the path. Scattering and absorption is correlated to the dust volume density which we aim to reconstruct. Besides the simplified light transport model we do not pose any further restrictions on the nebula, most importantly we do not assume any kind of symmetry as has been formulated in

previous reconstruction approaches from single images [Magnor et al. 2004, Linfu et al. 2007b].

Of course, the reconstruction of 3D volumes from 2D images is an under-determined problem. We generate plausible reconstructions by making use of two insights: the intensity of each observed pixel is actually the combined effect of the volume densities along the entire light path from the central star towards the viewer. Each voxel of the volume we are reconstructing therefore has a non-local effect on the final image. This implicitly regularizes the possible solution to some extent. A second result of the specific light transport is that the estimated density for voxels close to the central star have a significant impact on the appearance of a large number of pixels while the area of influence decreases drastically with distance. We account for this effect by optimizing the volume densities in concentric shells, starting with the innermost sphere.

The optimization is driven by an analysis-by-synthesis approach. We make use of a hardware-accelerated volume renderer to determine the appearance given the current estimate of the dust densities. The error to the input image is then minimized based on Powell’s algorithm [Press et al. 1992]. While we do not claim to correctly reconstruct the original nebula’s 3D volume we at least reconstruct a plausible dust distribution that matches the input image. Compared to an initial naive traversal of the volume during optimization, we obtain a better match to the given image and a more plausible 3D volume by following an improved traversal during optimization. Plausible reconstructions can be used for visualization purposes or as starting point for further, more complex physical simulations that incorporate additional measurements. The main contribution of this work is that we recover a physically plausible 3D volume of an astronomical nebula from a single input image. The obtained datasets can be used as starting approximations by astrophysicists working with 3D models of reflection nebulae as well as for educational purposes in modern day planetarium shows.

## 6.2 3D Reconstruction

In the previous Chapter 5, we described a framework for physically correct rendering of reflection nebulae. In this chapter we propose a method to recover the 3D dust densities in reflection nebulae based on a single input image.

As lighting model, we use the same model which was described in Section 5.4. The dust density is the quantity we actually attempt to reconstruct, and our goal is to determine  $\tau(\nu)$  up to a scale factor.

Our analysis-by-synthesis approach is driven by the non-linear Powell optimization algorithm, Section 2.4. During optimization, we render the current dust density distribution using the equations described in Section 5.4 and the rendering framework in Section 6.2.1 and, at every step, we compare the rendering with the given input reflection nebula image.

Before starting the reconstruction process, the input images are cropped to a square and converted to gray-scale. One has to make sure that the central star is placed in the center of the image. Since we do not consider self-emission foreground stars are masked out in order to avoid interference with the reconstruction.

The reconstruction process is based on minimizing the following error functional

$$Err = \sum_{x,y=1}^n ||L(x,y) - L_{inp}(x,y)||^2 \quad (6.1)$$

which is computed using the currently rendered  $L(x,y)$  (Equation 5.2) and the input image  $L_{inp}$ .

As can be seen in Figure 5.2 each voxel has a non-local effect on the rendered image, resulting in some implicit regularization of the optimization. However, this is not constraining the under-determined problem entirely. In the Powell algorithm each voxel is optimized independently. During optimization, the order in which the voxels are processed is very important for the speed and quality of the reconstruction. A naive traversal in a loop over the  $x$ ,  $y$  and  $z$  coordinates yields poor reconstruction results, as demonstrated in Figure 6.1.

The reconstruction artifacts are due to the fact that the radiance reflected by voxels at the outer rim of the volume depends on the dust density values of the inner voxels. During optimization, changes to the inner voxels require updates of the outer voxels which can only be performed after the entire volume has been optimized in one iteration step.

We obtain much better results (Figure 6.3) when the traversal is done starting from the center to the outside. Voxels closest to the central star are traversed first, resulting in a set of concentric spheres with center at the point of the central star (see Figure 6.2).

Another observation is that it is better not to start the reconstruction process with an empty volume. It is filled homogeneously with dust densities as small as the smallest  $\Delta\rho$  with which we increment or decrement the voxel dust densities during optimization.

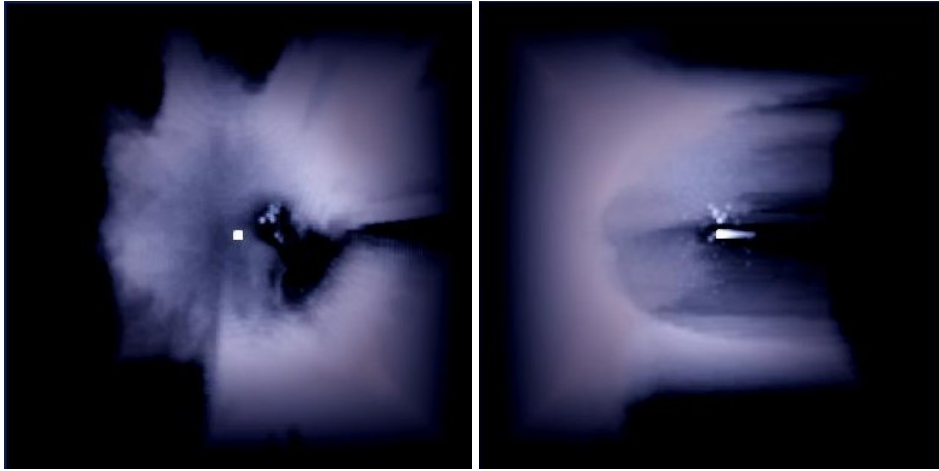


Figure 6.1: Inadequate optimization results of NGC 1999 by processing all voxels in scan-line order. Note the decreasing reconstruction quality with increasing distance to the central star. In the side-view (right), an unnatural distribution along the  $z$ -axis is visible: the dust is concentrated in the region furthest away from the observer.

### 6.2.1 Rendering and Runtime Optimization

As the lighting calculations are the most computationally expensive, we can obtain a great speedup by accelerating them. We have developed two different options:

To render full frames, and to visualize the results of the reconstruction, we use an OpenGL-based renderer very similar to that used in section 5.7 for reflection nebula visualization. It is a volume rendering application based on a real time ray-caster implemented on graphics hardware. The implemented algorithm uses the idea described by Krüger et al. [[Krüger and Westermann 2003](#)] to color code the direction of the viewing rays using a bounding box. The algorithm exploits the capabilities of modern graphics hardware to step along the lines of sight querying 3D textures, using a fragment shader to accumulate the in-scattering along each ray while considering absorption.

While the hardware-based renderer is significantly faster than a software renderer for computing a full frame, we observe that during the optimization of individual voxels only fractions of the images are actually affected. During optimization, while constantly changing the density of one voxel at a time, only those pixels in the rendered image have to be recomputed which are affected by the new voxel value. The footprint of each voxel is precomputed since it only depends on the ray geometry and is independent on the actual volume density.

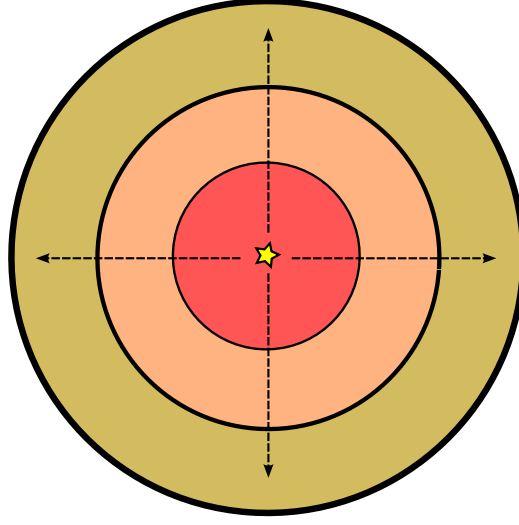


Figure 6.2: During optimization the volume is traversed starting from the center, in concentric shells.

A further speed-up as well as an additional means to avoid local minima during the optimization process is achieved by an iterative multi-resolution approach. The reconstruction starts with a lower resolution volume which is scaled up after the end of every iteration. This is done by subdividing each voxel into eight sub-voxels with the same dust density value and applying a 3D Gaussian filter on the dataset for smoothing the resulting high frequencies. We measure a speed-up of factor 2 in the final reconstruction compared to optimizing performed directly at the highest resolution.

## 6.3 Results

We present the results of our proposed reconstruction approach for several reflection nebulae: NGC 1999 (Figure 6.3), the Iris Nebula (Figure 6.4, top row) and the Cocoon Nebula (Figure 6.4, bottom row). As already mentioned in section 6.2, the reconstruction is performed for a single wavelength only, speeding up the computation. The here presented results were rendered using spectrally dependent absorption and scattering coefficients. Since our lighting model does not include self-emission we manually removed all stars in the input images since they cannot be recovered. To produce slightly more realistic final renderings we sometimes added artificial star fields approximating the original image.

For all nebulae we presented the original image the reconstructed volume rendered

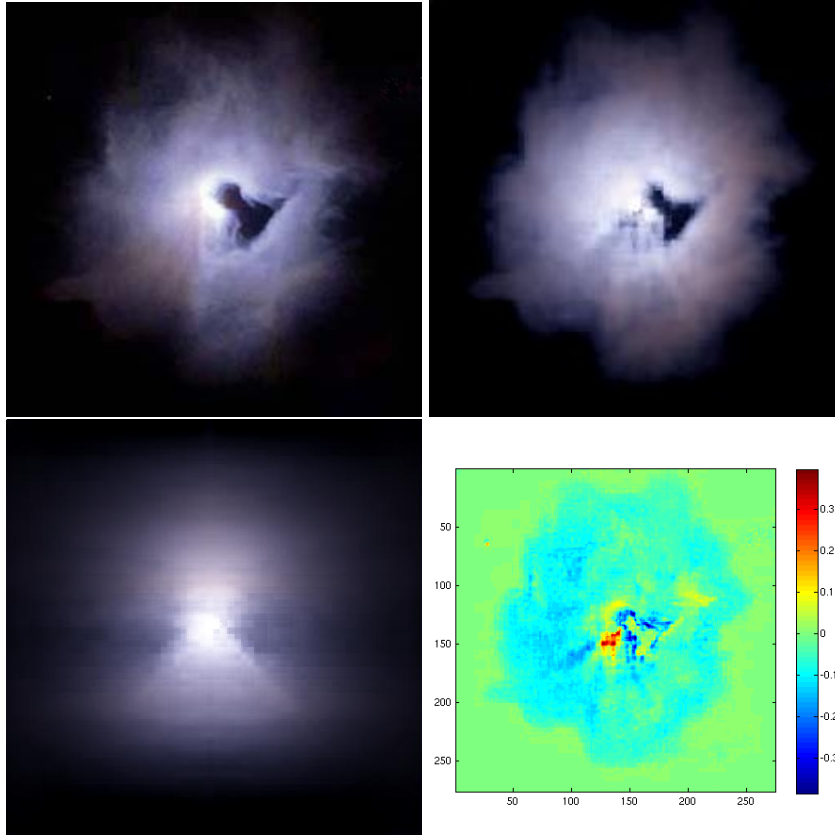


Figure 6.3: Results for the NGC 1999 nebula. The top row shows the input image (left) and the rendering of the reconstruction from the same viewpoint (right). The bottom row shows a side view of the recovered dust density (left). A color coded difference image between the input image and the rendering of the recovered dust density is presented in the bottom right corner, indicating the good quality of the reconstruction.

from the same view as well as a rendering of the volume rotated by 90 degrees around the vertical axis. In the frontal views, one can see that the large-scale features are very well reproduced. Some detail has been lost though because the reconstruction has been performed at a maximum resolution of  $64^3$  voxels. In the bottom right corner of Figure 6.3 we further present an image of the relative differences between the captured and the reconstructed image, which are overall relatively small.

In the frontal view, the largest error is observed close to the central star. This is because of the lack of self emission in our framework and can be explained by the algorithm trying to compensate the high intensity values in the center of the input



Figure 6.4: From left to right: input image, reconstructed frontal and rendered side view. The top row shows the reconstruction for the Iris Nebula and in the bottom row we present renderings of the Cocoon Nebula. Note, how the structures of the input image are well reproduced in the frontal view. The side views indicated that plausible volumes have been reconstructed.

image (where the central star is situated) with a dust density generating high pixel intensity values.

Looking at the side views, one sees a reconstruction that radiometrically agrees with the provided input data, and thus is physically plausible. However, the reconstructed distribution along the  $z$ -axis might not necessarily match the expected statistical distribution. It looks slightly too smooth compared to the frontal view. However, it still resembles a reasonable nebula. The best reconstruction is achieved for the Cocoon Nebula (Figure 6.4, bottom row). We attribute this effect to the slightly less inhomogeneous distribution in the input image.

The most prominent artifacts of our reconstruction are possibly the diagonal features visible in all three side views. While we are not exactly sure, this might be caused by the way how the aggregated extinction  $\tau(\nu)$  and albedo  $\alpha$  are pre-computed for a single voxel and for every density. During evaluation the voxel is assumed to be perfectly isotropic which of course contradicts the anisotropic shape of a cube, with the largest deviation exactly along the diagonal.

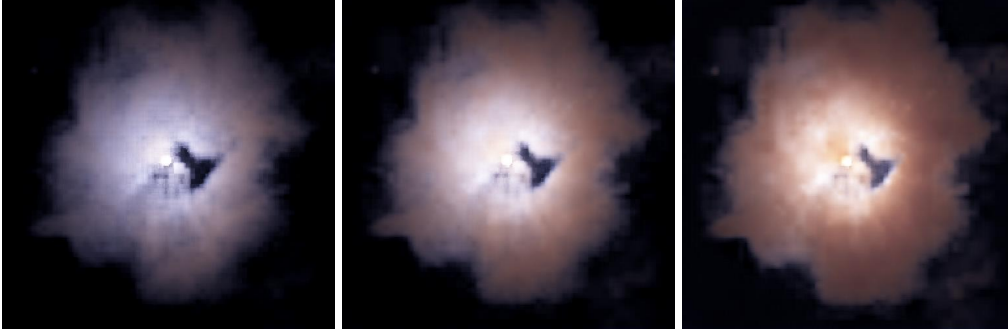


Figure 6.5: Reconstruction results for different intensity values of the central star, decreasing from left to right. A smaller luminance level leads to higher dust density values and to reddening of the nebula.

In Figure 6.5, we demonstrate the dependence of the reconstruction results on the intensity of the central stars. We reconstructed the same input image of the nebula NGC 1999 with three different values for  $L_e^{star}$ . In order to reproduce the same input pixel intensity, a fainter central star leads to higher dust density values. Conversely, a brighter central star leads to smaller dust density values. With the increasing dust density the different reconstructions also show an increased reddening as explained in Section 5.2. This effect could actually be used to optimize for the intensity of the central star as well, if wavelength dependent effects are considered during the optimization.

## 6.4 Conclusion

We presented a reconstruction method for physically plausible volumetric models of reflection nebulae given only single input images. We do not pose any geometric constraints on the shape of the nebulae, such as symmetry which has been applied in previous reconstruction methods. Using an analysis-by-synthesis approach we perform a non-linear optimization to recover the dust density values. The recovered datasets can later be visualized using a custom renderer and can also be used as starting point for planetarium shows or further physical simulations. While we so far concentrated on the reconstruction of reflection nebulae, it would be interesting to apply our reconstruction algorithm to other volumetric phenomena that feature single scattering and absorption.

One meaningful extension of our method would be to incorporate multi-wavelength input images; the renderings of the recovered dust density would have to match



multiple input images taken with different band filters. Besides the ability of estimating the exact brightness of the central star as indicated in the previous section one might be able to obtain a more precise volumetric reconstruction since additional independent constraints are given.

Another promising future research direction would be to add further constraints to the optimization in order to force the statistical distribution of densities along the z-axis to match the statistics of the input image. One could apply for example histogram matching or similar techniques which recently has been successfully applied in the context of solid texture synthesis [[Kopf et al. 2007](#)]. Adding such an additional constraint should be rather easy in our current optimization framework.



---

---

## Chapter 7

# 3D Reconstruction of Gas and Dust in Planetary Nebulae

This chapter addresses the problem of reconstructing the 3D structure of planetary nebulae from 2D observations. Assuming axial symmetry, our method jointly reconstructs the distribution of dust and ionized gas in the nebulae from observations at two different wavelengths. In an inverse rendering framework we optimize for the emission and absorption densities which are correlated to the gas and dust distribution present in the nebulae. First, the density distribution of the dust component is estimated based on an infrared image, which traces only the dust distribution due to its intrinsic temperature. In a second step, we optimize for the gas distribution by comparing the rendering of the nebula to the visible wavelength image. During this step, besides the emission of the ionized gas, we further include the effect of absorption and scattering due to the already estimated dust distribution. Using the same approach, we can as well start with a radio image from which the gas distribution is derived without absorption, then deriving the dust distribution from the visible wavelength image considering absorption and scattering. The intermediate steps and the final reconstruction results are visualized at real-time frame rates using a volume renderer. Using our method we recover both gas and dust density distributions present in the nebula by exploiting the distinct absorption or emission parameters at different wavelengths.

## 7.1 Introduction

All astronomical nebulae are seen by an observer on Earth from a single perspective. Physics can help us infer the spatial distribution of some of these objects, but a quantitative understanding of their shape can only be gained by reconstructing their 3D structure and visualizing the derived models. Recently, there is an increased interest in the graphics community in the field of astronomical simulations and visualizations. Recent works range from physically correct animations of nebulae for planetarium shows [Nadeau et al. 2001], to a specifically designed ray-casting application for visualizing large scale datasets such as galaxy or star formation [Kähler et al. 2006].

In this chapter, we present an approach to reconstruct and visualize 3D volumes of planetary nebulae. In tomography, reconstruction is typically based on several 2D projections of the object to be reconstructed, observed from different directions. Provided there are enough 2D projections of the object of interest, the volume can be reconstructed using filtered back-projection, algebraic reconstruction [Gordon et al. 1970] or other available techniques [Sharpe et al. 2002, Trifonov et al. 2006]. There are, however, some cases where there is only one available 2D projection of the volume, e.g., when the observed phenomenon occurs only once. In our case, the nebulae are so distant from the observer that only one projection is available. In order to obtain a plausible reconstruction of the object's real 3D distribution, additional constraints are necessary. In this chapter we constrain the solution in two ways: axis-symmetry and optical consistency at different wavelengths. This axis-symmetry is found naturally in many planetary nebulae (See Figure 7.2 for example) [Magnor et al. 2004].

Based on the symmetry constraint we present a method for reconstructing the 3D axis-symmetric distribution of an emissive volume containing participating media, and apply our technique to recover the structure of *planetary nebulae*.

Our approach is based on the algorithm presented previously by Magnor et al. [Magnor et al. 2004], who reconstructed only 3D emissive volumes for planetary nebulae. The authors assume that absorption and scattering is negligible. As pointed out in [Kwok 2000, Lee and Kwok 2005] there are, however, quite significant quantities of dust present in planetary nebulae and their effect needs to be considered. Therefore, we recover the 3D distribution of ionized gas *and* dust by extending the reconstruction algorithm in such a way that it also correctly accounts for absorption and scattering due to dust.

Since we need to optimize for two different distributions at the same time, a single input image is not sufficient. Our key contribution is to make use of the fact that

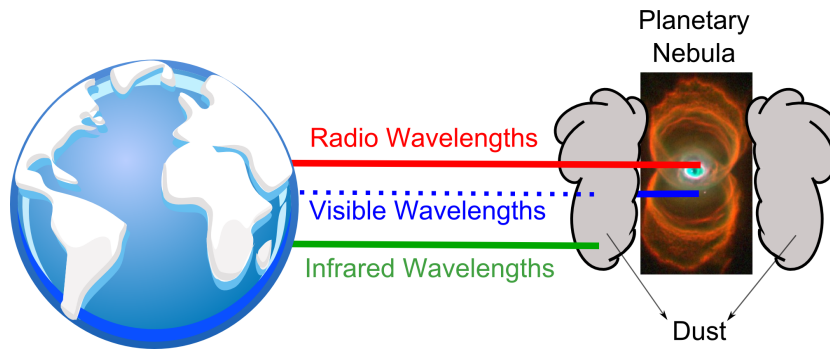


Figure 7.1: Light in the *visible* wavelengths is partially absorbed and scattered by dust present in the nebula. *Radio* wavelengths are not affected by any dust between the object and an observer on Earth. At certain *infrared* wavelengths, we can observe only the dust distribution in the nebula due to its blackbody radiation.

the extinction coefficient of the dust particles is wavelength dependent. As input data we use two images recorded at different wavelengths, one radio image and one image in the visible spectrum, or similarly by using an infrared and a visible wavelength pair of images (See Figure 7.1). From physics follows that the radio image is almost unaffected by the dust present in the nebula. It can thus be used to estimate the emissive volume, i.e., the concentration of the ionized gas. From the recovered distribution one can then compute analytically how much light the nebulae would emit at visible wavelengths if no dust were present. Lee et al. [Lee and Kwok 2005] describe a simple way to compute the expected  $H\alpha$  (emission line of ionized hydrogen) flux. By comparing this undisturbed estimate with the second recorded image at visible wavelengths, the dust distribution is derived. In a similar way, a pair of infrared and visible spectrum images can be used as input for our reconstruction algorithm, because infrared images trace mostly the dust distribution through its intrinsic temperature.

To visualize the reconstructed 3D volumes and the combined effect of ionized gas and dust we extend the real-time volume rendering approach for reflection nebulae described in [Magnor et al. 2005]. Our visualization algorithm now considers *emission*, *scattering* and *absorption*, all at the same time.

The reconstructed volumes can be used by astronomers for visualizing and analyzing the 3D distribution of gas and dust in axis-symmetric nebulae, or for educational purposes in planetarium shows intended for the general public.

## 7.2 Planetary Nebulae

In this section we will briefly describe the physics behind planetary nebulae and discuss the effects of dust present in these astronomical objects. These nebulae form when a star of up to 5 times the mass of our Sun reaches the end of its life span. When the star runs out of hydrogen fuel for the nuclear reactions, its inner pressure decreases, causing it to collapse under its own gravity and to start heating up.

As the temperature around the central star is rising, ultraviolet photons are emitted which ionize the previously ejected gas surrounding the stellar core. Depending on the chemical elements present in the nebula, the emitted photons by the ionized gas have different energy levels, and thus generate light of different characteristic wavelengths. The emission in every such narrow band traces back the distribution of the corresponding chemical elements in the nebula. More in-depth information about the astrophysics of planetary nebulae can be found in [Kwok 2000, Osterbrock 1974]. For a review on planetary nebula formation refer to [Balick and Frank 2002].

A large number of these objects also show a distinct axial-symmetrical structure, Figure 7.2. This can be explained by the way some of these objects are created, which is mainly a strong jet of outflow of gas and dust in two opposite directions from the central star.

The electromagnetic radiation emitted by planetary nebulae, as presented in Figure 7.1, is affected differently depending on the wavelength the observations are conducted. At *visible* wavelengths, the dust present in the nebula absorbs and scatters the light reaching an observer on Earth. Whereas based on observations at *radio* wavelengths, the distribution of the ionized gas without the effects of scattering or absorption can be directly determined; we use this property in our reconstruction process, which is described in detail in Section 7.3.2. At *infrared* wavelengths (based on the laws of blackbody radiation), predominantly the dust particles present in the nebula emit electro-magnetic radiation caused by their intrinsic temperature. We use this property in our reconstruction process, which is described in detail in Section 7.3.2.

### 7.2.1 Absorption and Scattering

At visible wavelengths the dust particles in planetary nebulae affect the light reaching an observer on Earth by absorption and scattering. Even though the ionized gas in planetary nebulae emits light itself, the central star's emission is much

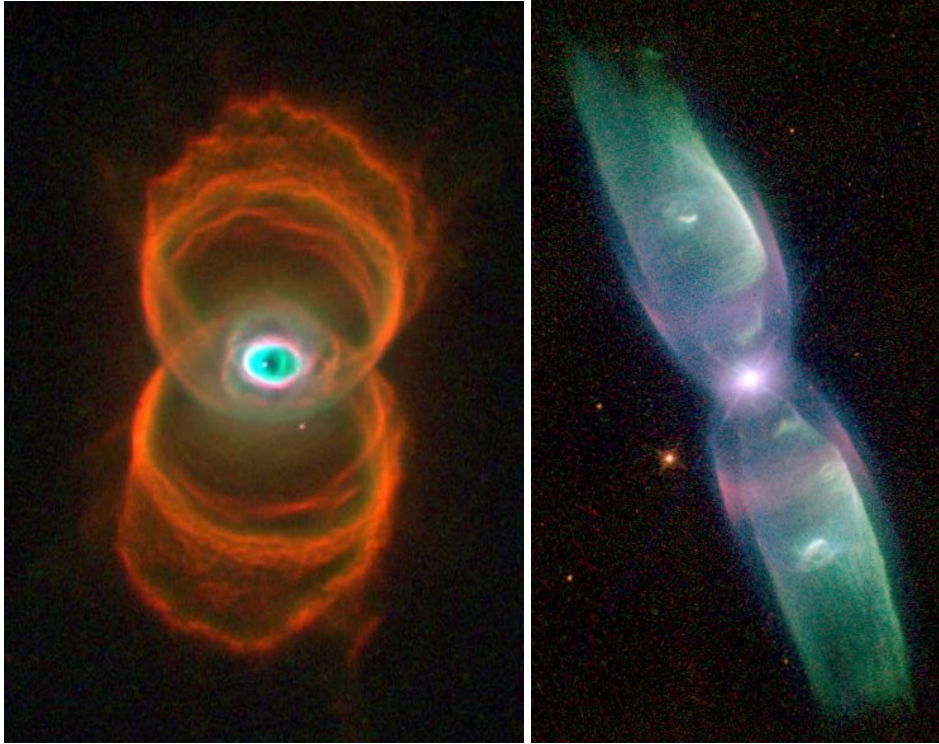


Figure 7.2: Hubble Space Telescope Images of the Hourglass Nebula (left, courtesy of Sahai and Trauger (JPL), NASA) and the Butterfly Nebula (right, courtesy of Balick (University of Washington) et al., NASA). Both nebulae highlight significant axial symmetry. The Hourglass Nebula has a smaller inclination angle. Its symmetry axis is tilted towards the viewer while for the Butterfly Nebular the axis is almost parallel to the image plane.

brighter. Therefore, we consider the central star as being the only light source for the purpose of computing the amount of light scattered in the direction of the observer. The effect of absorption is given by the high amount of dust situated generally in the equatorial region of these objects, surrounding the central star, as well as the dust which is mixed with the ionized gas.

We create a physically-based model of light scattering in interstellar dust using two scalar parameters. First, there is *albedo*, which indicates how much light the particles reflect: 0 for total absorption, i.e., black dust, and 1 for the case when all incident light is scattered. The second parameter is the *single particle scattering probability* modeled using the Henyey-Greenstein phase function [Henyey and Greenstein 1941]. In addition, the presence of dust also attenuates any light shining through the dust region, which is described by the *extinction* parameter.

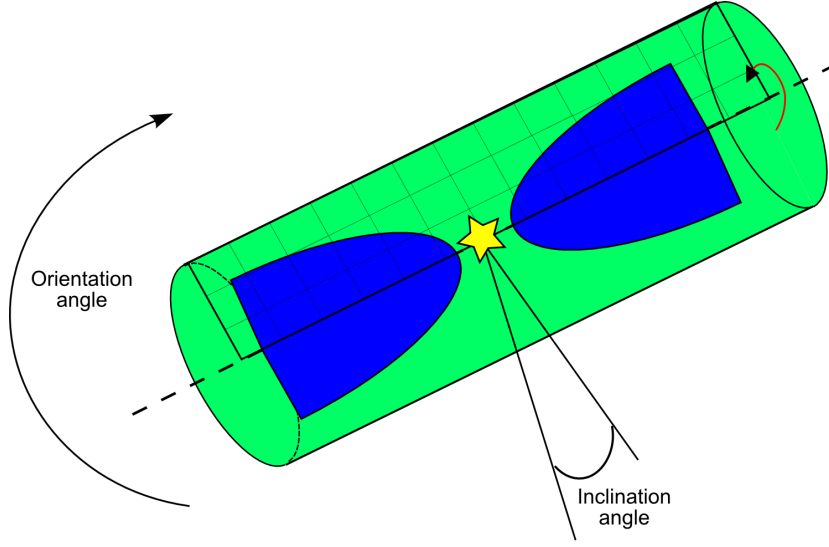


Figure 7.3: The axis-symmetric model of a planetary nebula. The *orientation angle* determines the rotation of the nebula's axis of symmetry in the plane perpendicular to the viewing direction. The *inclination angle* measures the tilt of the axis in relation to the viewing direction. A 3D volume of a nebula can be generated by rotating a 2D map around its axis of symmetry.

Absorption is taken into account for light emitted by the ionized gas as well as the scattered light of the central star.

### 7.3 3D Reconstruction

Our optimization is based on the following rendering model, very similar to the one used in the previous Chapter, in Section 5.4. In the case of planetary nebulae, we only add the self emission of each voxel. The observed radiance  $L(x, y)$  at a camera at position  $c$  is a function of the gas emission  $L_e(v)$ , extinction  $\tau(v)$ , and the albedo  $\alpha$  of every voxel  $v$  along the ray through the camera pixel:

$$L(x, y) = \int_c^\infty e^{-\int_c^v \tau(w) dw} \cdot (L_e(v) + \alpha \cdot S(v)) dv, \quad (7.1)$$

where  $S(v)$  is the total in-scattering to the voxel  $v$  towards the camera due to the emission  $L_e^{star}$  of the nebula's central star(s) at position  $p^{star}$ . Considering single scattering only,  $S(v)$  is computed as

$$S(v) = P(\tau(v), \theta) L_e^{star} \cdot e^{-\int_{p^{star}}^v \tau(w) dw} \quad (7.2)$$



incorporating the extinction on the way from the star to the voxel as well as the Henyey-Greenstein scattering phase function  $P$  from the star to the voxel into the direction of the camera  $c$ .  $L_e^{star}$ , and  $p^{star}$  are assumed to be known. For many nebulae they can be looked up in the astrophysical literature.

The extinction  $\tau(v)$  is directly proportional to the dust density  $d_{dust}(v)$ , while  $L_e(v)$  is linearly related to the concentration of ionized gas  $d_{gas}(v)$ . The exact factors can be found in physics textbooks. The goal is to determine  $d_{dust}(v)$  and  $d_{gas}(v)$  up to scale.

Reconstructing a 3D volume based solely on a single 2D view is generally an ill-posed problem. Using the axial symmetry constraint we can simplify the problem of reconstructing a 3D volume to that of reconstructing a 2D map. This reduces the complexity of the reconstruction problem and speeds up the optimization process. At each step in the reconstruction, a 3D volume is obtained from the 2D maps by rotating the maps around the symmetry axis, see Figure 7.3. During the description of the algorithm, to better distinguish between reference images and the reconstructed 2D slices, we will refer to 2D recordings of real nebulae as *images*, and to the reconstructed 2D axis-symmetric distributions as *maps*.

### 7.3.1 Optimization

To drive our optimization we use the standard implementation of Powell's non-linear optimization method, Section 2.4. At every step, the sum of squared differences between the rendered and the reference image is evaluated. The algorithm minimizes this error functional by updating individual pixels in the maps and stops when it drops below a given threshold. We always initialize the maps to be zero. Besides the values in the 2D map, the algorithm also optimizes the inclination and orientation angles of the nebula (Figure 7.3). An initial estimate for the orientation angle is computed based on the input images by calculating the principal eigenvectors of the image's covariance matrix. The initial inclination angle is set to  $90^\circ$ , i.e. symmetry axis is parallel to the image plane.

Since each iteration step in the optimization requires the computation of a volume rendered image we exploit graphics hardware for acceleration. The rendering algorithm used is described in more detail in Section 7.4. We evaluate Equation 7.1 in each iteration step for the entire image, or use simplified versions (Equation 7.4 or Equation 7.5 in the particular cases below), and finally compute the difference to the reference image on a graphics card. The rest of the optimization is still controlled by the CPU though.

For a more efficient and more stable optimization we perform the optimization

hierarchically, start by optimizing a low resolution map, successively increasing the resolution until it slightly exceeds the resolution of the input images.

### 7.3.2 Planetary Nebula Reconstruction

In order to reconstruct both *gas* and *dust* distributions, our algorithm needs as input two different images for each nebula. As a general prerequisite, these images have to be affected differently by the optical characteristics of the gas and dust elements present in the nebula.

#### Reconstruction Based on Radio and Visible Datasets

In this approach we use a pair of radio and visible wavelength images. The first input image (denoted as  $U$ ) is a radio continuum image from which we derive the gas distribution  $d_{gas}$ . The radio data is not affected by the dust distribution at all. The radio intensity  $U$  is related to the expected visible emission  $U'$  of the gas by the following equation [Lee and Kwok 2005]

$$U' = 6.85 \cdot 10^{-10} \cdot \nu \cdot U \quad (7.3)$$

where  $\nu$  is the frequency of the radio observation in  $GHz$  and  $U$  is measured in  $Jy$ . We compute  $U'$  which would correspond to an image of the nebula at the wavelength of  $H\alpha$  emission of the ionized gas as if no dust were present (Figure 7.5, left). The second input image, denoted  $A$  (Figure 7.6, left), is a captured image at this particular narrow band of visible wavelength corresponding to the same emissive  $H\alpha$  gas elements which in fact is affected by scattering and absorption due to the dust.

*Gas distribution estimation.*

In the first step, the *emission density map* corresponding to the ionized gas distribution  $d_{gas}(\nu)$  is reconstructed using  $U'$  as reference image. The rendering model simplifies to

$$L(x, y) = \int_c^\infty L_e(\nu) d\nu \quad (7.4)$$

because this observation is almost unaffected by the dust, so no absorption or scattering needs to be considered. The gas distribution map is estimated using the iterative non-linear optimization algorithm (Section 7.3.1). Given a current estimate of the gas density map  $d_{gas}$ , the emission  $L_e(\nu)$  is computed and an image is rendered according to Equation 7.4. The optimization drives the difference

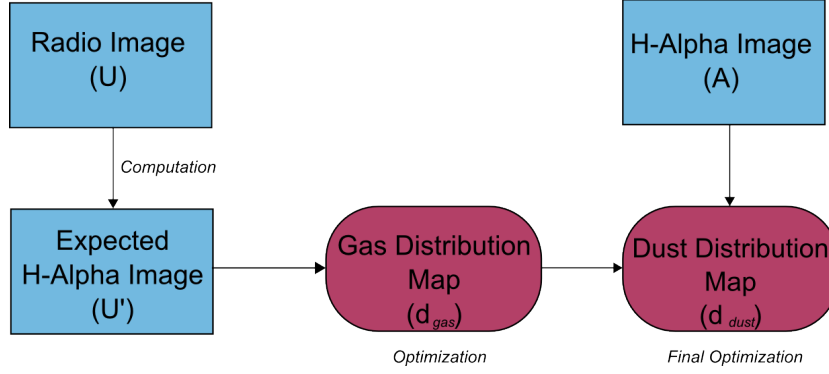


Figure 7.4: Flowchart of the reconstruction process using radio and visible wavelength data. First, the radio input image is converted to simulate a visible wavelength image  $U'$  of the emissive gas without any absorption or scattering. From  $U'$  we derive  $d_{gas}$ . Using the visible wavelength image  $A$  which capture the combined effects of the gas emission and the scattering and absorption of the dust, we obtain  $d_{dust}$ .

between this estimated image and the reference image  $U'$  to a minimum. We initialize the optimization with a homogeneous distribution. Figure 7.5 shows the reference image  $U'$ , the recovered gas density map  $d_{gas}$  and the rendering of the reconstructed volume. The reconstruction resembles the input up to the non-symmetries in the input.

#### *Dust distribution estimation.*

Using the gas density map  $d_{gas}$  from the previous step and the image  $A$  as reference, we optimize the *dust density map* until the reconstructed model resembles the reference image  $A$ . In this optimization step the nebula is rendered taking scattering and absorption into account as described by Equation 7.1. This time, the emission is derived from  $d_{gas}$ , while  $d_{dust}$  accounts for scattering and absorption. In this process, the emission density map  $d_{gas}$  recovered in step 1 is not optimized anymore. The results of this final optimization step are shown in Figure 7.6.

### Reconstruction Based on Infrared and Visible Datasets

In this approach we use a pair of infrared and visible wavelength images. The first infrared input image, denoted  $I$  (Figure 7.8, left), traces predominantly the dust particles present in the nebula, due to its intrinsic blackbody radiation. The second image, denoted  $A$  (Figure 7.9, left), is again captured at visible wavelengths with a narrow-band  $H\alpha$  filter. It shows the emission of the ionized gas and is affected

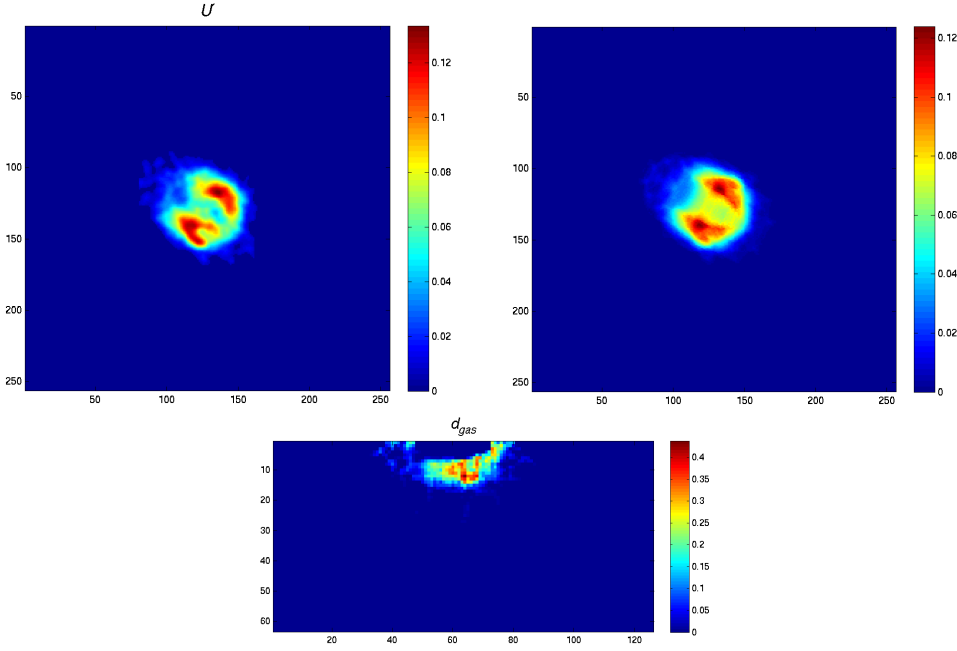


Figure 7.5: Left: Input image for the M3-35 planetary nebula, corresponding to  $U'$ . Right: Rendering of the reconstruction. Some deviations are visible because the input is not perfectly symmetric. Bottom: Recovered gas density map  $d_{gas}$

by scattering and absorption due to the dust. In Figure 7.7, an overview of the reconstruction process using infrared and visible datasets is given. We first reconstruct the dust density map  $d_{dust}$  using the infrared image  $I$ . In a second step, the gas density map  $d_{gas}$  is optimized, until the rendering of the reconstruction which considers the effects of scattering and absorption due to dust resembles the visible wavelength input image  $A$ .

#### *Dust distribution estimation.*

In the first step, the *dust density map* corresponding to the dust particles present in the nebula  $d_{dust}$  is reconstructed using  $I$  as reference image. Because at certain infrared wavelengths electromagnetic emission is proportional only to the dust's intrinsic temperature, we can consider the dust particles being emissive, and the rendering model for infrared observations simplifies to

$$L_{dust}(x, y) = \int_c^\infty L_I^{dust}(v) dv \quad (7.5)$$

where  $L_{dust}(x, y)$  is the measured infrared radiance at position  $(x, y)$  and  $L_I^{dust}(v)$  is the infrared emission of the dust particles. The dust distribution map is estimated using the same iterative non-linear optimization algorithm which has been

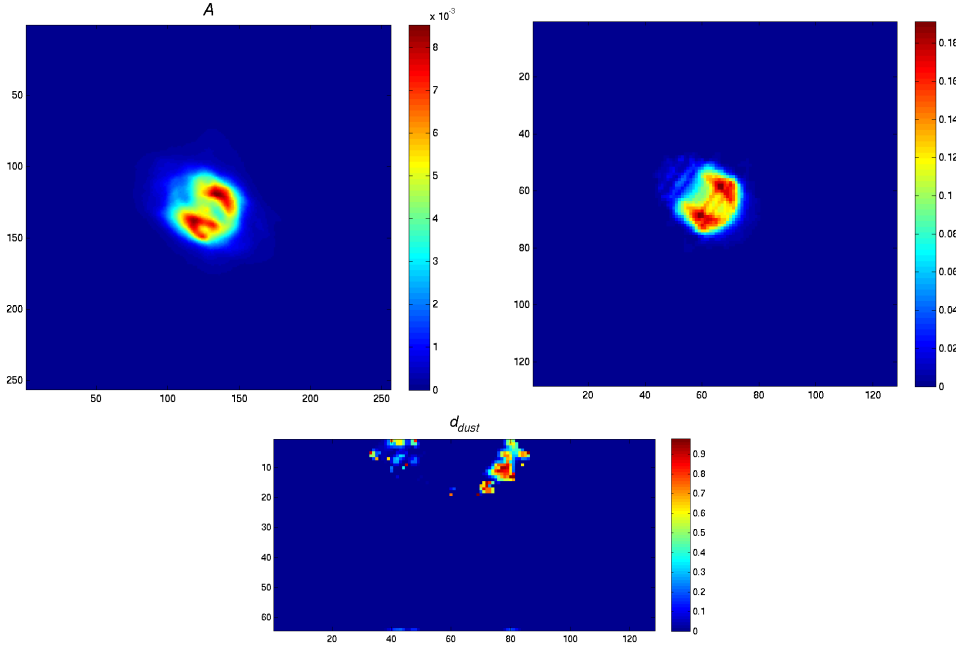


Figure 7.6: Left:  $H\alpha$  image of the M3-35 planetary nebula, corresponding to A. The symmetry axis in this figure as well as in  $U'$  from Figure 7.5 spans from the upper left to the lower right corner. Right: Rendering of the final reconstruction, considering absorption and scattering. Bottom: Final recovered  $d_{dust}$  dust map

applied in Section 7.3.2 in order to estimate the emissive gas distribution. Figure 7.8 shows the reference image  $I$ , the recovered dust density map  $d_{dust}$  and the rendering of the reconstructed volume.

#### *Gas distribution estimation*

In this second step, using the dust distribution map  $d_{dust}$  from the previous step, and image A as a reference, we optimize the gas distribution map  $d_{gas}$  until the rendering of the model resembles image A. In this second step, the dust is no longer treated being emissive and we render the nebula taking into account absorption and scattering as described by Equation 7.1. The result of the reconstruction process is shown in Figure 7.9.

## 7.4 Rendering and Visualization

To visualize the results of the reconstruction we adapted the OpenGL based renderer used for reflection nebulae visualization by Magnor et al. [Magnor et al.

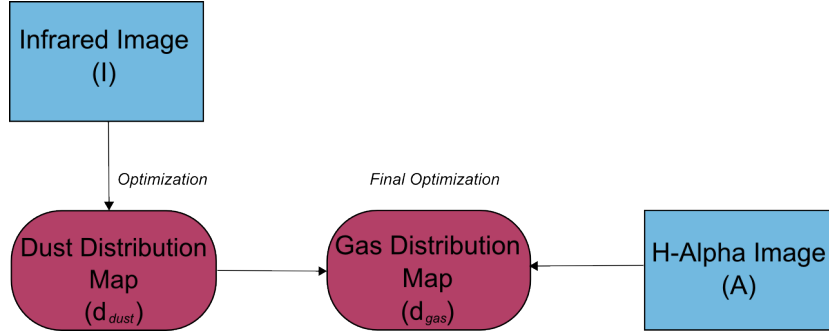


Figure 7.7: Overview of the reconstruction process using infrared datasets.  $d_{dust}$  is estimated from infrared image which corresponds to the black-body emission of the dust. The combined effect of dust absorption and scattering, and the gas emission is captured in  $A$ , from which  $d_{gas}$  can be derived.

2005]. It is a volume rendering application based on a real time ray-caster implemented on graphics hardware. The implemented algorithm uses the idea described by Krüger et al. [Krüger and Westermann 2003] to color code the direction of the viewing rays using a bounding box. In the next step, we exploit modern graphics hardware's capabilities to step along the lines of sight querying 3D textures using a fragment shader to accumulate the emission and in-scattering along each ray while considering absorption. To further increase the frame rate of the interactive visualization tool we extended the existing renderer by implementing *empty space skipping* [Sobierajski and Avila 1995] to improve the volume's bounding geometry.

As another optimization for the rendering, we partially precompute the single scattering term (Equation 7.2) within the map instead of the full volume. The integral  $\tau(x, y) = e^{-\int_{p^{star}}^y \tau(w) dw}$  can be fully determined within the 2D map (see Figure 7.10), which is then rotated around the symmetry axis to compute the in-scattering to each voxel. To the final output, we apply gamma correction and high dynamic range rendering. We achieve about 14 fps, at  $128 \times 128$  resolution.

## 7.5 Results

We have applied the proposed pipelines to two different data sets, a pair of radio and visible wavelength images for the nebula M3-35 and a pair of infrared and visible wavelength images for the nebula Hen 2-320. Computation times for both nebulae range in the scale of 24 hours per dataset / wavelength.

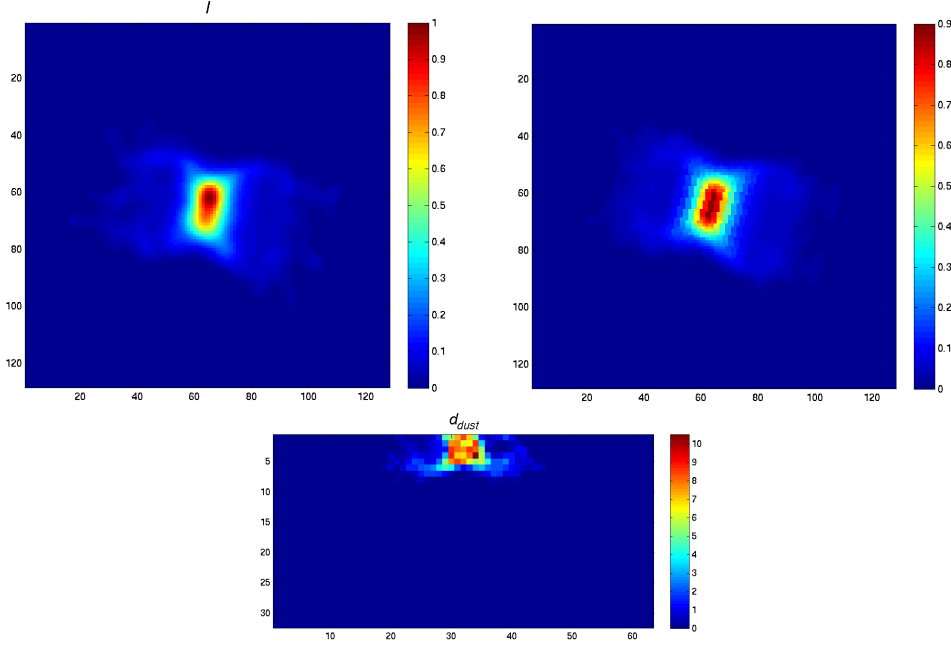


Figure 7.8: Left: Input image for the Hen 2-320 planetary nebula, corresponding to  $I$ . The axis of symmetry spans almost horizontally across the image with a slight tilt. Right: Rendering of the reconstruction. Bottom: Recovered dust density map  $d_{dust}$

For the approach based on radio and visible wavelengths presented in Section 7.3.2, we used data from the paper by Lee et al. [Lee and Kwok 2005], consisting of observations of PNe in the visible wavelengths from the Hubble Space Telescope (HST) and radio data from the Very Large Array radio observatory. These are compact planetary nebulae with a symmetrical form.

For the approach based on datasets at infrared and visible wavelengths described in Section 7.3.2, we combined an infrared dataset kindly provided by Kevin Volk, Gemini Observatory, and visible observations taken with the HST, which are publicly available from the HST Online Archive [NASA 2007].

Because we make use of datasets from different telescopes for the same astronomical object we had to align and to scale the radio / infrared data to match the visible wavelength images. This is necessary because of the positioning uncertainties and the different resolutions of the given telescopes.

In addition, we were not able to obtain absolutely photometrically calibrated images. We therefore included a relative intensity scale between the gas emission and the dust absorption, and the overall intensity of the central star into our optimiza-

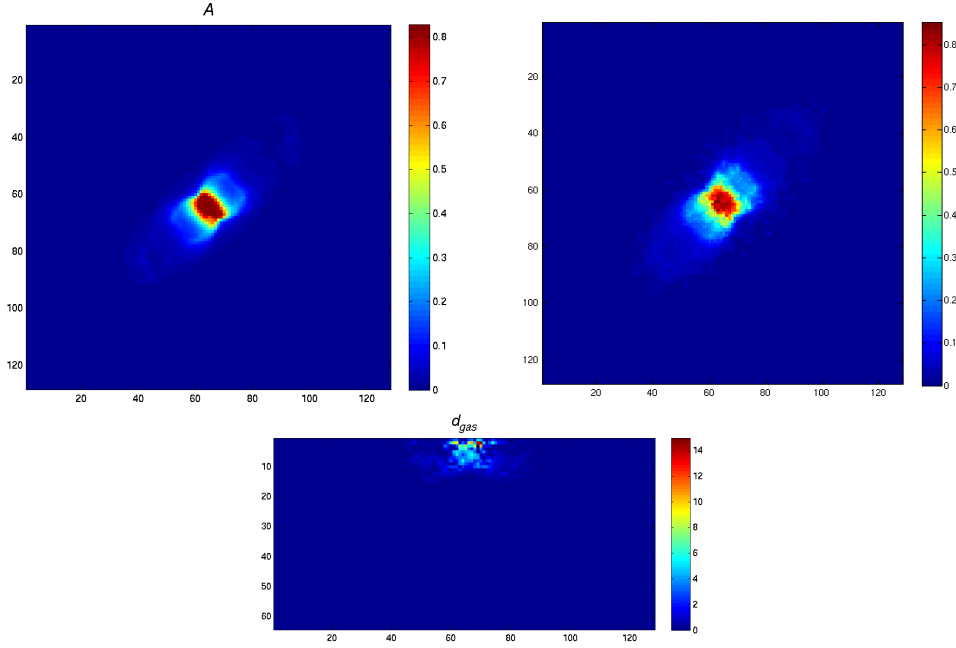


Figure 7.9: Left:  $H\alpha$  input image corresponding to A. The axis of symmetry spans over the diagonal from the lower left to the upper right corner. Right: Rendering of the final reconstruction, considering absorption and scattering. Bottom: Recovered gas density map  $d_{gas}$

tion scheme, adding two global scalar parameters. Using additional calibration data this step could be avoided in order to obtain absolute dust and gas densities which we so far can only estimate up to some unknown factor.

### 7.5.1 Planetary Nebula M3-35

For the volumetric reconstruction of the planetary nebula M3-35 based on radio and visible wavelength images results are shown in Figures 7.5 and 7.6. Our algorithm recovered for this nebula an inclination angle of  $73^\circ$ , which is fairly close to the value of  $80^\circ$  given in [Lee and Kwok 2005]. The reconstructed gas density map  $d_{gas}$  (Figure 7.5, middle) highlights an area of low gas density in the center which corresponds to the input radio map. Because of the slightly asymmetric shape of the real nebula there are however some small deviations in the red top right region. The recovered dust map (Figure 7.6) correctly attenuates the intensity of the bottom right part of the nebula.



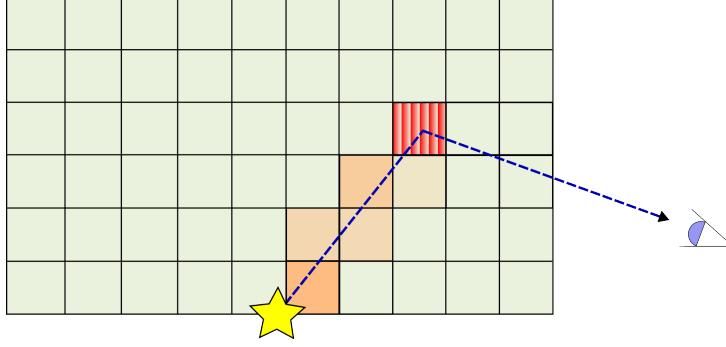


Figure 7.10: 2D Precomputation of the light reaching a voxel (striped texel) from the central star within the map instead of computing it for the full volume. All dust density values on the line from the central star to the texel are accumulated.

### 7.5.2 Planetary Nebula Hen 2-320

The reconstruction results for planetary nebula Hen 2-320 based on infrared and visible wavelength images are shown in Figures 7.8 and 7.9. Our algorithm recovered an inclination angle of  $90^\circ$ , indicating that the symmetry axis is parallel to the image plane. The reconstructed dust density map  $d_{dust}$  (Figure 7.8, middle) reproduces the nebula's butterfly-like lobes visible in the infrared image  $I$  very well, up to the asymmetries of the red center.

Results from the gas reconstruction are presented in Figure 7.9. The map  $d_{gas}$  (Figure 7.9, middle) also succeeds to recover the two butterfly-like lobes noticeable in the  $H\alpha$  input image  $A$ . Currently, we observe slight block artifacts in the final rendering, which might be due to the accumulated effect of the two subsequent optimization steps and their specific errors, which influence each other in a non-linear way. Still, the main structures of the nebula are well represented, indicating a plausible reconstruction. The artifacts can be reduced if smoothness is enforced during the optimization of the gas map.

Figure 7.11, left, shows the difference images after the reconstruction of the dust distribution and respectively right, after the final optimization of the gas distribution. The RMS errors for the  $128 \times 128$  input images are relatively low: 0.0172 and 0.0153, respectively.

From the recovered distributions we can now render the nebula from different view points (inclination angles) as presented in Figure 7.12. The synthesized images provide novel ways for exploring the 3D structure of the nebula.

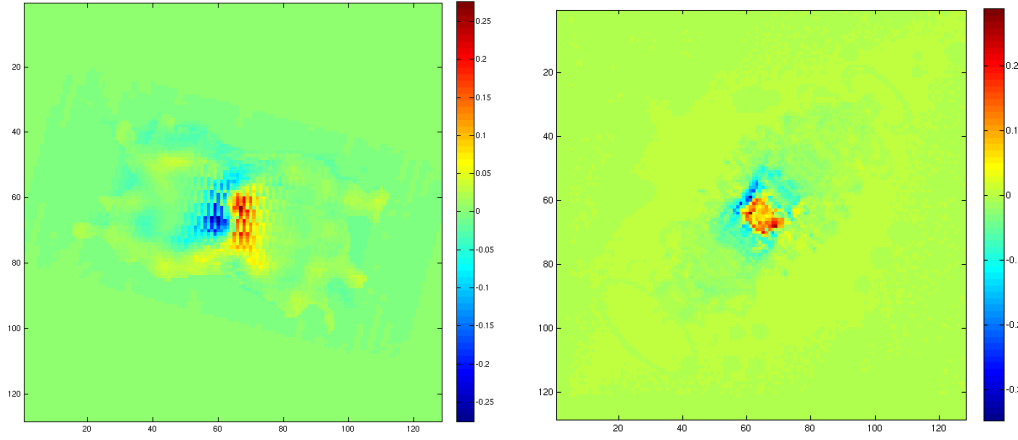


Figure 7.11: Difference between the input images and the reconstructions for nebula Hen 2-320. Left: for the density reconstruction in Figure 7.8. Right: for the gas reconstruction in Figure 7.9.

## 7.6 Discussion and Future Work

The presented results demonstrate the effectiveness of our volumetric reconstruction algorithm for planetary nebulae. Given two input images at different wavelengths, we can recover both the 3D distribution of emitting gas as well as the density of dust particles in axis-symmetric nebulae. Our physically-based reconstruction and visualization algorithms simulate emission, absorption and scattering.

The quality of the reconstruction results is limited by the input images for any recovered gas or dust data. It is important that the input images are well aligned and have similar resolution in order to obtain accurate reconstruction results. Furthermore, any deviation from axis-symmetry in the real nebula affects the reconstructed volumes.

Because we assume axial-symmetry the reconstruction results depend on the inclination angle of the symmetry axis and the projection direction. The best quality is obtained if the symmetry axis is parallel to the image plane.

While our current approach incorporates only two images at different wavelengths and assumes that the image of one wavelength is not at all effected by the dust, further extension of the algorithm could incorporate more images at different wavelengths to increase the stability of the optimization. In addition, it is not necessary to assume that one image is completely unaffected by scattering and absorption.

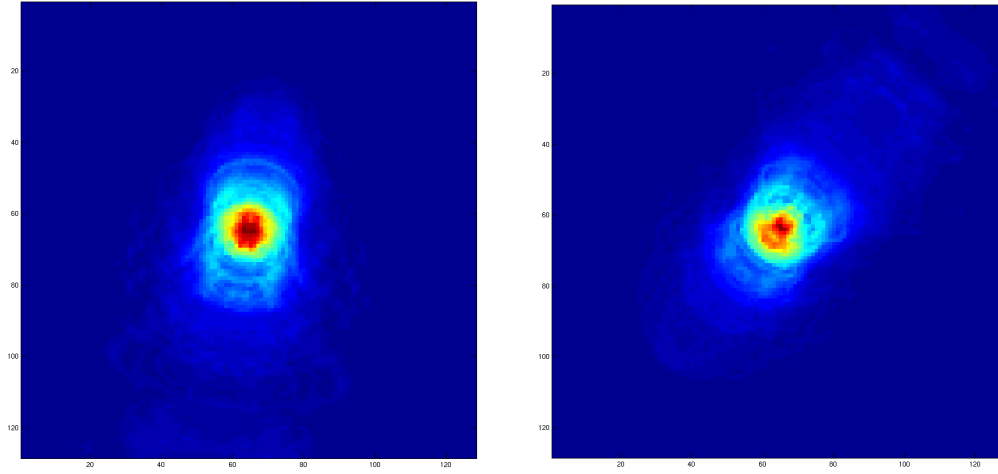


Figure 7.12: Reconstructed He2-320 rendered at an inclination angle of  $50^\circ$  and  $75^\circ$ . By viewing the nebula at different inclination angles, we can derive a better insight in its 3D distribution.

As long as the scattering and absorption coefficients are sufficiently different the ionized gas and the dust distributions could be recovered if optimized simultaneously.

Besides the application in astronomy, it is promising to investigate the performance of the proposed volumetric reconstruction algorithm in the context of medical imaging, where scattering and absorption are the main effects when illuminating through biological tissue.



## **Part IV**

# **An Augmented Reality Application for Educational Astronomy**



---

---

## Chapter 8

# Augmented Astronomical Telescope

Anyone who has gazed through the eyepiece of an astronomical telescope knows that, with the exception of the Moon and the planets, extra-solar astronomical objects are disappointing to observe visually. This is mainly due to their low surface brightness, but also depends on the visibility, sky brightness and telescope aperture. In this chapter we describe a system which projects images of astronomical objects (with focus on nebulae and galaxies), animations and additional information directly into the eyepiece view of an astronomical telescope. As the telescope orientation is queried continuously, the projected image is adapted in real-time to the currently visible field of view. For projection, a custom-built video projection module with high contrast and low maximum luminance value was developed. With this technology visitors to public observatories have the option to experience the richness of faint astronomical objects while directly looking at them through a telescope.

### 8.1 Introduction

Since its beginning, mankind has always been fascinated by the starry sky. It is one of the first natural phenomena that was investigated by humans. An observer starts by learning the constellations in the sky and their relative position by stargazing with the "naked eye". More advanced amateur astronomers make use of *binoculars* and *telescopes* with which many more objects can be observed.

Goto (motorized) telescopes are gaining in popularity. Many newcomers purchase one as their first telescope. These telescopes find a target object in the sky by following its selection from a hand controller. The user then expects for an "instant success" in the observations. This surely happens when "easy to observe", bright objects such as the *Moon* or *the planets* are the targets. However, when observing faint *deep sky objects* (astronomical objects which lie outside our solar system) like galaxies or nebulae, much of the initial enthusiasm is lost. These appear as fuzzy grey spots in the telescope's eyepiece and leave the observer quite unimpressed, possibly thinking about giving up his new hobby. The main reason is that the image in the eyepiece is not really similar to the well known images recorded by the Hubble Space Telescope [NASA a] (or some other large aperture Earth-bound telescopes) which are familiar to the newcomer through astronomy websites or magazines.

One possibility to attain interactivity during astronomical observation is to use an *electronic eyepiece*, a *web-cam* or a custom *CCD camera* to display the live image formed at the telescope focus on a TV or computer screen. However, this approach only works for bright astronomical objects and needs a skilled observer to fit the image of the desired object on the CCD chip.

We propose a system which augments the view through the eyepiece of an astronomical telescope in order to provide additional online information to the user during observation. The system overlays the currently visible object with a long exposure image of it, as a visual aid. The present orientation of the telescope is continuously queried and the currently visible sky section is computed in real time by a portable computer. It is also possible to overlay animations for specific objects. The system is not meant to replace traditional deep sky observation. Rather, it is intended more as *educational* and *visual aid* for the novice astronomer.

The main motivation of our work is to increase the interest in astronomy among the general public who are quite unimpressed after their first glimpse through a telescope. As the human eye has a limited capacity to integrate capture light over time, faint deep sky objects are perceived vaguely, and the observer cannot determine their structure. Our system gives observers the ability to simultaneously compare the visually perceived object with a photograph acquired using long exposure. When observing the planets it is often difficult to identify their natural satellites because of their fast movement relative to the position of the planet due to short orbital periods. Our system can help the stargazer by overlaying the names of the visible natural satellites. The same approach is used when observing dim stars which can also be hard to identify in a field containing a considerable number of stars.

In the following section we present an overview of the related work in the field



of tracking and registration augmented reality applications. Section 8.2 provides a short system description. We describe the telescope's optical characteristics in Section 8.3 and discuss about its pointing and tracking accuracy in Section 8.4. We present the custom-built projection device in Section 8.5. The human visual system's adaptation is shortly reviewed in Section 8.6. Section 8.7 introduces the custom planetarium software used in our application and Section 8.8 describes the input unit in use. We bring up some possible applications in Section 8.9 and we conclude and point out possible future work in Section 8.10.

## 8.2 System Description

Our system augments the view of the skies through an astronomical telescope. The hardware part consists of a *telescope* fitted with a goto mounting, a custom built *projection unit* and a *portable PC*. The software part consists of the customized *planetarium software* and the integrated *telescope communication module* (See Figure 8.1).

The working principle of the system is the following: the telescope is pointed towards the desired astronomical object selected via the hand controller unit. The actual telescope position is constantly queried by the telescope communication module. Using the current coordinates, the planetarium software focuses on the corresponding sky section which is directly projected onto the telescope's image plane by the projection module. The projected image is then combined with the optical image seen through the telescope using a beam splitter.

The planetarium software contains a database of locations and additional details about the planets in our solar system, a large number of stars and interesting deep space objects. It provides high resolution photographs, 3D animations (when available) and supplementary data. The user can customize the exact information displayed for individual objects, and it is possible to switch between various eyepieces (i.e. magnifications) during observation. This approach provides information beyond that available via the standard hand controller. The telescope used in our application is a 10" aperture (250 mm), Meade LX200 GPS, Schmidt Cassegrain model (See Figure 8.3, Left), equipped with a goto mounting, but the working principle of the system can be applied to any telescope fitted with goto mounting. Figure 8.2, Left shows a possible image perceived by an observer when looking through the telescope's eyepiece at the Andromeda Galaxy (M31). Figure 8.2, Right, presents, the same sky section, after the long exposure photograph and additional information have been projected onto the telescope's image plane. Another important aspect of our system is the maintenance of the *dark adaptation*

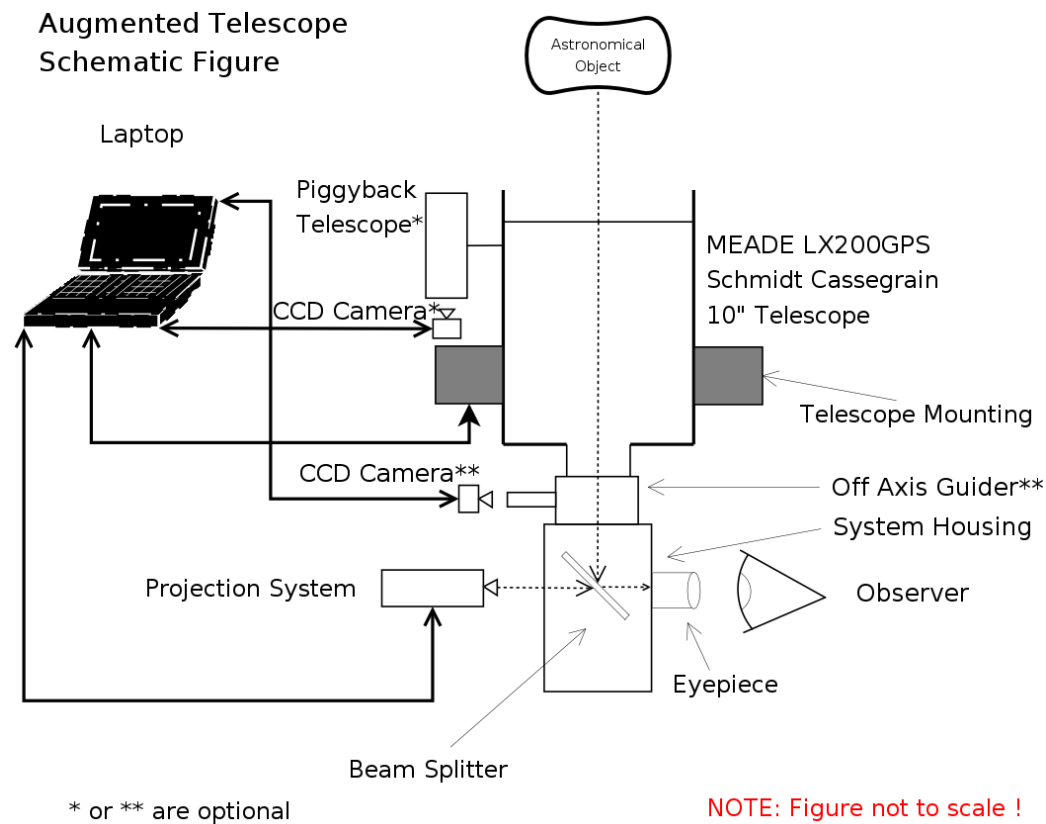


Figure 8.1: Schematic description of the entire system. To improve the tracking accuracy, a special purpose, high sensitivity CCD camera can optionally be added (components marked with \* and \*\*). It can be mounted together with a smaller piggyback telescope or directly on the optical axis of the telescope using an off axis guider

of the observer when projecting the additional information into the telescope's field of view. For this reason the projection module is equipped with a knob permitting continuous brightness adjustment and a tray to insert additional neutral density filters.

### 8.3 Telescope Optical Characteristics

This section deals with the optical properties of the telescope in use. As shortly described earlier, the telescope used in our application is a 10" aperture (250 mm), Meade LX200GPS, Schmidt Cassegrain model (Figure 8.3, Left). It has a focal

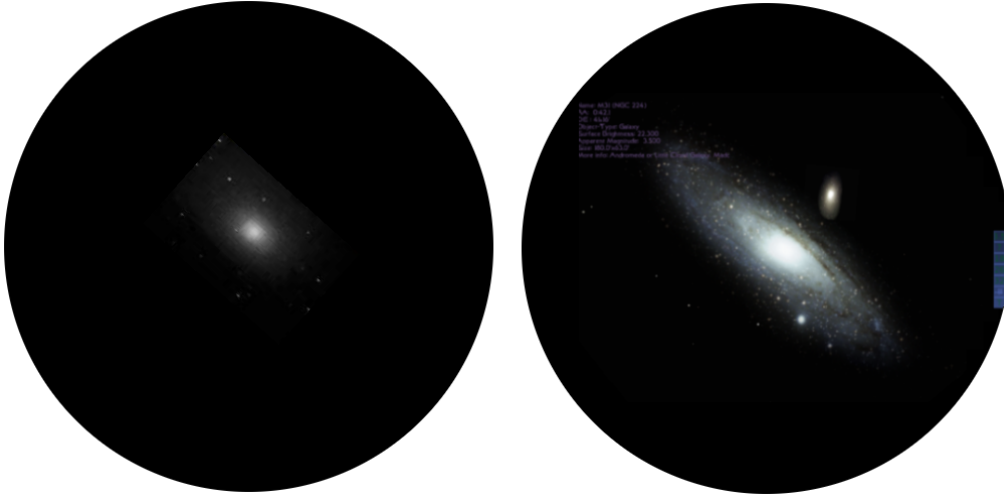


Figure 8.2: *Left*: Standard Eyepiece View. The image shows the visual appearance of the Andromeda Galaxy (M31) through an eyepiece (from [Daly 2005], courtesy Leo Taylor). *Right*: Augmented Eyepiece View. A sight of the same field of view with the overlaid image and additional information blended into the upper left corner.

length of 2500 mm and is equipped with a goto mounting. A telescope, when used in astronomy mainly serves three functions: *magnification*, to increase *light grasp* and to increase *resolution* [Tonkin]. The magnification provided by a given telescope eyepiece combination can be simply computed by: *telescope focal length / eyepiece focal length*. With our available eyepieces we can obtain magnifications ranging from 78x (32 mm eyepiece) up to 500x (5 mm eyepiece). The light grasping capability of a telescope is given only by the diameter of its main objective. Knowing this, we can compute the limiting magnitude of the telescope, i.e. the faintest star which can still be observed through the telescope. The resolution of a telescope is the angular limit at which two close distinct stars can be still perceived as two different objects. The diffraction limited resolution of the telescope for a given wavelength can be simply computed once the aperture of the main objective  $D$  (mm) is known by the following formula:  $115.82 / D$  (arc-seconds). Our telescope has the resolution is 0.46 arc-seconds for a wavelength of 555 nm. This theoretical maximum optical resolution can hardly be achieved because of the atmosphere which limits the seeing to a value between 2 and 10 arc-seconds, and can sometimes be 1 arc-second at good observing sites.

An observer, when using the proposed system, can compare the actual optical image of an astronomical object with a brighter and higher resolution image. This way we augment the telescope's limited resolution and light gathering power.



Figure 8.3: Left: The Meade LX200 GPS 10'' Astronomical Telescope used in the application. Right: The hand controller provided with the telescope

## 8.4 Telescope Pointing and Sidereal Tracking Accuracy

The telescope used in our application (See Figure 8.3, Left) is equipped with a GPS receiver and is capable of calibrating itself by determining the mount's *tip*, *tilt* and *true north* [Meade Instruments Corp. 2003]. True north is computed using magnetic north but due to magnetic disturbances and variations of the Earth's magnetic field is not accurate enough. For a precise calibration two bright stars have to be successively centered in the telescope's eyepiece. After calibration the user can choose to observe one of the objects available in the telescope's hand controller unit (See Figure 8.3, Right), and the telescope slews directly to the desired object.

There are two different types of accuracy which have to be taken into account: *pointing* and *sidereal tracking*. Pointing accuracy is the precision with which the telescope aims at a given astronomical object in the sky. The most important factor on which it depends is the positioning of two calibration stars exactly in the center of the eyepiece. This can be achieved using an illuminated reticle with a cross-

line intersecting in the eyepiece's center. Also, to maximize calibration accuracy, the two chosen stars should be situated at least  $90^\circ$  apart in the sky. The tele-

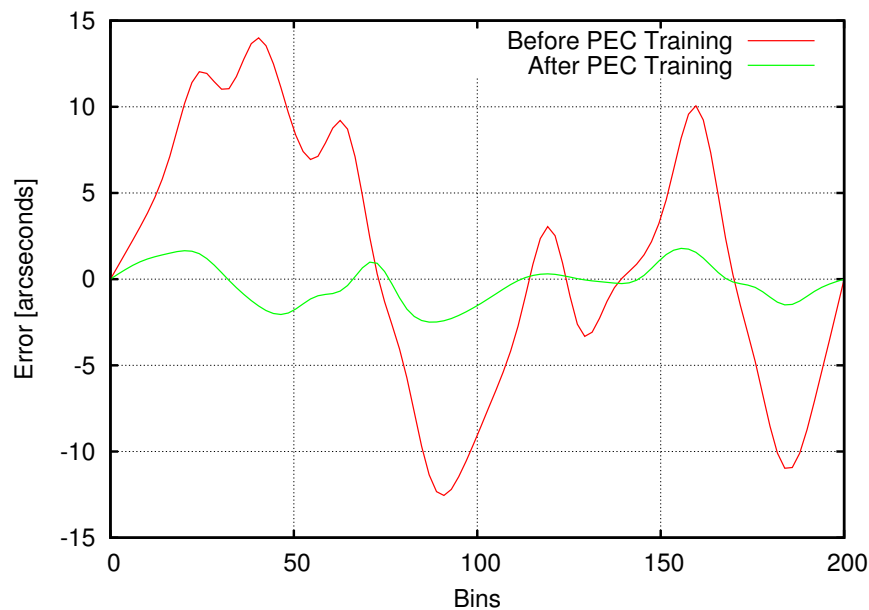


Figure 8.4: Telescope tracking accuracy before and after PEC training over an 8-minute period. Note the visible accuracy improvement after a simple training session, after Greiner [Greiner 1998]

scope's pointing precision given by the manufacturer is of 2 arc-minutes [Meade Instruments Corp. 2003]. If the telescope is correctly aligned as described above and the user uses the available *high precision* feature (the telescope first slews to a nearby bright star, the user centers the bright star in the eyepiece and the telescope slews afterwards to the desired object with higher accuracy) much higher precision can be attained. Also, at any point during telescope operation, the user has the option to manually correct / change the telescope's orientation. The telescope's mount sends updated position information approximately every 1 second, with an accuracy of up to 1 arc-second.

During sidereal tracking (the speed the Earth rotates around its axis) of an observed object, accuracy is of major importance for the correct overlapping of the observed and projected object. The actual position indication of the telescope's mounting (approximately once per second) could be precise, but there is also an inaccuracy in the mounting's gears. This inaccuracy can be improved by per-

forming a so called *Periodic Error Correction* (PEC) [[Meade Instruments Corp. 2003](#), [Greiner 1998](#)] on the telescope to "train" the drives, which is also used for high-precision astrophotography applications. The graph in Figure 8.4 presents the sidereal tracking accuracy of the telescope in use over a period of 8 minutes (200 intervals of 2.4 seconds each). Before PEC training the peak to peak tracking error is up to approximately 25 arc-seconds, after a training session it is reduced to 5 arc-seconds or less. A tracking error of 5 arc-seconds is equivalent to the size of a small crater on the Moon measuring 9 Km in diameter. As comparison, the true field of view when using the 32 mm eyepiece on our telescope is approximately 30 arc-minutes or 108000 arc-seconds (the size of the Full Moon), the maximum tracking error after PEC training equals only 0.0046 % of the full field of view.

After the first tests with the prototype version of our projection module we were satisfied with system pointing and tracking accuracy. When slewing to the Andromeda Galaxy (M31) using the 32 mm eyepiece (78 x magnification), the projected image and the optical image of the galaxy were both in the eyepiece's field of view.

## 8.5 Projection System

There are several criteria which have been taken into account for the development and design of the projection module suited to our application. Its size and weight should be minimized to preserve the freedom of movement of the telescope and to maintain its weight balance. The projection module also should have the highest possible contrast ratio, so that the user is still able to discern between black and white levels when projecting at low brightness levels.

Another important requirement is a low brightness at the displays "black" value; LCDs for instance tend to emit a small amount of light even when set to black. After researching the currently available projection technologies, we concluded that the best fit to all these requirements is a solution using DLP (Digital Light Processing) [[Texas Instruments 2004 - 2007](#)] (See Figure 8.5). A photograph of the designed projection module together with the 32 mm eyepiece is presented in Figure 8.6.

The module utilizes a 0.7"-diagonal DMD (Digital Mirror Device) with XVGA (1024x768) resolution and the whole projection unit was developed by Op-Sys Project Consulting [[Jacobsen 2005](#)]. It features a custom projection lens and a special color LED projection head. The LED light source reduces size considerably, as there is no need for a color wheel used in standard DLP projectors. The

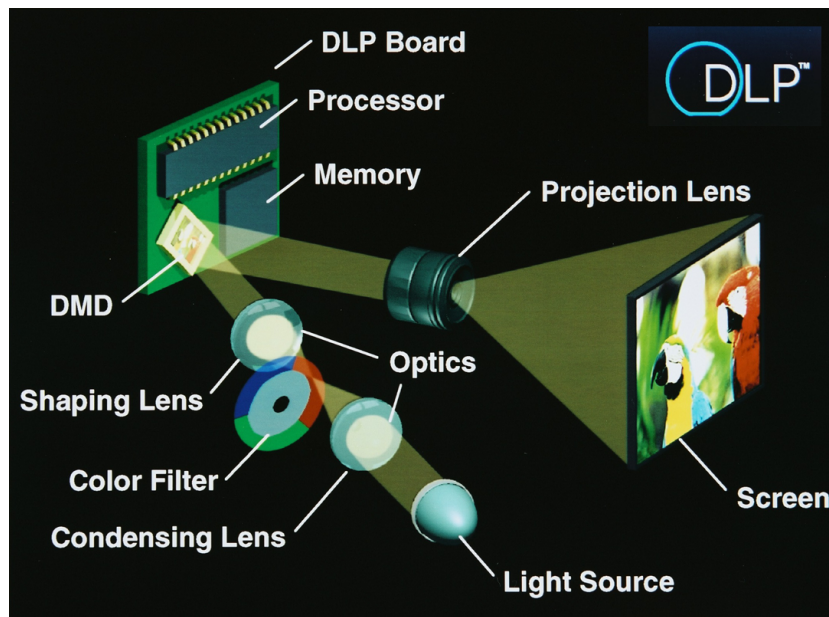


Figure 8.5: A schematic description of the DLP working principle. Light coming from the light source is modulated by the Digital Micromirror Device (DMD) after passing through special optics. A projection lens then projects the image on a screen. In our system the traditional light-source and the color wheel are replaced by a set of color LEDs, and the image is small, projected inside the whole projection unit. Image courtesy of Texas Instruments [Texas Instruments 2004 - 2007]

maximum luminance is  $1.8 \text{ cd/m}^2$  and is dimmable down to  $0.03 \text{ cd/m}^2$ . The minimum contrast of 500 : 1 is maintained over the complete luminance range varying from the maximum value down to  $0.3 \text{ cd/m}^2$  and decreases for lower values. To dim the projection module down to values not affecting low adaptation levels, a fixed neutral density (ND) filter is installed in front of the LED's. There is also an optional tray to insert additional ND filters (Figure 8.8, Right) when still lower maximum luminance values are needed e.g. for very faint nebulae. The advantage in using the ND filters is that we can obtain lower projection luminance values without dimming the LED's to the range where contrast loss occurs. We have a set of ND filters in the transmission range varying from 70% to 0.3%. However, for observing most objects of interest, the user does not have to change ND filters, a medium transmission ND filter does the job well. To combine the projected and optical image we use a beam splitter which transmits 90% of the light coming from the telescope and reflects only 10% of the light coming from the projection engine. Figure 8.7, presents the projection system mounted on the





Figure 8.6: A photograph of the projection system together with the 32 mm eyepiece. It is directly mounted on the telescope's optical axis through the flange on the bottom side. The eyepieces in use are placed in the provided holder on the right side. The DLP engine and LED head are situated in the box on the left. The box in the middle contains the 45° mounted beam splitter

telescope's optical axis.

As mentioned above, we use a combining mirror to overlay the telescope image and the projected image. After optimizing the beam splitter's anti-reflective coating and placing a polarization filter in front of the projection unit, multiple ghosting artifacts showing up in earlier prototype versions could be minimized. In its current state, just one faint ghost image of the projected information can be observed through the eyepiece.

Because of the different *image ratios* and *geometric shapes* of the eyepiece view (circle, 1:1 ratio) and the projected image (rectangle, 4:3 ratio), a compromise between the number of pixels of the projected image which are invisible and the surface of the eyepiece image with no projection coverage has to be found. We also have to take into account the possibility to use eyepieces of different focal length which yield different magnifications. To still get acceptable coverage of the visual field by the projected image when using higher magnifications (24mm, 104x), the field of view when using the lowest magnification eyepiece (32mm, 78x) is not totally covered by the projected image on the margins.

We propose as a solution to the coverage problem when using the 24mm eyepiece





Figure 8.7: The projection unit together with an eyepiece mounted on the telescope. The figure also highlights the path light from the currently observed astronomical object and the projector travels. The beam splitter combines these images and the observer magnifies the final image using an eyepiece

the setup presented in Figure 8.8, Left. It offers a fair tradeoff between the area of the eyepiece view with no projection coverage (small top and bottom area) and the unused pixels of the projected image (four small corner regions) for the given eyepiece.

When overlaying the projected image on top of the optical view we want to have the images of the astronomical objects displayed with the correct orientation in the frame. To find this for every observed object we only have to take into account the angle with which the projection engine is rotated in the plane perpendicular to the viewing direction. If we rotate the entire projection unit in the plane perpendicular to the optical axis of the telescope, the projection unit and the eyepiece rotate together, not influencing the overall correct orientation of the projected data.

An important additional control on the unit is a potentiometer knob which allows continuous adjustment of LED brightness. This assures one can keep low luminance values during projection thus maintaining the user's dark adaptation. The unit is powered by a 12 V adapter so that it can be operated together with the telescope using a standard car battery, or other portable power supply, when needed. Even though the projection system was designed to have lowest possible weight,

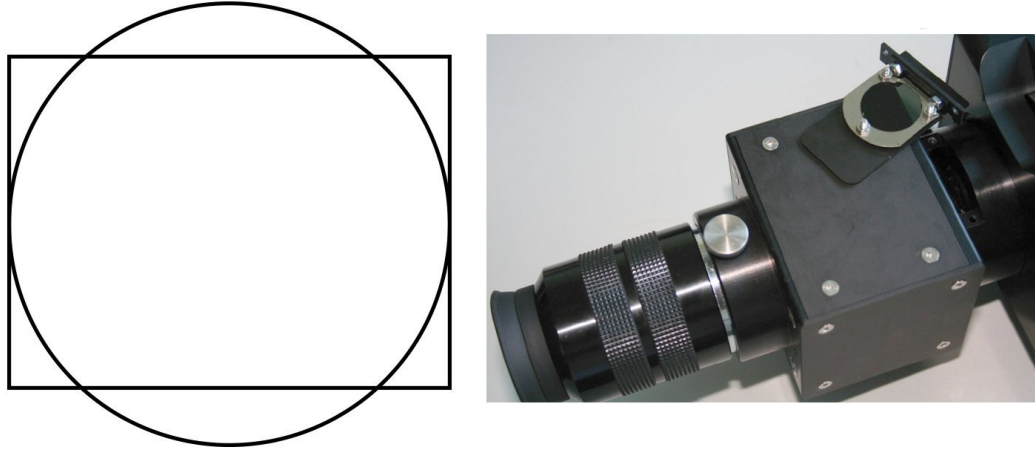


Figure 8.8: Left: Projection coverage (rectangle) for the 24 mm eyepiece field of view (circle). Right: The tray provided to insert Neutral Density filters, directly in front of the projection lens

the telescope needs to be balanced in order to keep the pointing and tracking accuracy unaffected and not to wear out the telescope's gears. Telescope balancing is achieved using a standard Meade accessory, a counterweight set attached to factory drilled holes on the bottom of the telescope's optical tube. The projection unit without eyepiece weights approximately 2 kg, the wide angle 32 mm eyepiece approximately 500 g.

## 8.6 Adaptation of the Human Visual System

The range of luminance values in our surrounding environment is large. The human eye has an effective adaptation mechanism to allow perception of visual information along this range. A mix of mechanical, photochemical and neural processes are responsible for adaptation at different illumination levels. The iris is responsible for limiting the aperture and thus the amount of light entering the eye. The size of the pupil can range from 7 mm down to 2mm. Responsible for the photochemical processes are two types of sensitive cells situated on the retina, the *rods* and the *cones*. At different incident luminance values, various light sensitive cells on the retina are active [Ferwerda et al. 1996, Clark 1990]. The rods are very light sensitive but achromatic and are active at *scotopic* levels of illumination,

from  $10^{-6}$  to  $10 \text{ cd/m}^2$ . The cones are less sensitive but deliver color vision and are active at *photopic* levels of illumination, from  $0.01$  to  $10^8 \text{ cd/m}^2$ . For light levels ranging from  $0.01$  to  $10 \text{ cd/m}^2$  called *mesopic* levels, both the rods and the cones are active [Ferwerda et al. 1996]. The range of luminance values and the corresponding visual functions of the eye are presented in Figure 8.9.

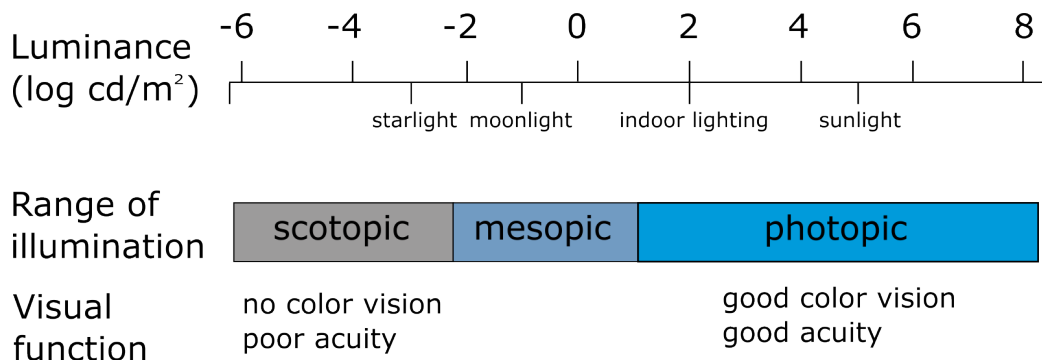


Figure 8.9: The range of luminance values and the corresponding visual parameters. After Ferwerda et al. [Ferwerda et al. 1996]

Adaptation to different levels of illumination is not immediate, as the human visual system needs time to activate and deactivate its photosensitive cells. *Light adaptation* is relatively fast; 80% of sensitivity is recovered in 2 seconds. *Dark adaptation* takes much longer; complete adjustment requires roughly 30 minutes [Ferwerda et al. 1996, Clark 1990]. For projection applications used during astronomical observation it is very important to maintain the observer's dark adaptation, because once exposed to higher levels of illumination re-adaptation occurs too slowly for an immediate perception of faint sky objects.

Looking at the projection module with the above mentioned facts in mind, we try to keep the projected luminance values in the range of scotopic or mesopic levels. Even if the projection module possesses a potentiometer for dimming the intensity values and has the possibility to use neutral density filters, an option for adjusting the brightness of the overlaid information relative to the observed object would be welcome. This approach would support the human visual system's *adaptation*, having similar levels of brightness at spatially close areas.

The planetarium software used as basis for our customized software implements a fast version of the tone mapping algorithm by Tumblin and Rushmeier [Tumblin and Rushmeier 1993]. It also includes a blue-shift of the color hues in the case of scotopic levels of illumination [Wann Jensen et al. 2000], to be able to easier simulate night-time scenes, when viewed under normal daylight illumination.

The scope of our system is not to simulate the exact levels of incident illumination during stargazing, instead we want to provide the user visual information about the observed object in the same time maintaining as much as possible her / his adaptation level. In order to achieve this we remove the blue-shift of the color hues from the original tone mapping scheme and apply the same levels of tone mapping not only to the textures, but also to the additional information displayed for an observed object. This way the user can maintain her / his level of adaptation suited to perceive the observed object. In the case the projected captions are much brighter than the observed object, it can happen that the observer's detection threshold changes, not being able to perceive details in the observed astronomical object [Ferwerda et al. 1996].

## 8.7 Customized Planetarium Software

As basis for our custom planetarium software we use the OpenGL driven open source software *Stellarium* [Chéreau 2005]. It has an easily customizable user interface and new custom objects can easily be added. There is no telescope communication support, so it is extended it by implementing the Meade Telescope Control Protocol [Meade Instruments Corp. 2002]. Support for animation playback is also implemented in our customized version of the software.

Stellarium uses the Hipparchos Catalogue, a star catalog which contains over 120000 stars, a number which is by far satisfactory considering our application. Position information regarding objects in our solar system is also available including major natural satellites of the planets. To have an acceptable number of nebulae and galaxies of interest accessible, we augmented the existing list including only the Messier objects with the objects from the *Appendix E* of Clark's book [Clark 1990], available also online from [Clark 2002]. This list includes 611 deep sky objects, which as Clark states are "the most interesting for amateur astronomers". Additional information about the objects have been downloaded from the NGC-IC project webpage [Corwin Jr. 2005]. We set the same coordinates for the objects in our database and the corresponding objects from the telescope's hand controller, to make sure no telescope pointing errors due to different coordinates can occur.

In order to place all objects in the database at the right position on the simulated sky hemisphere various input data are necessary. Of major importance is the *date* and the *time* of the observation. The *location* of the telescope on Earth is also crucial; all these data are downloaded by the software from the telescope, to assure full consistency. Using this input information the planetarium software computes

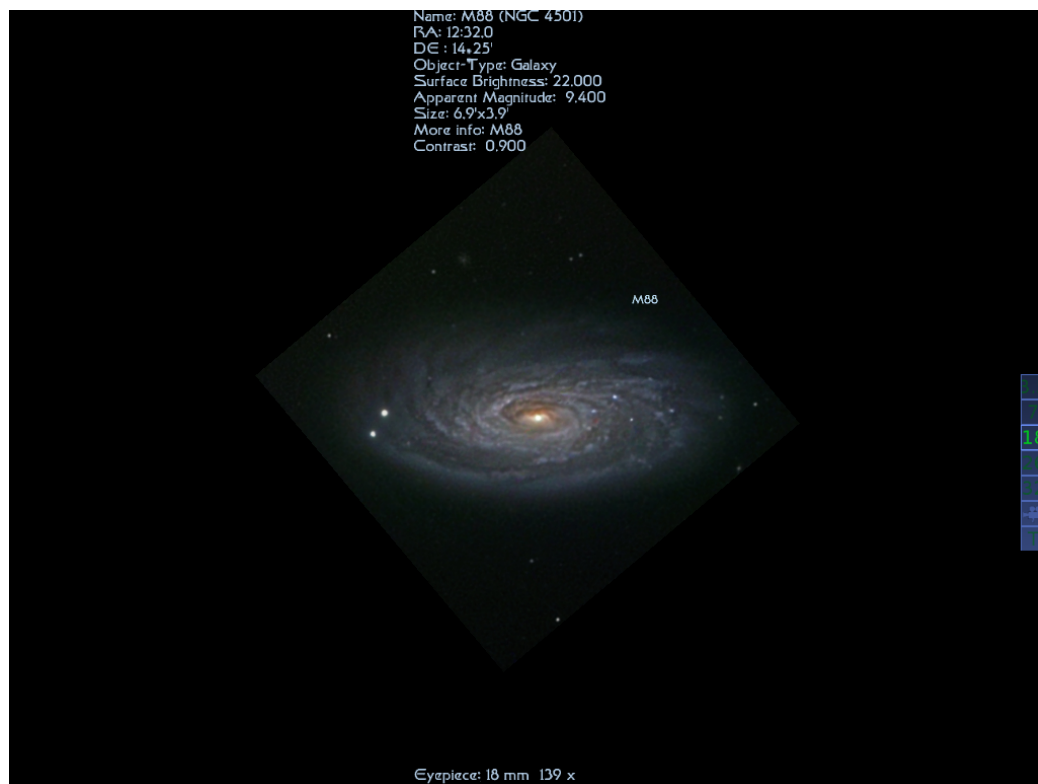


Figure 8.10: Screenshot of the display output produced by the planetarium software. In the top region of the display basic information about the observed object is displayed. On the right side, the menu for specifying the current eyepiece is visible. In the middle bottom region, the selected eyepiece and corresponding magnification are displayed. The photograph of the object is displayed centered and with the correct orientation (M88 photograph courtesy of Rob Gendler [[Gendler 2007](#)])

the position of the objects on the hemisphere by transforming the given equatorial coordinates in local altitude-azimuth coordinates (See Appendix). We read out the location the telescope is pointing to and focus the planetarium software on the same sky region.

One of the main attributes of an astronomical telescope is that by using *eyepieces* of different focal length, one can achieve various magnifications. Therefore a prerequisite for the correct functioning of the system is to specify the current eyepiece. A snapshot from the customized planetarium software is presented in Figure 8.10. On the right side the observer can select the currently used eyepiece from a menu or an animation related to the observed object can be played. In the top region basic information about the currently observed object is visible.

The information in the bottom region provides the currently used eyepiece and its corresponding magnification. The long exposure photograph of the object is placed centered and with correct orientation in the frame (See Section 8.5). For the deep sky objects included in our planetarium software the source for high resolution textures were [NASA a, Gendler 2007, Croman 2005].

After the first field tests of the prototype during night-time conditions, we found it practical for the projection approach to have the option to offset or to turn off completely the overlaid image. This gives the user the ability to observe and compare both images. In the current implementation of the system the user can choose between displaying the projected image of the currently observed object overlaid, offset or no image at all. However, if the user chooses to offset the projected image, the observer has to consider that both images have to fit into the eyepiece's field of view.

### 8.7.1 Field of view calibration

The planetarium software in use has the option to specify the magnification used during observation. For practical reason, the size of objects projected into the eyepiece view should match the size of the objects directly observed on the night sky. The main factor influencing the size of the projected image perceived by the observer is provided by the OpenGL field of view (FOV) used in our software. The absolute size of the objects displayed in our planetarium software can only be approximated when viewed through the eyepiece and thus we have to calibrate it. We use a simple approach: with the projection unit mounted on the telescope, we take separate photographs of the Moon and of the projected Moon texture at the magnification corresponding to the eyepiece in use (See Figure 8.11). We compare the two photographs to determine the scaling factor needed for the observed and approximated magnification factors to match. After matching the curvature of the Moon a scaling factor of 40% was computed with which the approximated FOV has to be decreased.

### 8.7.2 Additional Information

To help the user navigate through the sky we blend various additional information about the observed objects directly into the eyepiece view. Basic information such as *name*, *position* (Right Ascension and Declination, see Appendix for details), *overall brightness*, *surface brightness* and the *contrast relative to the background* of the observed object are overlaid. Further useful information such



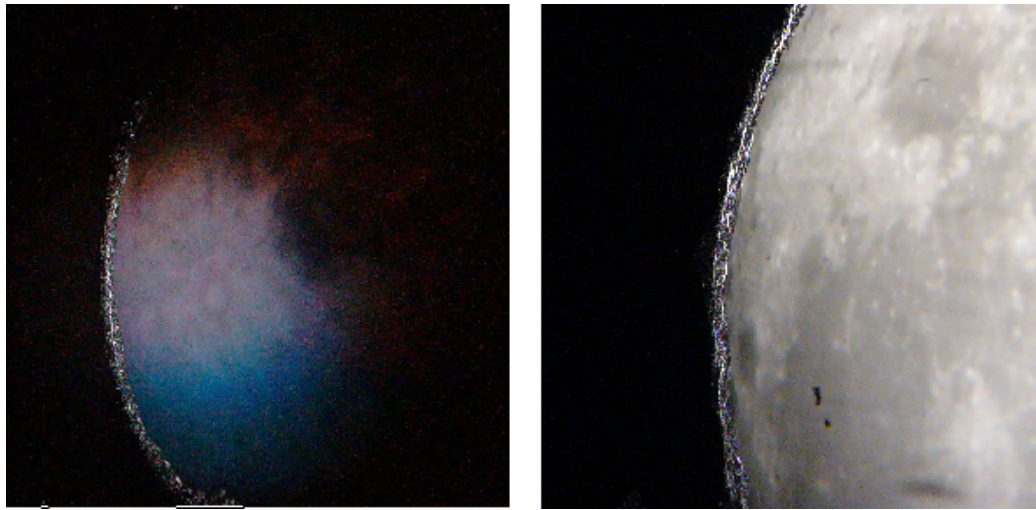


Figure 8.11: Images used for FOV calibration. Left: Picture of the Moon texture from the planetarium software before FOV calibration. Right: Picture of the Moon. Both images taken through the eyepiece. We overlaid the output of an edge detection filter on the photographs to better distinguish the curvatures of the Moon's silhouette

as the object's type and classification, the page where it is referenced in several widely used sky atlases, absolute magnitude or the constellation where it is found can also be customized to be directly blended into the telescope's image plane. All this additional information has high practical value during astronomical observing, assisting and helping the telescope user. Another advantage is that the information usually printed via scrolling text on the hand controller's display is available when looking through the eyepiece. This means that the user doesn't always have to switch between eyepiece and hand controller to gather information about the observed object.

As a visual observation aid, there is an option of overlaying the observed optical image with a long exposure astro-photo of the same object. Another option is to blend in animations of nebulae or galaxies which have an already reconstructed 3D geometry [Magnor et al. 2004, Magnor et al. 2005], animations showing the object's evolution in time or virtual flybys. With the proposed system, useful informations about *practically viable* magnifications for the target object can also be directly blended into the user's field of view, thus improving the visual perception of the visible object.

Our system also assists the user during planetary and dim stars observation. The major planets of our solar system are quite easy to recognize unlike their natural

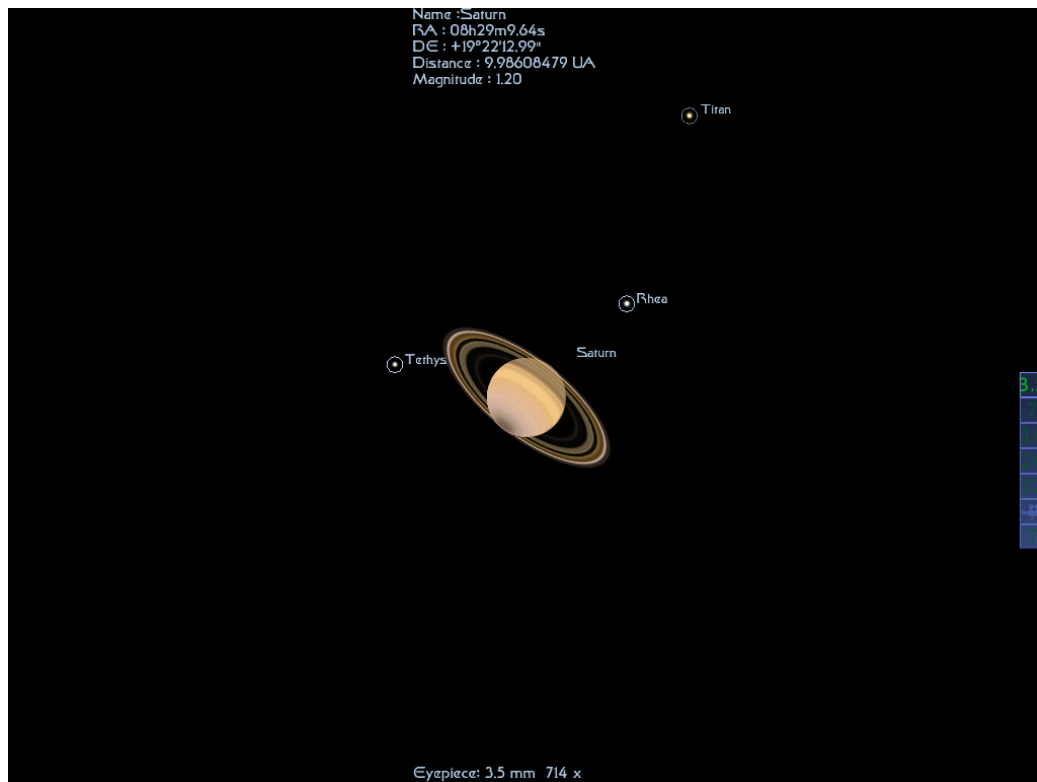


Figure 8.12: Snapshot of the planetarium software focused on Saturn. Three of its major natural satellites are visible, each highlighted with the corresponding name. Thus, locating small moons is made much easier

satellites. Their position relative to the parent planet changes very quickly (in matter of hours) and are therefore hard to locate for the beginner. The systems helps the observer identify outer planets and fainter stars also, which are not straightforward to identify due to their small size and low luminance values. In all the cases mentioned above, the name of the currently selected object is blended into the field of view of the user (See Figure 8.12).

## 8.8 Input Device

The input device of our prototype system was a standard keyboard. The requirement of having a PC in the field can simply be satisfied. Nowadays almost every amateur astronomer has a portable PC available during observation. It is usually used for astro-photography or as an optional control unit for pointing the tele-



scope to objects of interest on the sky. However, the high luminance value of the computer's display (even if dimmable) can result in partially losing the observer's dark adaptation. There is also much time lost by constantly switching between the PC keyboard / mouse and the telescope's hand controller. Based on the above mentioned facts, it is desirable that the user is able to control both the telescope and the whole AR system by the means of the already provided hand controller (See Figure 8.3, Right). The application's few and simple menus can easily be controlled with the available hand controller keys. This option was not implemented in our first prototype version of the system.

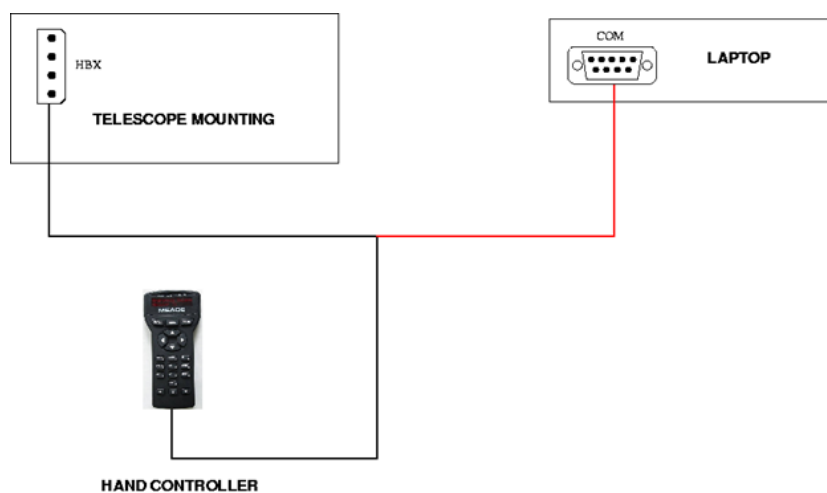


Figure 8.13: A schematic drawing of our modified connection cable for the hand controller. The additionally added connection is highlighted in red

We recently built a custom cable in order to intercept the codes of the pressed keys on the hand controller, Figure 8.13. It is attached to the PC via a DB9 connector on the COM port. The most important menu action which is executed during normal operation is changing the magnification i.e. the eyepiece in use. We assign the "?" key from the hand controller (See Figure 8.3) to this command (it is normally used to display a help message, which can be disabled by pressing the MODE key once). The user has to press the "?" several times to scroll through the available magnifications and select the desired one. After future field tests of the system we will be able to assign other hand controller key combinations to frequently used menu actions.

## 8.9 Fields of Application

The projection unit developed for our application was designed taking into account special requests to be applicable in the field of observational astronomy. However, due to its high contrast and relatively small size, its applicability is not limited to this domain and can be used in any application where augmenting the view through an optical aid is needed.

The designed projection system together with a custom software unit can be used in many other domains. It can be put into practice in fixed applications similar to the Augmented Reality Telescope [Zoellner et al. 2005, Stricker 2005] or the Timescope [ArtCom 2005] at cultural heritage sites. At major tourist attractions sites or at sites with panoramic views an application fitted with a software projection engine like Google Earth [Google Inc. 2005] can be used to overlay information like roads, buildings, geographic features, census data or information about stores and recreation areas. The advantage of our system over any video see-through application is the high optical resolution of details the used optical aid provides.

Because of the relatively small size of the projection unit, portable systems are another target application. In systems where no optical aid is necessary [Feiner et al. 1997], a Head Mounted Display suffices as output for an AR application. However, for mobile applications where a user is operating an optical aid such as a small telescope or spotting scope, a custom projection unit is desired as output.

## 8.10 Conclusion and Future Work

We have presented a system which is capable of augmenting the image visible through the eyepiece of an astronomical telescope. The user can compare the visually observed object directly with images of the same object photographed using a larger aperture telescope and long exposure time. The identification of small astronomical objects such as the major natural satellites of planets or dim stars is also assisted. Animations of the observed objects can also be blended directly into the eyepiece view, showing their 3D distribution or their projected evolution in time. Additional information regarding the observed object is also blended into the user's field of view.

In a possible future extension, the complete mapping of the lunar surface can be added to the planetarium application, making it possible to integrate a lunar atlas such as the *Virtual Moon Atlas* [Legrand and Chevalley 2004] or NASA's *World*

*Wind Moon* [[NASA 2005](#)]. This would make lunar observing much easier and features on the Moon could be identified with ease. The number of deep sky objects available in the planetarium software can also be extended as well as the amount of available textures, animations and additional information.



Figure 8.14: Our telescope mounted in the 2.6 dome situated on the roof of the institute

As a further improvement on accuracy there is the possibility of attaching a highly sensitive CCD camera to the telescope for guiding (as shown in Figure 8.1). The guiding principle consists of detecting a relatively bright star situated near the observed object using the camera, and track its position in all the following frames. If the star's absolute position changes in one of the frames, a command for a corresponding correction movement in the opposite direction is sent to the telescope mounting.

Our telescope is permanently mounted in a dome on the roof of our institute [[Lințu 2005](#)] (Figure 8.14). Possible future work would include scheduling observing sessions with the setup described in this paper to be able to gather hints about possible improvements on ease of use and understandability for the developed system.



---

---

## Chapter 9

# Discussion and Conclusion

In this dissertation we presented several novel methods to realistic and physically correct rendering of selected astronomical objects. An important contribution are also the reconstruction algorithms proposed in this thesis which enable recovering the 3D structure of planetary and reflection nebulae. We also proposed an augmented reality system for use in educational astronomy.

### 9.1 Summary

We first described an algorithm to render correct colors and shapes of the *solar disc*, given several different distributions of aerosols in the atmosphere and height to temperature profiles. We demonstrate that climate type can strongly influence the hue of the solar disc. The presence of temperature inversion layers in the atmosphere can cause several mirages observable on the solar disc, as the green flash, the red flash or the omega sun. The proposed algorithm can be used to create highly accurate rendering of the solar disc, for realistic rendering purposes such as in games or as a tool to recover atmospheric conditions based on real photographs as proposed also in [\[Bruton 1996\]](#).

For physically correct rendering of reflection nebulae we proposed a framework consisting of a rendering engine which takes into account single scattering and absorption, and approximates well multiple scattering events. This rendering framework was later used in a reconstruction step, where the 3D distribution of dust in *reflection nebulae* was recovered using an analysis-by-synthesis step. The proposed rendering framework can be used for digital media production in plane-

tarium shows to render synthetic or reconstructed nebula datasets, as well as by astrophysics researchers who can visualize in real-time the effects of changing different physical parameters as well as orientation in the appearance of a reflection nebula.

We also proposed a system to reconstruct the ionized gas and dust densities in *planetary nebulae* using similar methodology as for the reflection nebula reconstruction. In this case, we used the fact that many planetary nebulae highlight an intrinsic axially symmetric structure, thus reducing the complexity of the reconstruction process. By using images at two wavelengths at which light emitted by the nebula is affected in a different way by the inherent dust, we can recover jointly both the dust density which mainly absorbs light and the ionized gas density which emits most of the light coming from the nebula.

Further, we proposed a novel augmented reality system designed specifically for astronomical observations. The system, we call *the augmented astronomical telescope* projects with the aid of a custom developed projection unit, high resolution images, additional information and video material directly into the eyepiece view, during observation. Amongst its main applications are helping beginner amateur astronomers to distinguish very faint objects on the sky or it can be used as an observing aid for correctly identifying satellites of gas giant planets.

## 9.2 Future Work

Producing 3D animations for use in planetarium shows is currently a very tedious work. Space artist create 3D models of astronomical objects just by carefully analyzing and interpreting photographs of the objects and use a high degree of artistic skill to produce the final renderings or animations. It would be desirable in the future for space artist to be able to use tools as proposed in Chapters 5, 6 and 7 to simplify their work as well as to be able to generate models close to the real, physical models these astronomical objects show.

Renderings of the solar disc were done independently of the scene it is lighting, so no effects as for example the bright stripes visible on the ocean or the halo surrounding the disc were simulated. For a more convincing rendering in computer games or virtual reality applications, the before mentioned effects should be used in the future. Also, if we consider the whole scene while rendering, an extension to a high dynamic range rendering and tone mapping pipeline should be considered.

A possible application of the algorithm proposed to reconstruct both ionized gas

and dust densities in planetary nebulae would be in dedicated medical imaging applications where the standard tomography approach cannot be applied, i.e., there are just a very small number of input images of the object to reconstruct available. Another extension to the proposed reconstruction method would be the usage of datasets at other wavelengths which show different but known absorption or emission properties as the datasets we already used. The reconstruction algorithm for planetary nebulae using the axis symmetry constraint can also be easily adapted to the reconstruction of proto-planetary nebulae, which highlight the basic physics behind reflection nebulae [Kwok 2000].

Regarding the augmented astronomical telescope, one of the main tasks to be done in the future is to conduct user studies concerning the whole augmented reality system. Questions like the usability, the ease of use and the importance of the additional information to the observer should be investigated. An important step for the community would be to reduce the size and also the cost of the projection unit used and to make the whole system commercially available. A commercial version of our system could use the projection module proposed by Martin Neumann, in order to reduce the manufacturing prices to a minimum.





---

---

# Appendix A

## Monte-Carlo Simulation of Anisotropic Photon Scattering

This appendix describes the model used to simulate anisotropic scattering by monte-carlo simulation and it is an extract from the paper by Magnor et al. [Magnor et al. 2005].

Let the simulation consider  $N$  photons. Each photon is initialized with a weight  $w_0 = 1/N$ . Instead of a cube of edge length  $l$ , a voxel  $v$  is modeled as a sphere of the same volume. The scattering coefficient is  $\sigma_{\text{sct}} = \tau(v)/l$ . The photon is placed on the sphere at  $\mathbf{x}_0$  with its travel direction  $\mathbf{d}_0$  pointing towards the sphere's center. In the following, the photon is traced through the volume until it either emerges from the sphere, in which case its remaining weight  $w_i$  is added to the appropriate direction bin  $B[\cos \theta]$  of its emergence angle  $\cos \theta = \mathbf{d}_i \cdot \mathbf{d}_0$ , or its weight  $w_i$  falls below a minimum threshold and the photon is discarded. Given a uniformly distributed (pseudo-) random variable  $u = [0, 1]$ , the next scattering event of the photon takes place after it has travelled a length

$$r = -\ln(1 - u)/\sigma_{\text{sct}} ,$$

where  $\sigma_{\text{sct}} = 1/\bar{r}$  is the scattering coefficient. From the previous position  $\mathbf{x}_i$  and direction  $\mathbf{d}_i$ , the new scattering site's 3D coordinates are

$$\mathbf{x}_{i+1} = \mathbf{x}_i + r \cdot \mathbf{d}_i .$$

To determine the new scattering direction  $\mathbf{d}_{i+1}$ , scattering anisotropy must be taken into account. We are free to use any analytic or measured single-particle

phase function. Here, we rely on the Henyey-Greenstein phase function, (2.2), adopted from astrophysics research. For (2.2), the cumulative distribution function can be inverted analytically to yield

$$\cos \theta = \frac{1}{2g} \cdot \left( 1 + g^2 - \left( \frac{1 - g^2}{1 - g + 2gv} \right)^2 \right)$$

if  $g \neq 0$ , i.e., for non-isotropic scattering. In azimuthal angle  $\phi$ , scattering probability is constant,

$$\phi = 2\pi \cdot w .$$

Both random variables  $v, w = [0, 1]$  are uniformly distributed.

To compute the new scattering direction  $\mathbf{d}_{i+1} = (d'_x, d'_y, d'_z)$  in Cartesian coordinates, two cases must be distinguished. If the previous photon direction  $\mathbf{d}_i = (d_x, d_y, d_z)$  was almost parallel to the z-axis, e.g.,  $\|d_z\| > 0.9999$ , then

$$\begin{aligned} d'_x &= \sin \theta \cos \phi \\ d'_y &= \sin \theta \sin \phi \\ d'_z &= \frac{d_z}{\|d_z\|} \cdot \cos \theta , \end{aligned}$$

otherwise

$$\begin{aligned} d'_x &= \frac{\sin \theta}{\zeta} \cdot (d_x d_z \cos \phi - d_y \sin \phi) + d_x \cos \theta \\ d'_y &= \frac{\sin \theta}{\zeta} \cdot (d_y d_z \cos \phi + d_x \sin \phi) + d_y \cos \theta \\ d'_z &= -\zeta \sin \theta \cos \phi + d_z \cos \theta \end{aligned}$$

with  $\zeta = \sqrt{1 - d_z^2}$ . The photon weight is multiplied by the albedo,  $w_{i+1} = w_i \cdot a$ . The photon is traced until it either leaves the sphere, or until its weight  $w_i$  falls below a preset threshold. The simulation ends after simulating all  $N$  photons. The accumulated values in the bins,  $B[\cos \theta]$ , represent the row of entries for  $\tau(v)$  in the scattering probability table  $P(\tau(v), \theta)$ .

---

---

## Appendix B

# Celestial Coordinate Systems

To uniquely determine the position of an astronomical object in the sky we need to know its coordinates in a celestial coordinate system. The most widely used coordinate system in astronomy is the equatorial one. In this coordinate system, the projection of the Earth's equator on the celestial sphere is the *celestial equator* and the intersection points of the Earth's rotation axis with the celestial sphere are called the *celestial poles*. The intersection of the Earth's rotational plane with the celestial sphere is called the *ecliptic*. The celestial sphere is divided into 24 *hour circles*, each spanning  $15^\circ$ . The origin of the equatorial coordinate system is the *vernal equinox*, one of the intersection points between the celestial equator and the ecliptic (See Figure B.1). An exact position in the sky can be described by its Right Ascension  $\alpha$  and Declination  $\delta$ . Right Ascension is defined as the angle between the vernal equinox and the hour circle intersecting that point, and is measured in hours, minutes and seconds, from 0 to 24 hours. The Declination is defined as the angular distance to the celestial equator, measured in degrees, arc minutes and arc seconds, from -90 to +90 with 0 for the celestial equator [[ThinkQuest Library](#)]. The equatorial coordinate system is very similar to the geographic coordinate system used to define positions on Earth.

For an observer situated at a latitude  $\phi$  on Earth, the elevation  $E$  - azimuth  $A$  coordinate system is more straightforward. In this coordinate system the elevation is given by the altitude in degrees of an object above the horizon, and the azimuth is the angle of the object around the sky from north. The transformations from the equatorial coordinate system to the altitude (elevation) - azimuth coordinate

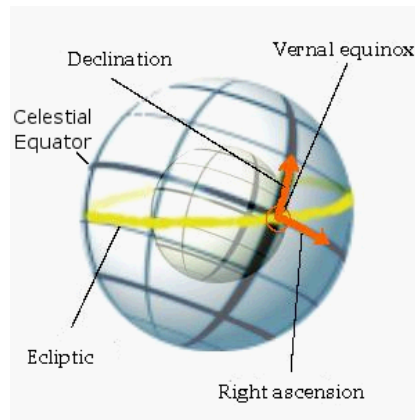


Figure B.1: The Celestial Sphere

system are the following [[Weisstein](#) ]:

$$\begin{aligned}\sin E &= \sin \phi \sin \delta + \cos \phi \cos \delta \cos \alpha \\ \cos E \cos A &= \cos \phi \sin \delta - \sin \phi \cos \delta \cos \alpha \\ \cos E \sin A &= -\cos \delta \sin \alpha.\end{aligned}$$

# Bibliography

[Aaquist and Kwok 1996]

AAQUIST, O. B., AND KWOK, S. 1996. Radio Morphologies of Planetary Nebulae. *The Astrophysical Journal* 462 (May), 813–+.

[Arridge 1999]

ARRIDGE, S. 1999. Optical tomography in medical imaging. *Inverse Problems* 15, R41–R93.

[ArtCom 2005]

ARTCOM, 2005. Timescope. available from [www.artcom.de/index.php?option=com\\_acprojects&page=6&id=38&Itemid=115&details=0&lang=en](http://www.artcom.de/index.php?option=com_acprojects&page=6&id=38&Itemid=115&details=0&lang=en).

[Azuma 1997]

AZUMA, R. T. 1997. A Survey of Augmented Reality. In *Presence: Teleoperators and Virtual Environments*, vol. 6, 355–385.

[Balick and Frank 2002]

BALICK, B., AND FRANK, A. 2002. Shapes and Shaping of Planetary Nebulae. *Annual Review of Astronomy and Astrophysics* 40, 439–486.

[Beamon 1990]

BEAMON, W. S., 1990. Helmet display, Jan.

[Bimber and Raskar 2005]

BIMBER, O., AND RASKAR, R. 2005. *Spatial augmented reality*:

- merging real and virtual worlds*. Wellesley, Mass.: AK Peters.
- [Binney and Merrifield 1998] BINNEY, J., AND MERRIFIELD, M. 1998. *Galactic astronomy*. Galactic astronomy / James Binney and Michael Merrifield. Princeton, NJ : Princeton University Press, 1998. (Princeton series in astrophysics).
- [Binzoni et al. 2006] BINZONI, T., LEUNG, T., GANDBAKHCHE, A., RÜFENACHT, D., AND DELPY, D. 2006. The use of the Henyey–Greenstein phase function in Monte Carlo simulations in biomedical optics. *Physics in Medicine and Biology* 51, 17, N313–N322.
- [Birkfellner et al. 2000] BIRKFELLNER, W., HUBER, K., WATZINGER, F., FIGL, M., WANSCHITZ, F. AND HANEL, R., RAFOLT, D., EWERS, R., AND BERGMANN, H. 2000. Development of the Varioscope AR - A See-through HMD for Computer-Aided Surgery. In *Proceedings of the IEEE and ACM International Symposium on Augmented Reality*, 54 – 59.
- [Bremer 1995] BREMER, M. 1995. A 3D iterative deprojection technique. I. Development of the algorithm and tests. *Astronomy and Astrophysics* 112 (Sept.), 551–566.
- [Bronnikov 1999] BRONNIKOV, A. V. 1999. Numerical solution of the identification problem for the attenuated Radon transform. *Institute of Physics, Electronical Journals*.

- [Bruton 1996] BRUTON, D. 1996. *Optical Determination of Atmospheric Temperature Profiles*. PhD thesis, Texas A&M University.
- [Carl Zeiss Jena GmbH 2007] CARL ZEISS JENA GMBH, 2007. Digistar 3. available from [www.zeiss.de/planetariums](http://www.zeiss.de/planetariums).
- [Celestron, LLC. 2006] CELESTRON, LLC., 2006. Celestron sky scout. available from [www.celestron.com/skyscout](http://www.celestron.com/skyscout).
- [Cellarius 1661] CELLARIUS, A. 1661. *Harmonia macrocosmica, seu Atlas universalis et novus, totius universi creati cosmographiam generalem, et novam exhibens*. Amstelodami, apud Joannem Janssonium, anno 1661.
- [Chéreau 2005] CHÉREAU, F., 2005. Stellarium. available from [stellarium.sourceforge.net](http://stellarium.sourceforge.net).
- [Ciddor 1996] CIDDOR, P. E. 1996. Refractive index of air: new equations for the visible and near infrared. *Applied Optics* 35, 9 (Mar.), 1566–1573.
- [Clark 1990] CLARK, R. N. 1990. *Visual Astronomy of the Deep Sky*. Cambridge University Press.
- [Clark 2002] CLARK, R. N., 2002. Visual Astronomy of the Deep Sky - Appendix E. available from [clarkvision.com/visastro/appendix-e.html](http://clarkvision.com/visastro/appendix-e.html).
- [Cogo 1996 - 2004] COGO, M., 1996 - 2004. Astrophotography. available from [www.intersoft.it/galaxlux](http://www.intersoft.it/galaxlux).

- [Corwin Jr. 2005] CORWIN JR., H. G., 2005. The NGC / IC Project. available from [www.ngcic.org](http://www.ngcic.org).
- [Crinklaw 2005] CRINKLAW, G., 2005. Cocoon nebula (IC 5146, OCL 213). available from [www.skyhound.com/sh/archive/sep/Cocoon.html](http://www.skyhound.com/sh/archive/sep/Cocoon.html).
- [Croman 2005] CROMAN, R., 2005. Russel Croman Astrophotography. available from [www.rc-astro.com](http://www.rc-astro.com).
- [Cybermind Interactive Nederland ] CYBERMIND INTERACTIVE NEDERLAND. Visette45 sxga. available from [www.cybermindnl.com](http://www.cybermindnl.com).
- [Daly 2005] DALY, K., 2005. M31. available from [members.aol.com/KDaly10475/m31.html](http://members.aol.com/KDaly10475/m31.html).
- [Elias 2007] ELIAS, H., 2007. Perlin noise webpage. available from [freespace.virgin.net/hugo.elias/models/m\\_perlin.htm](http://freespace.virgin.net/hugo.elias/models/m_perlin.htm).
- [Ellenby et al. 1997] ELLENBY, J., ELLENBY, T., AND ELLENBY, P., 1997. Vision imaging devices and methods exploiting position and attitude, Oct.
- [Ercolano et al. 2003] ERCOLANO, B., BARLOW, M. J., STOREY, P. J., AND LIU, X.-W. 2003. MOCASSIN: a fully three-dimensional Monte Carlo photoionization code. *Monthly Notices of the Royal Astronomical Society* 340 (Apr.), 1136–1152.
- [Ercolano et al. 2005] ERCOLANO, B., BARLOW, M. J., AND STOREY, P. J. 2005. The dusty MOCASSIN: fully self-consistent 3D photoionization and dust radiative transfer models. *Monthly Notices of the Royal*



- Astronomical Society* 362 (Sept.), 1038–1046.
- [Evans & Sutherland 2007] EVANS & SUTHERLAND, 2007. Digistar 3. available from [www.es.com/products/digital\\_theater/](http://www.es.com/products/digital_theater/).
- [Evans and Sutherland 2000] EVANS, AND SUTHERLAND, 2000. Wonders of the universe – planetarium show. available from [www.es.com/products/digital\\_theater/wonders\\_2.jpg](http://www.es.com/products/digital_theater/wonders_2.jpg).
- [Feiner et al. 1997] FEINER, S., MACINTYRE, B., HOLLERER, T., AND WEBSTER, A. 1997. A touring machine: Prototyping 3D mobile augmented reality systems for exploring the urban environment. In *In Proc. ISWC '97 (Int. Symp. on Wearable Computers)*, 74–81.
- [Ferwerda et al. 1996] FERWERDA, J. A., PATTANAIK, S. N., SHIRLEY, P., AND GREENBERG, D. P. 1996. A Model of Visual Adaptation for Realistic Image Synthesis. In *SIGGRAPH '96: Proceedings of the 23rd annual conference on Computer graphics and interactive techniques*, ACM Press, New York, NY, USA, 249–258.
- [Fu and Hanson 2007] FU, C., AND HANSON, A. 2007. A Transparently Scalable Visualization Architecture for Exploring the Universe. *IEEE Transactions on Visualization and Computer Graphics* 13, 1, 108–121.
- [Gendler 2007] GENDLER, R., 2007. The universe in colors. available from [www.robgendlerastropics.com](http://www.robgendlerastropics.com).

- [Google Inc. 2005] GOOGLE INC., 2005. Google Earth. available from [earth.google.com](http://earth.google.com).
- [Gordon et al. 1970] GORDON, R., BENDER, R., AND HERMAN, G. 1970. Algebraic Reconstruction Techniques (ART) for Three-dimensional Electron Microscopy and X-ray Photography. *Journal of Theoretical Biology* 29, 471–481.
- [Gordon et al. 2001] GORDON, K. D., MISSELT, K. A., WITT, A. N., AND CLAYTON, G. C. 2001. The DIRTY Model. I. Monte Carlo Radiative Transfer through Dust. *The Astrophysical Journal* 551 (Apr.), 269–276.
- [Gordon 2004a] GORDON, K. 2004. Interstellar dust scattering properties. In *Astrophysics of dust*, ASP conference series, A. Witt, G. Clayton, and B. Draine, Eds.
- [Gordon 2004b] GORDON, K. D. 2004. Interstellar Dust Scattering Properties. In *Astrophysics of Dust*, A. N. Witt, G. C. Clayton, and B. T. Draine, Eds., vol. 309 of *Astronomical Society of the Pacific Conference Series*, 77–+.
- [Greiner 1998] GREINER, R. A., 1998. Data on Precision Error Correction for LX200 Telescopes. available from [www.mailbag.com/users/ragreiner/PEC-WORM.html](http://www.mailbag.com/users/ragreiner/PEC-WORM.html).
- [Gröller 1995] GRÖLLER, E. 1995. Nonlinear ray tracing: Visualizing strange worlds. *The Visual Computer* 11, 5, 263–274.

- [Groshong 2006] GROSHONG, K., 2006. New scientist space: Augmented reality telescope brings universe closer. available from [space.newscientist.com/article.ns?id=dn8653](http://space.newscientist.com/article.ns?id=dn8653).
- [Gutierrez et al. 2005] GUTIERREZ, D., MUNOZ, A., ANSON, O., AND SERON, F. J. 2005. Non-linear volume photon mapping. In *Proceedings of Eurographics Symposium on Rendering 2005*, Eurographics.
- [Gutierrez et al. 2004] GUTIERREZ, D., SERON, F., ANSON, O., AND MUNOZ, A. 2004. Chasing the Green Flash: a Global Illumination Solution for Inhomogeneous Media. In *Spring Conference On Computer Graphics 2004*, 95–103.
- [Haber et al. 2005] HABER, J., MAGNOR, M., AND SEIDEL, H.-P. 2005. Physically-based simulation of twilight phenomena. *ACM Transactions on Graphics* 24, 4, 1353–1373.
- [Hadamard 1902] HADAMARD, J. 1902. Sur les problèmes aux drives partielles et leur signification physique. *Bull. Univ. Princeton* 13, 49–52.
- [Hall 1989] HALL, R. 1989. *Illumination and Color in Computer Generated Imagery*. Springer, New York.
- [Hanson et al. 2000] HANSON, A., FU, C., AND WERNERT, E. 2000. Very large scale visualization methods for astrophysical data. *Proceedings of the Joint Eurographics and IEEE TVCG Symposium on Visualization*, 115–124.

- [Henyey and Greenstein 1941] HENYEY, L. G., AND GREENSTEIN, J. L. 1941. Diffuse Radiation in the Galaxy. *Astrophysical Journal* 93, 70–83.
- [Hess et al. 1998] HESS, M., KOEPKE, P., AND SCHULT, I. 1998. Optical Properties of Aerosols and Clouds: The Software Package OPAC. *Bulletin of the American Meteorological Society* 79, 5 (May), 831–844.
- [Hess 1998] HESS, M., 1998. OPAC (Optical Properties of Aerosols and Clouds). available from <ftp://ftp.lrz-muenchen.de/pub/science/meteorology/aerosol/opac/>.
- [Hildebrand et al. 2006] HILDEBRAND, K., MAGNOR, M., AND FROELICH, B. 2006. 3d reconstruction and visualization of spiral galaxies. In *WSCG'2006 Full Papers Conference Proceedings*, 113–120.
- [Hügler 2006] HÜGLER, S. 2006. Dem wetter trotzen. *Astronomie Heute* (July), 52–54.
- [HyperPhysics 2007] HYPERPHYSICS, 2007. Blue sky and rayleigh scattering. available from [hyperphysics.phy-astr.gsu.edu/hbase/atmos/blusky.html](http://hyperphysics.phy-astr.gsu.edu/hbase/atmos/blusky.html).
- [Jacobsen 2005] JACOBSEN, A., 2005. Opsys project consulting. available from [opsysconsult.com](http://opsysconsult.com).
- [Kähler et al. 2002] KÄHLER, R., COX, D., PATTERSON, R., LEVY, S., HEGE, H., AND ABEL, T. 2002. Rendering the first star in the Universe-A

- case study. *Visualization, 2002. VIS 2002. IEEE*, 537–540.
- [Kähler et al. 2006] KÄHLER, R., WISE, J., ABEL, T., AND HEGE, H.-C. 2006. GPU-assisted raycasting for cosmological adaptive mesh refinement simulations. In *Eurographics/IEEE VGTC Workshop on Volume Graphics*, Eurographics Association, Boston, Massachusetts, USA, R. Machiraju and T. Möller, Eds., 103–110.
- [Kähler et al. 2007] KÄHLER, R., WISE, J., ABEL, T., AND HEGE, H.-C. 2007. Simultaneous GPU-Assisted Raycasting of Unstructured Point Sets and Volumetric Grid Data. In *IEEE/EG International Symposium on Volume Graphics*, H.-C. Hege and R. Machiraju, Eds., 49–56.
- [Kak and Slaney 1988] KAK, A., AND SLANEY, M. 1988. *Principles of Computerized Tomographic Imaging*. IEEE Press New York.
- [Knuth and Hajian 2002] KNUTH, K., AND HAJIAN, A. 2002. Hierarchies of Models: Toward Understanding Planetary Nebulae. *Bayesian Inference and Maximum Entropy Methods in Science and Engineering* 22, 92–103.
- [Kopf et al. 2007] KOPF, J., FU, C.-W., COHEN-OR, D., DEUSSEN, O., LISCHINSKI, D., AND WONG, T.-T. 2007. Solid texture synthesis from 2d exemplars. *ACM Transactions on Graphics (Proceedings of SIGGRAPH 2007)* 26, 3, to appear.

- [Krueger and Westermann 2003] KRUEGER, J., AND WESTERMANN, R. 2003. Acceleration techniques for gpu-based volume rendering. In *Proc. IEEE Visualization*, 287–292.
- [Krüger and Westermann 2003] KRÜGER, J., AND WESTERMANN, R. 2003. Acceleration techniques for GPU-based volume rendering. In *14th IEEE Visualization 2003 Conference (VIS 2003), 19-24 October 2003, Seattle, WA, USA*, IEEE Computer Society, G. Turk, J. J. van Wijk, and R. M. II, Eds., 287–292.
- [Kurucz et al. 1984] KURUCZ, R. L., FURENLID, I., BRAULT, J., AND TESTERMAN, L. 1984. Solar Flux Atlas from 296 to 1300 nm. Tech. rep., NOAO, Sunspot, NM. available from [kurucz.harvard.edu/sun/fluxatlas/](http://kurucz.harvard.edu/sun/fluxatlas/).
- [Kwok 2000] KWOK, S. 2000. *The Origin and Evolution of Planetary Nebulae*. Cambridge ; New York : Cambridge University Press, 2000. (Cambridge astrophysics series ; 33), June.
- [Lee and Kwok 2005] LEE, T.-H., AND KWOK, S. 2005. Dust Extinction in Compact Planetary Nebulae. *The Astrophysical Journal* 632 (Oct.), 340–354.
- [Legrand and Chevalley 2004] LEGRAND, C., AND CHEVALLEY, P., 2004. Virtual Moon Atlas. available from [www.astrosurf.com/avl](http://www.astrosurf.com/avl).
- [Lehn 1985] LEHN, W. H. 1985. A simple parabolic model for optics of the atmospheric surface layer. *Ap-*

- plied Mathematical Modelling* 9 (December), 447–453.
- [Lensch 2003] LENSCH, H. P. A. 2003. *Efficient, Image-Based Appearance Acquisition of Real-World Objects*. PhD thesis, Saarland University.
- [Lințu and Magnor 2005] LINȚU, A., AND MAGNOR, M. 2005. Augmented Astronomical Telescope. In *Second GI-Workshop VR/AR Proceedings*, Shaker Verlag, T. Kuhlen, L. Kobbelt, and S. Müller, Eds., 203–213.
- [Lințu and Magnor 2006] LINȚU, A., AND MAGNOR, M. 2006. An Augmented Reality System for Astronomical Observations. In *IEEE Virtual Reality 2006*, IEEE, Alexandria, Virginia, USA, IEEE Computer Society, 119–126.
- [Lințu et al. 2005] LINȚU, A., HABER, J., AND MAGNOR, M. 2005. Realistic Solar Disc Rendering. In *WSCG'2005 Full Papers Conference Proceedings*, 79–86.
- [Lințu et al. 2007a] LINȚU, A., HOFFMAN, L., MAGNOR, M., LENSCH, H. P. A., AND SEIDEL, H.-P. 2007. 3D Reconstruction of Reflection Nebulae from a Single Image. In *Vision, Modelling and Visualization*. to appear.
- [Lințu et al. 2007b] LINȚU, A., LENSCH, H. P. A., MAGNOR, M., EL-ABED, S., AND SEIDEL, H.-P. 2007. 3D Reconstruction of Emission and Absorption in Planetary Nebulae. In *IEEE/EG International Symposium on Volume Graphics*, H.-C. Hege and R. Machiraju, Eds., 9–16.

- [Lințu et al. 2007c] LINȚU, A., LENSCH, H. P. A., MAGNOR, M., LEE, T.-H., EL-ABED, S., AND SEIDEL, H.-P. 2007. A Multi-wavelength-based Method to de-project Gas and Dust Distributions of several Planetary Nebulae. In *Asymmetrical Planetary Nebulae IV*. to appear.
- [Lințu 2005] LINȚU, A., 2005. Astronomy at the MPI Informatics. available from [www.mpi-inf.mpg.de/~lintu/astronomy.html](http://www.mpi-inf.mpg.de/~lintu/astronomy.html).
- [Lucy 1974] LUCY, L. 1974. An iterative technique for the rectification of observed distributions. *The Astronomical Journal* 79, 6, 745–754.
- [Magnor et al. 2004] MAGNOR, M., KINDLMANN, G., HANSEN, C., AND DURIC, N. 2004. Constrained inverse volume rendering for planetary nebulae. In *Proc. IEEE Visualization 2004, Austin, USA*, 83–90.
- [Magnor et al. 2005] MAGNOR, M., HILDEBRAND, K., LINȚU, A., AND HANSON, A. J. 2005. Reflection Nebula Visualization. In *Proceedings of the IEEE Conference on Visualization (VIS'05)*, IEEE, Minneapolis, USA, C. Silva, E. Gröller, and H. Rushmeier, Eds., 255–262.
- [Marschner 1998] MARSCHNER, S. R. 1998. *Inverse Rendering in Computer Graphics*. PhD thesis, Program of Computer Graphics, Cornell University, Ithaca, NY.
- [Meade Instruments Corp. 2002] MEADE INSTRUMENTS CORP., 2002. Meade Telescope Serial Command Protocol. available



- from [www.meade.com/support/CommandSet.html](http://www.meade.com/support/CommandSet.html).
- [Meade Instruments Corp. 2003] MEADE INSTRUMENTS CORP., 2003. Instruction Manual – 10” LX200GPS Schmidt-Cassegrain Telescopes. available from [www.meade.com/manuals/TelescopeManuals/LXseries/LX200GPS\\_manual.pdf](http://www.meade.com/manuals/TelescopeManuals/LXseries/LX200GPS_manual.pdf).
- [Meade Instruments Corp. 2007] MEADE INSTRUMENTS CORP., 2007. Meade mySKY. available from [meade.com/mysky](http://meade.com/mysky).
- [Melville 1999] MELVILLE, C. D., 1999. Augmented imaging using a silhouette to improve contrast, June.
- [Minnaert 1954] MINNAERT, M. 1954. *The nature of light and colour in the open air*. Dover Books on Earth Sciences, New York: Dover, 1954, edited by Jay, K.E. Brian (rev.).
- [Monteiro et al. 2005] MONTEIRO, H., SCHWARZ, H. E., GRUENWALD, R., GUENTHNER, K., AND HEATHCOTE, S. R. 2005. Three-Dimensional Photoionization Structure and Distances of Planetary Nebulae. II. Menzel 1. *The Astrophysical Journal* 620 (Feb.), 321–329.
- [Morisset 2006] MORISSET, C. 2006. Cloudy\_3D, a new pseudo-3D photoionization code. In *Planetary Nebulae in our Galaxy and Beyond*, M. J. Barlow and R. H. Méndez, Eds., vol. 234 of *IAU Symposium*, 467–468.
- [Nadeau et al. 2001] NADEAU, D. R., GENETTI, J. D., NAPEAR, S., PAILTHORPE, B., EMMART, C., WESSELAK, E.,

- AND DAVIDSON, D. 2001. Visualizing stars and emission nebulas. *Comput. Graph. Forum* 20, 1, 27–33.
- [Nagel et al. 1978] NAGEL, M. R., QUENZEL, H., KWET, W., AND WENDLING, R. 1978. *Daylight Illumination — Color-Contrast Tables for Full-Form Objects*. Academic Press, New York.
- [NASA a] NASA. Hubble Space Telescope Gallery. available from [hubblesite.org/gallery](http://hubblesite.org/gallery).
- [NASA b] NASA. NASA/Marschal Solar Physics. available from [solarscience.msfc.nasa.gov/surface.shtml](http://solarscience.msfc.nasa.gov/surface.shtml).
- [NASA c] NASA. The Electromagnetic Spectrum. available from [mynasadata.larc.nasa.gov/ElectroMag.html](http://mynasadata.larc.nasa.gov/ElectroMag.html).
- [NASA 2005] NASA, 2005. World Wind Moon. available from [worldwind.arc.nasa.gov/moon.html](http://worldwind.arc.nasa.gov/moon.html).
- [NASA 2007] NASA, 2007. Hubble Space Telescope Online Archive. available from [archive.stsci.edu/hst/search.php](http://archive.stsci.edu/hst/search.php).
- [Nishita et al. 1993] NISHITA, T., SIRAI, T., TADAMURA, K., AND NAKAMAE, E. 1993. Display of The Earth Taking into account Atmospheric Scattering. In *Computer Graphics (SIGGRAPH '93 Conf. Proc.)*, ACM SIGGRAPH, J. T. Kajiya, Ed., 175–182.

- [Nishita et al. 1996] NISHITA, T., DOBASHI, Y., KANEDA, K., AND YAMASHITA, H. 1996. Display Method of the Sky Color Taking into Account Multiple Scattering. In *Proc. Pacific Graphics '96*, IEEE, 117–132.
- [Nvis Inc. 2005] NVIS INC., 2005. Nvisor SX. available from [www.nvisinc.com/nvisor\\_sx.php](http://www.nvisinc.com/nvisor_sx.php).
- [Osterbrock 1974] OSTERBROCK, D. E. 1974. *Astrophysics of gaseous nebulae*. San Francisco, W. H. Freeman and Co., 1974. 263 p.
- [Perlin 1985] PERLIN, K. 1985. An image synthesizer. In *SIGGRAPH '85: Proceedings of the 12th annual conference on Computer graphics and interactive techniques*, ACM Press, New York, NY, USA, 287–296.
- [Petty 2004] PETTY, G. 2004. *A First Course in Atmospheric Radiation*. Sundog.
- [Planck 1901] PLANCK, M. 1901. Ueber das Gesetz der Energieverteilung im Normalspectrum. *Annalen der Physik* 309, 3, 553–563.
- [Powell 1964] POWELL, M. 1964. An efficient method for finding the minimum of a function of several variables without calculating derivatives. *The Computer Journal* 7, 2, 155.
- [Preetham et al. 1999] PREETHAM, A. J., SHIRLEY, P., AND SMITS, B. 1999. A Practical Analytic Model for Daylight. In *Computer Graphics (SIGGRAPH '99 Conf. Proc.)*, ACM SIGGRAPH, 91–100.

- [Press et al. 1992] PRESS, W. H., TEUKOLSKY, S. A., VETTERLING, W. T., AND FLANNERY, B. P. 1992. *Numerical Recipes in C: The Art of Scientific Computing*, 2. ed. Cambridge University Press, Cambridge, MA.
- [Reeves et al. 2005] REEVES, S., FRASER, M., SCHNÄDELBACH, H., O'MALLEY, C., AND BENFORD, S. 2005. Engaging augmented reality in public places. In *Adjunct proceedings of SIGCHI Conference on Human Factors in Computing Systems (CHI)*.
- [Richardson 1972] RICHARDSON, W. 1972. Bayesian-based iterative method of image restoration. *J. Opt. Soc. Am* 62, 1, 55–59.
- [Scharsach 2005] SCHARSACH, H. 2005. Advanced GPU raycasting. In *Central European Seminar on Computer Graphics (CESG'05)*. available from [www.cg.tuwien.ac.at/studentwork/CESCG/proceedings.html](http://www.cg.tuwien.ac.at/studentwork/CESCG/proceedings.html).
- [Seron et al. 2004] SERON, F., GUTIERREZ, D., GUTIERREZ, G., AND CEREZO, E. 2004. Visualizing Sunsets through Inhomogeneous Atmospheres. In *Proceedings of Computer Graphics International 2004(CGI 2004)*, IEEE Computer Society Press, 349–356.
- [Sharpe et al. 2002] SHARPE, J., AHLGREN, U., PERRY, P., HILL, B., ROSS, A., HECKSHER-SORENSEN, J., BALDOCK, R., AND DAVIDSON, D. 2002. Optical Projection

- Tomography as a Tool for 3D Microscopy and Gene Expression Studies. *Science* 296, 19.
- [Sloup 2002] SLOUP, J. 2002. A Survey of Modelling and Rendering of the Earth's Atmosphere. In *Proc. 18th Spring Conference on Computer Graphics (SCCG 2002)*, 135–144.
- [Sloup 2003] SLOUP, J. 2003. Visual simulation of refraction phenomena in the Earth's atmosphere. *Proceedings. Seventh International Conference on Information Visualization, 2003. IV 2003.*, 452–457.
- [Sobierajski and Avila 1995] SOBIERAJSKI, L. M., AND AVILA, R. S. 1995. A Hardware Acceleration Method for Volumetric Ray Tracing. In *IEEE Visualization*, 27.
- [Steffen and López 2006] STEFFEN, W., AND LÓPEZ, J. A. 2006. Morpho-Kinematic Modeling of Gaseous Nebulae with SHAPE. *Revista Mexicana de Astronomía y Astrofísica* 42 (Apr.), 99–105.
- [Stricker 2005] STRICKER, D., 2005. Augmented reality telescope. available from [www.xc-01.de](http://www.xc-01.de).
- [Tarantola 2005] TARANTOLA, A. 2005. *Inverse Problem Theory and Methods for Model Parameter Estimation*. Society for Industrial & Applied Mathematics.
- [Texas Instruments 2004 - 2007] TEXAS INSTRUMENTS, 2004 - 2007. DLP Technology Overview. available from [www.dlp.com/tech/what](http://www.dlp.com/tech/what).

- [ThinkQuest Library ] THINKQUEST LIBRARY. Coordinate systems. available from [library.thinkquest.org/29033/begin/coordinate.htm](http://library.thinkquest.org/29033/begin/coordinate.htm).
- [Tonel 2007] TONEL, G., 2007. Unconstrained optimization using powell. available from [www.mathworks.com/matlabcentral/files/15072/powell.JPG](http://www.mathworks.com/matlabcentral/files/15072/powell.JPG).
- [Tonkin ] TONKIN, S. The Three Functions of a Telescope. available from [www.astunit.com/tutorials/telescope.htm](http://www.astunit.com/tutorials/telescope.htm).
- [Trifonov et al. 2006] TRIFONOV, B., BRADLEY, D., AND HEIDRICH, W. 2006. Tomographic reconstruction of transparent objects. In *Rendering Techniques 2006: 17th Eurographics Workshop on Rendering*, 51–60.
- [Tumblin and Rushmeier 1993] TUMBLIN, J., AND RUSHMEIER, H. E. 1993. Tone reproduction for realistic images. *IEEE Computer Graphics and Applications* 13, 6 (Nov.), 42–48.
- [van de Hulst 1982] VAN DE HULST, H. C. 1982. *Light Scattering by Small Particles*. Dover Publications, Inc., New York.
- [van Gent, Robert 2007] VAN GENT, ROBERT, 2007. Andreas cellarius - a bibliographical overview. available from [www.phys.uu.nl/~vgent/cellarius/cellarius.htm](http://www.phys.uu.nl/~vgent/cellarius/cellarius.htm).
- [Volk and Leahy 1993] VOLK, K., AND LEAHY, D. 1993. Deprojection of planetary nebula images. *The Astronomical Journal* 106, 1954.

- [VR Centre for the Built Environment 2004] VR CENTRE FOR THE BUILT ENVIRONMENT, 2004. Arthur. available from [www.vr.ucl.ac.uk/projects/arthur](http://www.vr.ucl.ac.uk/projects/arthur).
- [Wann Jensen et al. 2000] WANN JENSEN, H., PREMOZE, S., SHIRLEY, P., THOMPSON, W. B., FERWERDA, J. A., AND STARK, M. M. 2000. Night rendering. Technical Report UUCS-00-016, Computer Science Dept., University of Utah, Aug.
- [Wann Jensen et al. 2001] WANN JENSEN, H., DURAND, F., STARK, M. M., PREMOZE, S., DORSEY, J., AND SHIRLEY, P. 2001. A Physically-Based Night Sky Model. In *Computer Graphics (SIGGRAPH 2001 Conf. Proc.)*, ACM SIGGRAPH, 399–408.
- [Weisstein ] WEISSTEIN, E. W. Altitude-azimuth coordinates. available from [scienceworld.wolfram.com/astronomy/Altitude-AzimuthCoordinates.html](http://scienceworld.wolfram.com/astronomy/Altitude-AzimuthCoordinates.html).
- [Wood et al. 2004] WOOD, K., MATHIS, J. S., AND ERCOLANO, B. 2004. A three-dimensional Monte Carlo photoionization code for modelling diffuse ionized gas. *Monthly Notices of the Royal Astronomical Society* 348 (Mar.), 1337–1347.
- [Wyszecki and Stiles 1982] WYSZECKI, G., AND STILES, W. S. 1982. *Color Science: Concepts and Methods, Quantitative Data and Formulae*, 2nd ed. John Wiley & Sons, New York.
- [Young 1999 - 2004] YOUNG, A. T., 1999 - 2004. A Green Flash Page. available from

- [mintaka.sdsu.edu/GF/index.html](http://mintaka.sdsu.edu/GF/index.html).
- [Young 2000] YOUNG, A. 2000. Sunset science. III. Visual adaptation and green flashes. *Journal of the Optical Society of America A* 17, 12, 2129–2139.
- [Zinner 1957] ZINNER, E. 1957. *Astronomische Instrumente des 11. bis 18. Jahrhunderts*. C. H. Beck, München.
- [Zoellner et al. 2005] ZOELLNER, M., STRICKER, D., AND BOCKHOLT, U. 2005. AR Telescope - Taking Augmented Reality to a large Audience. *COMPUTER GRAPHIK topics* 17, 1, 19–20.
- [Zotti and Gröller 2005] ZOTTI, G., AND GRÖLLER, M. E. 2005. A sky dome visualisation for identification of astronomical orientations. In *Proceedings IEEE Symposium on Information Visualization*, IEEE, J. Stasko and M. Ward, Eds., 9–16.
- [Zotti et al. 2006] ZOTTI, G., WILKIE, A., AND PURGATHOFER, W. 2006. Using virtual reconstructions in a planetarium for demonstrations in archaeo-astronomy. In *Third Central European Multimedia and Virtual Reality Conference (Proc. CEMVRC2006)*, Pannonian University Press, C. S. Lanyi, Ed., 43–51.
- [Zotti et al. 2007] ZOTTI, G., WILKIE, A., AND PURGATHOFER, W. 2007. A Critical Review of the Preetham Sky-light Model. In *Short Communi-*



*cation Proceedings of WSCG 2007,*  
23–30.



# Curriculum Vitae – Lebenslauf

## Curriculum Vitae

January 1980		born in Oradea, Romania
September 1987	– July 1995	Primary School, Oradea, Romania
September 1995	– July 1998	High School Degree, Oradea, Romania
September 1998	– August 2003	Diploma [M.Sc.] in Computer Science Engineering, Politehnica University, Timișoara, Romania
October 2003	– December 2007	Ph.D. in Computer Graphics, Max-Planck-Institut für Informatik Saarbrücken, Germany

## Lebenslauf

Januar 1980		geboren in Oradea, Rumänien
September 1987	– Juli 1995	Grundschule, Oradea, Rumänien
September 1995	– Juli 1998	Gymnasium mit Abiturabschluss Oradea, Rumänien
September 1998	– August 2003	Diplom Ingenieur in Informatik, Politehnica Universität Timișoara, Rumänien
Oktober 2003	– December 2007	Promotion in Computergrafik, Max-Planck-Institut für Informatik Saarbrücken, Deutschland